Aalto University
School of Science
and Technology

Faculty of Chemistry and Materials Sciences
Degree Programme of Chemical Technology

Kaj Nikiforow

OPTIMIZATION OF POLYMER ELECTROLYTE MEMBRANE FUEL CELL SYSTEMS – APPLIED STUDY OF HYDROGEN RECIRCULATION

Master's thesis for the degree of Master of Science in Technology submitted for inspection, Espoo, 1 December, 2010.

Supervisor	**Prof. Ville Alopaeus**
Instructor	**Jari Ihonen, Ph.D.(Tech.)** **Tanja Kallio, Ph.D.(Tech.)**

Aalto University
School of Science
and Technology

Faculty of Chemistry and Materials Sciences **Abstract of Master's Thesis**
Degree Programme of Chemical Technology

Author

Kaj Nikiforow

Title of Thesis

Optimization of polymer electrolyte membrane fuel cell systems – Applied study of hydrogen recirculation

Abstract

The goal of this thesis was to investigate the effects of hydrogen recirculation in a polymer electrolyte membrane fuel cell (PEMFC) on hydrogen stoichiometry and on the build-up of nitrogen in the recirculated stream as well as the effects of nitrogen build-up on the fuel cell performance. Recirculation of hydrogen has a remarkable effect on the overall efficiency of a fuel cell system, as recirculation affects not only the performance of the fuel cell through hydrogen stoichiometry and water balance but also the consumption of fuel. However, recirculation of hydrogen consumes energy and causes impurities to build up in the recirculated stream.

In this work, recirculation of hydrogen was studied by simulating an ejector model as well as through experimental work conducted on an 8-kW$_e$ PEMFC system. The ejector model presented in this work was based on the assumptions of one-dimensional flow in steady state as well as constant area and constant pressure mixing. In the experimental part of this work, the build-up of nitrogen in the recirculated stream was monitored using a hydrogen sensor which measured the partial pressure of hydrogen.

Based on the simulations with the ejector model, it was found that the achievable recirculation rate strongly depends on several factors, such as the flow resistance of the stack, the dimensions of the ejector, and the hydrogen feed pressure. The results from the experimental work revealed that the build-up of nitrogen has a profound effect on cell voltages, depending strongly, however, on the conditions of the cells. Hence, the condition of the cells must be taken into account when optimizing the fuel supply in a PEMFC.

Chair **Chemical Engineering**	**Chair code** **KE-42**
Supervisor **Prof. Ville Alopaeus**	**Pages** **87**
Instructor **Jari Ihonen, Ph.D.(Tech.); Tanja Kallio, Ph.D.(Tech.)**	**Language** **English**
Keywords **PEMFC, hydrogen recirculation, ejector model, nitrogen build-up**	**Date** **1.12.2010**

Aalto University
School of Science
and Technology

Kemian ja materiaalitieteiden tiedekunta **Diplomityön tiivistelmä**

Kemian tekniikan koulutus- / tutkinto-ohjelma

Tekijä

Kaj Nikiforow

Diplomityön nimi

Polymeeripolttokennojärjestelmän optimointi – Vedyn kierrätyksen soveltava tarkastelu

Tiivistelmä

Tämän diplomityön tavoitteena oli tutkia vedyn kierrättämisen vaikutusta polymeeripolttokennossa vedyn stoikiometriseen kertoimeen ja typen rikastumiseen vetykierrossa sekä typen rikastumisen vaikutusta polttokennon suorituskykyyn.

Vedyn kierrättämisellä on merkittävä vaikutus polttokennojärjestelmän kokonaishyötysuhteeseen. Kierrätyksellä voidaan parantaa polttokennon suorituskykyä vaikuttamalla vedyn stoikiometriseen kertoimeen ja veden hallintaan, joilla on edelleen vaikutusta polttoaineen käyttöasteeseen. Vedyn kierrättäminen kuitenkin kuluttaa energiaa ja johtaa epäpuhtauksien rikastumiseen vetykierrossa.

Tässä työssä vedyn kierrätystä tutkittiin sekä mallintamalla vety-ejektoria että suorittamalla kokeita 8 kW_e polymeeripolttokenno-järjestelmällä. Työssä esitetyssä ejektorimallissa oletettiin 1-uloittteinen stationaarinen virtaus sekä vakio pinta-ala- ja vakio paine-sekoittuminen. Työn kokeellisessa osassa typen rikastumista kierrätetyssä kaasussa tutkittiin vetyanturin avulla, joka mittasi vedyn osapainetta.

Ejektori-mallin simulointitulosten perusteella voitiin todeta, että saavutettavaan kierrätysnopeuteen vaikuttaa merkittävästi polttokennoston virtausvastus, ejektorin mitat sekä vedyn syöttöpaine. Kokeelliset tulokset osoittivat että typen rikastuminen vetykiertoon vaikuttaa merkittävästi kennojännitteisiin, kuitenkin voimakkaasti riippuen siitä miten kennot ovat vanhentuneet. Näin ollen kennojen kunto on otettava huomioon optimoitaessa polttoaineen syöttöä polymeeripolttokennossa.

Professuurin nimi **Kemian laitetekniikka**	**Professuurin koodi** **KE-42**
Työn valvoja **Prof. Ville Alopaeus**	**Sivumäärä** **87**
Työn ohjaaja **Jari Ihonen, TkT; Tanja Kallio, TkT**	**Kieli** **Englanti**
Avainsanat **PEMFC, vedyn kierrätys, ejektorimalli, typen rikastuminen**	**Päiväys** **1.12.2010**

Acknowledgements

This Master's thesis has been made at the Technical Research Centre of Finland in the working group of 'Fuel cells and hydrogen technology' as a part of the TopDrive-project. The focus of the project is in optimization of fuel cell systems for working machine applications.

The instructors of this work were Jari Ihonen at the Technical Research Centre of Finland and Tanja Kallio at the Aalto University, both of whom I wish to thank for many constructive and valuable comments as well as for introducing me to the world of fuel cells. The supervisor of this work, Ville Alopaeus, has also contributed greatly to this work for which I would like to thank him. I also want to thank Matthew Ivity for proofreading.

Moreover, a thankyou goes to all the people working within the TopDrive-project who have helped me during the work. Especially, I want to thank Henri Karimäki who tirelessly has partaken to the experimental work and Timo Keränen who has contributed to the experimental work with his expertise.

Last but not least, I want to thank all the people close to me, especially my wife, for supporting me during the work.

Espoo, December 1, 2010

Kaj Nikiforow

Table of contents

Nomenclature

Roman symbols

A	Area, $[m^2]$
a_j	Activity of species j
c	Speed of sound, $[m/s]$
C_p	Isobaric heat capacity, $[J/K]$
C_v	Isochoric heat capacity, $[J/K]$
ΔC_p	$= \sum(v_j \cdot \mathrm{C}_{p,j})$, change of isobaric heat capacity in a reaction, $[J/K]$
$c_{p,}$	Specific heat capacity, $[J/K\ kg]$
D	Diameter, $[m]$
d	Nominal diameter, $[m]$
E	Voltage, $[V]$
E^0	Standard voltage, i.e. the reversible open circuit voltage at standard state
e	Elementary charge, $1.602 \cdot 10^{-19} C$
F	$= e/N_A$, Faraday constant, $96485\, C/mol$
ΔG	Gibbs free energy change in a reaction, $[J]$
g	Gravitational acceleration, $9.81\ m/s^2$
Δg	Molar Gibbs free energy change in a reaction, $[J/mol]$
Δg^0	Molar Gibbs free energy change at standard state in a reaction, $[J/mol]$
H	Enthalpy, $[J]$
ΔH_r	Enthalpy change in a reaction, $[J]$
ΔH_f^0	$= \sum(v_j \cdot \mathrm{H}_{f,j}^0)$, change of enthalpy of formation at standard state in a reaction, $[J]$
$H_{f,j}^0$	Enthalpy of formation at standard state of species j, $[J]$
h_l	Latent heat, $[J/mol]$
h_w	Specific enthalpy, $[J/kg]$
Δh	Molar enthalpy change in a reaction, $[J/mol]$
Δh_r^0	Molar reaction enthalpy at standard state, $[J/mol]$
I	Current, $[A]$
i	Current density, $[A/cm^2]$
i_0	Exchange current density, $[A/cm^2]$
i_L	Limiting current density, $[A/cm^2]$
K_p	Equilibrium constant
k	Absolute roughness of a pipe

L	Length, $[m]$
M	Mach number
M_w	Molar weight, $[kg/mol]$
$\dot{m}$	Mass flow rate, $[kg/s]$
N_A	Avogadro's constant, $6.022 \cdot 10^{23} mol^{-1}$
n	Number of electrons exchanged, charge number of cell reaction, polytropic exponent
$\dot{n}$	Molar flow rate, $[mol/s]$
P	Power, $[W]$
p	Pressure, $[bar]$
p_{dyn}	Dynamic pressure, $[bar]$
p_j	Partial pressure of species j, $[bar]$
$\dot{Q}$	Heat flux, $[W]$
q	Charge, $[C]$
R	Universal gas constant, $8.3145 J/K\ mol$, $8.3145 \cdot 10^{-5}\ m^3\ bar/K\ mol$
r	Area specific resistance, $[\Omega\ cm^2]$
S_j^0	Entropy of species j at standard state, $[J/K]$
ΔS^0	$= \sum(\upsilon_j \cdot \mathrm{S}_j^0)$, change of entropy at standard state in a reaction, $[J/K]$
ΔS_r	Entropy change in a reaction, $[J/K]$
T	Temperature, $[K]$
t	Time, $[s]$
V	Volume, $[m^3]$
$\dot{V}$	Volume flow rate, $[m^3/s]$
v	Velocity, $[m/s]$
W	Work, $[J]$
x_j	Absolute humidity of gas j
y_j	Mole fraction of species j in gas phase
z	Charge transferred per mole of water generated in a reaction between hydrogen and oxygen
Δz	Elevation, $[m]$
$\emptyset_j$	Relative humidity of gas j

Greek symbols

α	Charge transfer coefficient, net water transport coefficient

β	Impurity build-up factor
ε	A constant in equation (3.4)
ζ	Local flow resistance
η	Overpotential, $[V]$; efficiency
κ	$= \frac{C_p}{C_v}$, isentropic expansion factor
λ_j	Stoichiometric ratio of species j
μ	Viscosity, $[Pa\ s]$
ξ	Friction loss coefficient
ρ	Density, $[kg/m^3]$
υ_j	Stoichiometric coefficient of species j
Φ_j	Utilization of species j
χ	Flow resistance coefficient (includes ζs and ξ)

Superscripts

0	Standard state: 1 bar and 298.15 K
$'$	Isentropic
$a \rightarrow c$	From the anode towards the cathode
s	Gas phase saturated with water

Subscripts

0	Stagnated fluid
a	Anodic, Anode, Activation (overpotential)
c	Cathodic, Cathode, Concentration (overpotential)
d	Diffuser
e	Electrical
gen	Generated
l	Laminar flow
m	Mixed fluid
mix	Beginning of the mixing section
ohm	Ohmic (overpotential)
p	Primary fluid
r	Reaction
s	Secondary fluid
t	Nozzle throat, Turbulent flow
xp	Nozzle exit plane

Abbreviations

BoP	Balance of plant
CEM	Compressor expander module
CHP	Combined heat and power
CL	Catalyst layer
EMF	Electromotive force, a.k.a. the reversible open circuit voltage
EOD	Electro-osmotic drag
EWH	Enthalpy wheel humidifier
FC	Fuel cell
FCS	Fuel cell system
FDS	Fuel delivery system
GDL	Gas diffusion layer
HE	Heat exchanger
HHV	Higher heat value
HOR	Hydrogen oxidation reaction
ICE	Internal combustion engine
LHV	Lower heat value
MEA	Membrane electrode assembly
MH	Membrane humidifier
ORR	Oxygen reduction reaction
PEMFC	Polymer electrolyte membrane fuel cell
PTFE	Polytetrafluoroethylene

1 Introduction

Internal combustion engines (ICE) have for a long time now ruled over the markets of power plants in small and/or mobile applications. Now that the era of abundant crude oil is coming to its end and the environmental impacts of different emissions are recognized, alternative solutions for ICEs are being investigated.

Fuel cells have potential to replace combustion engines in certain applications because of the higher efficiency of fuel cells and the flexibility of the fuel used in them. Polymer electrolyte membrane fuel cells (PEMFC) are especially suitable for mobile applications because of their compact structure and their low operating temperature. However, before widespread commercialization of fuel cells, their durability has to be increased and their cost has to be reduced. The durability and the cost of fuel cells are mainly matters of material development.

A fuel cell system consists of, in addition to fuel cells, auxiliary components and a control system which are required to ensure suitable operating conditions for the fuel cells. The auxiliary components, however, consume energy, thus lowering the overall efficiency of the system. Hence, ongoing research is aiming at material development as well as optimizing and simplifying fuel cell systems.

1.1 Background

This thesis was done for the TopDrive project which is part of the Tekes' Fuel Cell Technology Program (2007-2013). The TopDrive project is a follow-up to the Working PEM project (2007-2009) and the PowerPEMFC project (2004-2006) and is aiming at optimizing fuel cell systems used in working machine applications. The financiers of the project are Tekes (the Finnish Funding Agency for Technology and Innovation), VTT (the Technical Research Centre of Finland), and industry partners in the TopDrive project.

1.2 Problem

In polymer electrolyte membrane fuel cells, the anode exhaust gas is usually recirculated to anode inlet in order to increase fuel utilization and to humidify the anode inlet gas. Recirculation not only consumes energy but also causes impurities (inert gases and contaminants) to build up in the recirculated stream. Because of the impurity build-up, the anode compartment has to be purged occasionally. During the purges, some fuel is lost irrecoverably, thus decreasing fuel utilization. Hence, from fuel utilization point of view, it is advantageous to operate the fuel cell with high impurity content in the recirculated stream. However, high impurity content translates into decreased performance of the fuel cell. In some cases, the detrimental effects of high impurity content in the recirculated stream can be mitigated by increasing recirculation. This, however, translates into increased energy consumption of the recirculation pump.

1.3 Target and approach

The target of this work is to investigate recirculation of anode exhaust gas in a PEMFC especially concentrating on the recirculation rate and the build-up of inert gases. The achievable recirculation rate by using an ejector as the recirculation pump is investigated by modelling an ejector. The ejector model is simulated by varying the flow resistance of the fuel cell stack and the dimensions of the ejector. The inert build-up in the recirculated anode stream, on the other hand, is investigated through experimental work. The rate of inert build-up and the effects of inert build-up on fuel cell stack performance are investigated by operating an 8-kW$_e$ PEMFC system at variable loads and by simulating different fuel qualities by feeding nitrogen together with the fuel feed.

1.4 Thesis outline

The focus of this master's thesis is on the recirculation of anode exhaust gas in a PEMFC system. However, first the fundamentals of fuel cells in general as well as of the PEMFC are presented in chapter 2. In chapter 3, the focus is targeted at the subsystems making up the PEMFC system. Here the different phenomena occurring in a PEMFC and affecting the performance and the durability of the PEMFC as well as the interrelationships between the subsystems are discussed. In chapter 4, the development of an ejector model is described. In chapter 5, the procedure of initial testing of the PEMFC system and the experimental setup of investigating the build-up of inert gases are described. The results from the simulation of the ejector model and from the experimental work are presented in chapter 6 where the results are also discussed. The conclusions are summarized and future work is proposed in chapter 7.

2 Fuel cells

2.1 Fuel cells in general

2.1.1 Working principle and structure of fuel cells

A fuel cell is an electrochemical cell where the available energy between reactants and products is converted into electrical current. This is possible by separating the oxidation and reduction reactions from each other, whereby the electrons transferred in the reaction can be used to do work. Hence, the working principle of a fuel cell is similar to that of a battery. The difference, however, is that while a battery has all the chemical energy stored inside it, the reactants are continuously supplied to a fuel cell. In this sense, the working principle of a fuel cell reminds of that of a combustion engine. The main differences between a fuel cell and a combustion engine are that a fuel cell has no moving parts and is not constrained by Carnot cycle efficiency like combustion engines.

A fuel cell consists of two electrodes, an anode and a cathode, and of an electrolyte, as seen in figure 2.1. The oxidation of the fuel takes place at the anode, and the reduction of the oxidant takes place at the cathode. Depending on the fuel cell type, different ions migrate through the electrolyte which, thus, must be ion conductive.

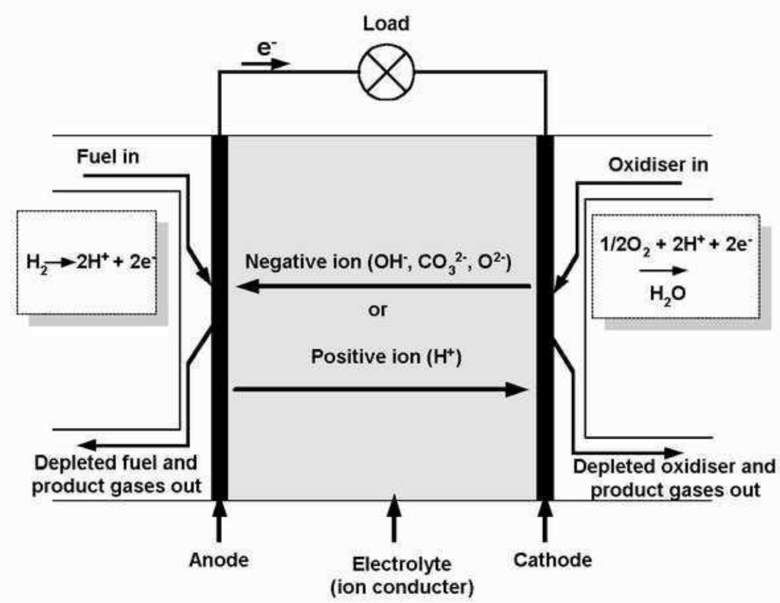

Figure 2.1. The working principle of a fuel cell when hydrogen is used as fuel (Ihonen 2003). Reproduced by the permission of Jari Ihonen.

When hydrogen is used as the fuel, the overall reaction in a fuel cell is either

$$H_2(g) + \frac{1}{2}O_2(g) \rightarrow H_2O(l) \qquad \Delta h_r^0 = -286000 \frac{J}{mol} \tag{2.1}$$

or

$$H_2(g) + \frac{1}{2}O_2(g) \rightarrow H_2O(v), \qquad \Delta h_r^0 = -242000 \frac{J}{mol} \tag{2.2}$$

depending on the operating temperature. The importance of distinguishing between these two reactions is apparent in the context of fuel cell efficiency as the efficiency can be calculated based on either the higher heat value (HHV), reaction (2.1), or the lower heat value (LHV), reaction (2.2).

2.1.2 Thermodynamics and electrochemistry in fuel cells

2.1.2.1 Thermodynamics

The maximum amount of energy that can be used to do electrical work (W_e) is given by the change in Gibbs free energy (ΔG)

$$W_e = \Delta G(T) \tag{2.3}$$

where the Gibbs free energy is calculated as follows

$$\Delta G(T) = \Delta H_r(T) - T\Delta S_r(T) \tag{2.4}$$

where ΔH_r is the enthalpy change in reaction, ΔS_r is the entropy change in reaction, and T is the temperature. The enthalpy change represents the amount of thermal energy available in the reaction, and the term $T\Delta S_r$ represents the amount of unavailable energy resulting from the entropy change within the system. The enthalpy change and the entropy change can be calculated as follows

$$\Delta H_r(T) = \Delta H_f^0 + \int_{T^0}^{T} \Delta C_p dT, \tag{2.5}$$

$$\Delta S_r(T) = \Delta S^0 + \int_{T^0}^{T} \frac{\Delta C_p}{T} dT \tag{2.6}$$

where ΔH_f^0 is the change in enthalpy of formation at standard state, ΔS^0 is the change in entropy at standard state, and ΔC_p is the change in isobaric heat capacity. The Gibbs free energy of a reaction can also be written using the definition of chemical potential as follows

$$\Delta g(T) = \Delta g^0 + RT \, ln \, K_p \tag{2.7}$$

where Δg is the molar Gibbs free energy, Δg^0 is the molar Gibbs free energy at standard state, R is the universal gas constant, $K_p = \prod a_j{}^{\nu_j}$ is the equilibrium constant, and ν_j is the stoichiometric coefficient of species j. For an ideal gas, the activity (a_j) of species j is

$$a_j = \frac{p_j}{p^0} \tag{2.8}$$

where p_j is the partial pressure of species j.

2.1.2.2 EMF & Nernst equation

The electrical work done is the charge (q) multiplied by the voltage (E)

$$W_e = q \cdot E. \tag{2.9}$$

In reactions (2.1) and (2.2), for every mole of product water, two moles of electrons are transferred. Therefore, the charge transferred per mole of water produced is

$$z = \frac{q}{n_{H_2O,gen}} = 2N_A(-e) = -2F \tag{2.10}$$

where N_A is Avogadro's constant, e is the elementary charge, and F is Faraday constant. By combining equations (2.3), (2.9), and (2.10), we arrive at

$$E = -\frac{\Delta g(T)}{2F}. \tag{2.11}$$

Equation (2.11) gives the electromotive force (EMF) or the reversible open circuit voltage of a hydrogen fuel cell. In other words, equation (2.11) is valid when there are no losses in the fuel cell.

By combining equations (2.7), (2.8), and (2.11), we arrive at

$$E = -\frac{\Delta g^0}{2F} - \frac{RT}{2F} ln\, K_P = E^0 - \frac{RT}{2F} ln \prod \left(\frac{p_j}{p^0}\right)^{\nu_j} \tag{2.12}$$

where E^0 is the standard voltage, i.e. the EMF at standard state. Equation (2.12) is also known as the Nernst equation which gives the interdependency between EMF and reactant and product partial pressures as well as the operating temperature. In practice, the reversible open circuit voltage cannot be achieved due to losses occurring in a fuel cell.

2.1.2.3 Voltage losses in a fuel cell

The difference between the EMF and the actual voltage of a fuel cell is caused by four phenomena, namely (1) activation overpotential, (2) concentration overpotential, (3) ohmic losses, and (4) fuel crossover and internal currents.

Activation overpotential is caused by reaction kinetic limitation and can be calculated from the Butler-Volmer equation

$$\frac{i}{i_0} = e^{\alpha \eta_a \frac{nF}{RT}} - e^{(\alpha-1)\eta_a \frac{nF}{RT}} \tag{2.13}$$

where i is the current density, i_0 is the exchange current density, α is the charge transfer coefficient, η_a is the activation overpotential and, n is the number of electrons transferred in the reaction step that limits the kinetics (Murtomäki et al. 2009). The hydrogen oxidation reaction (HOR) is rather fast which results in a low activation overpotential. Hence, by linearizing equation (2.13) close to $\eta_a = 0$, the anode side activation overpotential can be calculated as follows

$$\eta_a = \frac{RT}{nF}\frac{i}{i_{a,0}}. \tag{2.14}$$

In contrast, the activation overpotential of the oxygen reduction reaction (ORR) is known to be much higher. Because the ORR is the cathode reaction in a fuel cell, the anodic term in the Butler-Volmer equation can be omitted, thus arriving at

$$\eta_a = \frac{RT}{(\alpha-1)nF} ln \frac{|i|}{i_{c,0}} \tag{2.15}$$

which is known as the Tafel equation (Murtomäki et al. 2009).

Concentration overpotential occurs when the reaction rate is limited by the rate of mass transport of the reactants to the electrode. Due to the limited mass transport rate, the partial pressure of the reactant at the electrode surface decreases, thus causing the voltage of the fuel cell to drop. This phenomenon is the same as intentionally decreasing the reactant partial pressure on the electrode. Hence, using the Nernst equation, the voltage drop can readily be calculated by introducing the limiting current density, i_L, which is the maximum current that can be drawn from the cell with the mass transport rate available,

$$E_2 - E_1 = \eta_c = \frac{RT}{nF} ln \left(\frac{p_{2,j}}{p_{1,j}}\right)^{\nu_i} = \frac{RT}{nF} ln \left(\frac{i_L}{i_L - i}\right)^{\nu_j}. \tag{2.16}$$

Equation (2.16) is valid when it can be assumed that the partial pressure of the reactant decreases linearly with increasing current density and that the reaction rate is limited only by the rate of mass transport, not by the reaction kinetics. (Sundholm 1987)

Ohmic losses occur due to a resistance in electric conductors and in the membrane. The magnitude of the voltage drop caused by these phenomena can be calculated using Ohm's law as follows

$$\eta_{ohm} = ir \tag{2.17}$$

where r is the area specific resistance.

Fuel crossover and internal currents are phenomena that result from the diffusion of fuel through the electrolyte and the electric conductivity of the electrolyte, respectively. The fuel crossover is the dominating one of these two (Larminie, Dicks 2003).
The fuel crossover, although not very notable in terms of flux, can cause a significant voltage drop especially in low temperature fuel cells. The reason for this is the occurrence of mixed potentials at the cathode. The fuel diffusing through the membrane reacts electrochemically with oxygen to form a waste current. As this reaction is mass transport limited (fuel diffusion), the potential of the cathode is decreased according to equation (2.16). In addition, the activation overpotential of the ORR causes some polarization. (Koryta, Kavan 1987)

2.2 Proton exchange membrane fuel cells

A proton exchange membrane fuel cell (PEMFC) is characterized by its solid polymer electrolyte and its low operating temperature. The polymer membrane as electrolyte is unique among fuel cells and brings several good qualities to PEMFCs. For instance, due to the solid electrolyte, there is no risk of leakage of the corrosive electrolyte, and the electrolyte can be made very thin which makes the construction of PEMFC very compact. The low operating temperature is necessary in a PEMFC because the electrolyte has to be hydrated in order to be proton conductive; indeed, water management is one of the major concerns in PEMFCs. The low operating temperature and the acidic electrolyte necessitates the use of more expensive catalysts, i.e. Pt or Pt-Ru alloys.

A PEMFC consists of different layers which are sandwiched together to form the fuel cell, as seen in figure 2.2. These components are the membrane electrode assembly

(MEA), the gas diffusion layers (GDL), the end plates, and gaskets (Larminie, Dicks 2003).

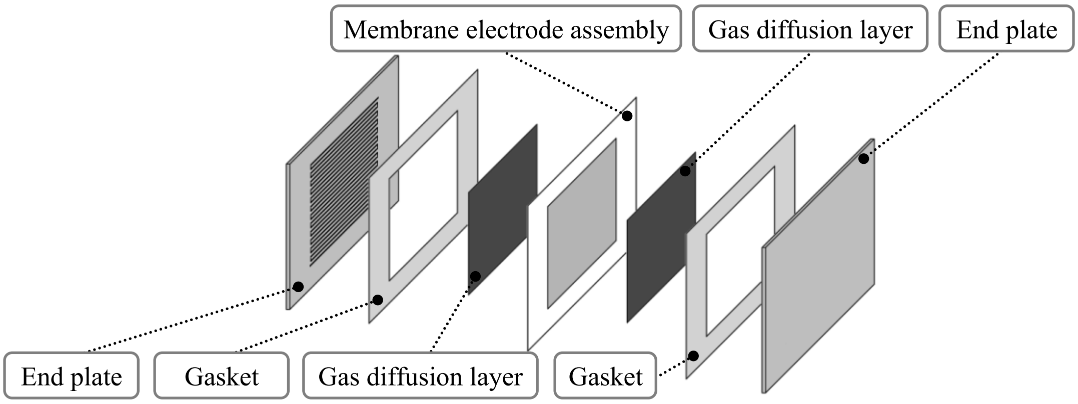

Figure 2.2. The structure of a PEMFC.

The *membrane electrode assembly* is the core of a PEMFC and consists of a polymer membrane (the electrolyte) with thin catalyst layers (electrodes) hot pressed on its both sides. The polymer most commonly used in the membrane is sulphonated polytetrafluoroethylene (PTFE) (Larminie, Dicks 2003) where the PTFE is hydrophobic and the sulphonic groups are hydrophilic. Thus, water filled pathways are formed in the membrane where protons dissociated from the sulphonic groups may move.

One concern in the PEMFCs is the catalyst loading. Even though the catalyst loading has shown a strongly decreasing trend in the past, the long-term availability of platinum, currently the only catalyst suitable for PEMFCs, is still a problem (Larminie, Dicks 2003). On the other hand, the low catalyst loadings have led to issues, such as faster decrease in catalyst activity (Ahluwalia, Wang 2008b).

The purpose of a *gas diffusion layer* is to spread the reactant gases evenly on the electrode as well as to continue the transport of current and water started in the electrode. Therefore, the material used must be porous and electron conductive. The most common materials are carbon cloth and carbon paper. (Larminie, Dicks 2003)

The *end plate*, also known as the bipolar plate, is the current collector. Thus, it is made of a conductive material such graphite or stainless steel (Larminie, Dicks 2003). The end plates have channels formed in them where reactant gases can flow and be distributed over the entire cell. The name ‘bipolar plate’ is actually correctly used only in fuel cell stacks where these plates provide an electrical contact between adjacent cells.

3 Proton exchange membrane fuel cell system

In section 2.1.1, the working principle of fuel cells was introduced, and in section 2.2, the components of a PEMFC were presented. In real fuel cell applications, other components are also needed to ensure that the fuel cell works properly. These components are called the balance of plant (BoP) components. In a PEMFC system, there are four major subsystems needed to operate the fuel cell properly, namely (1) a fuel supply subsystem, (2) an oxidant supply subsystem, (3) a water management subsystem, and (4) a thermal management subsystem. These subsystems are not necessarily self-contained, since the function of one subsystem may affect the function of another subsystem. Therefore, when optimizing the function of one subsystem, the effects on the entire fuel cell system should be taken into account. In this chapter, the four subsystems are introduced and it is discussed how they affect the function of the entire fuel cell system.

3.1 Fuel supply

The purpose of the fuel delivery system (FDS) in a PEMFC is to supply fuel from the storage to the anode of the fuel cell(s). Hence, a FDS consists at least of some equipment to control the flow. Moreover, in case the fuel is recirculated from the anode outlet back to the anode inlet, a recirculation device is needed. Besides the design of the hydrogen supply and recirculation systems, other factors worth considering are hydrogen purity and the build-up of impurities due to hydrogen recirculation as well as the effects of these on the performance and the durability of a fuel cell.

3.1.1 Impurities in hydrogen

Because hydrogen does not occur in its pure form on earth, it must be produced. The most common method for this today is reformation of natural gas or other hydrocarbons (Cheng et al. 2007). Depending on the method of producing hydrogen, different impurities might be present and in varying concentrations. For example, the reformate hydrogen contains impurities such as carbon dioxide, carbon monoxide, sulphur compounds (e.g. H_2S), ammonia, and methane (Cheng et al. 2007). The impurities might be either inert or contaminants. While the inert impurities (e.g. N_2, Ar, CO_2) do not affect the operation of a fuel cell other than through decreased partial pressure of fuel, the contaminants poison the fuel cell either reversibly or irreversibly. The nature of the effects of the contaminants depends, besides on the compound in question, also on the exposure time and the concentration of the contaminant. (Cheng et al. 2007)

In a PEMFC, the MEA is the most prone to be affected by contaminants. The effects of the contaminants on the MEA activity include (1) decreased catalytic activity through adsorption of the compound (e.g. CO, H_2S) on the catalyst, (2) decreased proton concentration in the membrane and, hence, increased resistance due to proton binding compounds (e.g. NH_3), and (3) increased mass transport resistance due to compounds that change the catalyst layer structure and hydrophobicity. (Cheng et al. 2007)

The above mentioned effects can be mitigated through (1) pre-treatment of the hydrogen, (2) material development and optimized operating conditions, and (3) regeneration of the affected material.

The pre-treatment of hydrogen is often done in some extent to remove most of the impurities left from the manufacturing process. Even though practically all impurities can be removed from hydrogen through pre-treatment (Papadias et al. 2009), it is not often economically feasible due to the costs of pre-treatment and due to the poor recovery of hydrogen. Thus, the task is to find an optimal level of impurities which can be tolerated in a fuel cell.

The discovery of CO-tolerant catalysts, e.g. Pt-Ru alloys, is one example of the fruits of material development in mitigating the effects of contaminants (Cheng et al. 2007). While Pt-Ru alloys do not completely remove the problem of CO adsorption, they make desorption of CO easier. The same effect can be achieved by increasing the operating temperature.

The third contamination mitigation strategy is to regenerate the contaminated material. One example of this is air-bleeding in which a small amount of air is mixed in the hydrogen stream to oxidize the CO adsorbed on the anode catalyst. (Cheng et al. 2007)

3.1.2 Hydrogen storage

The use of hydrogen as fuel is advantageous due to the clean oxidation and the high specific energy[1] of hydrogen. However, from the storage point of view, hydrogen has some drawbacks which include the low energy density[2] and the high leak rate of hydrogen. These drawbacks stem from the properties of hydrogen which include the

---

[1] Energy content of hydrogen/mass of hydrogen

[2] Energy content of hydrogen/volume of hydrogen

highest molecular mean velocity as well as the lowest viscosity and density of all gases. (Larminie, Dicks 2003)
Hydrogen can be stored in several ways: pure hydrogen can be stored either pressurized or liquefied, hydrogen may be adsorbed onto a carrier, or it can be stored as a chemical compound. These methods of hydrogen storage differ in size and weight, in hydrogen pressure, in hydrogen temperature, as well as in the need of pre-processing hydrogen before supplying it to the fuel cell.

Storing hydrogen pressurized is the most straightforward method due to the well-known technology. Because of the low density of hydrogen, a quite high storage pressure is often used in order to save space. The high pressure makes the storage tanks heavy, and the gravimetric density[3] is consequently quite poor (Sakintuna, Lamari-Darkrim & Hirscher 2007).
When storing hydrogen pressurized, a phenomenon called hydrogen embrittlement is possible. This phenomenon might lead to a crack in the tank wall which together with the high leak rate of hydrogen might in an extreme case result in a jet-propelled torpedo. Nevertheless, storing hydrogen under pressure is relatively safe. The advantages of this storage method include its simplicity, the indefinite storage time, and that there are no purity limits of the hydrogen stored. (Larminie, Dicks 2003)

By liquefaction of hydrogen, a higher density of hydrogen and, thus, a higher gravimetric density of the storage can be obtained. However, compared to other liquids, cryogenic hydrogen has a very low density, only 70.5 kg/m^3 at boiling point (Perry 1997). In addition, liquefaction of hydrogen requires more than 25 % of the specific enthalpy of the hydrogen liquefied (Larminie, Dicks 2003; Sakintuna, Lamari-Darkrim & Hirscher 2007; Ross 2006). Furthermore, some hydrogen has to be evaporated continuously to account for the heat losses of the storage (Ahluwalia, Peng 2008; Ross 2006). In conclusion, this storage method is highly energy-inefficient.
Liquefaction of hydrogen as a storage method is mostly used to store large quantities of hydrogen. In addition, some car manufacturers have investigated the possibility of using liquid hydrogen as fuel in hydrogen-powered cars propelled by an ICE. The advantage of using cryogenic hydrogen in an ICE is that hydrogen may be fed in liquid state, whereas hydrogen used in fuel cells has to be gaseous. (Larminie, Dicks 2003)

Hydrogen can also be stored by adsorbing it onto a metal (metal hydride). There are several alternatives for the metal used in this storage method especially alloys of

---

[3] Mass of hydrogen/mass of storage

titanium, iron, nickel, manganese, and chromium (Sakintuna, Lamari-Darkrim & Hirscher 2007). The advantages of metal hydrides as a storage method include the slow spontaneous discharge (safety), the high volumetric storage density, as well as the modest temperature and pressure of the storage (Sakintuna, Lamari-Darkrim & Hirscher 2007). However, metal hydrides are sensitive to impurities, they have to be charged relatively slowly, and the gravimetric density of metal hydride storage is quite poor (Larminie, Dicks 2003). These properties make the metal hydrides suitable for applications where small quantities of hydrogen are stored or when other methods are not acceptable due to safety reasons.

Another material that can adsorb hydrogen is carbon. Different forms of carbon used for storing hydrogen include activated carbons, carbon nanotubes, and carbon nanofibres (Sakintuna, Lamari-Darkrim & Hirscher 2007). In recent years much interest has been targeted at carbon nanostructures (Chambers et al. 1998) which, however, have not yet lived up to the expectations.

Besides storing hydrogen pressurized, liquefied, and adsorbed onto a carrier, it can also be stored as various chemical compounds: ammonia, methanol, ethanol, hydrazine, alkali metal hydrides (e.g. lithium hydride), and borohydrides (e.g. sodium borohydride, $NaBH_4$). The advantage of storing hydrogen as chemical compounds is the high hydrogen density. However, the problem with many of the above mentioned compounds is that they are too expensive to manufacture, very toxic, or very caustic (Larminie, Dicks 2003). In addition, they all need some processing to release the hydrogen. For example, sodium hydride and sodium borohydride release hydrogen during a reaction with water (Ross 2006), hydrogen in methanol can be extracted through steam reformation or partial oxidation (Balat 2008), and ammonia dissociates into nitrogen and hydrogen in very high temperatures (up to 1000 °C) (Li, Hurley 2007).

Due to the very different properties of the storage methods presented here, it is difficult to make a comparison between them. Nevertheless, Ahluwalia et al. have made a case study about different storage methods, and concluded that the highest Well-to-tank efficiency is achieved by storing the hydrogen pressurized (Ahluwalia, Hua & Peng 2007). However, the choice of the storage method for a fuel cell application should be done taking into account other factors as well such as suitability of the storage system from the application point of view.

3.1.3 Hydrogen supply and recirculation

The way in which hydrogen supply is realized depends mainly on the hydrogen storage method used. As storing hydrogen pressurized is the most common, other methods are not considered here.

When hydrogen is released from high pressure, there is no need for pumps or compressors as on the cathode side of the fuel cell. Furthermore, if the fuel cell is operated at low pressure and in a dead-end mode, no control is needed. Thus, the only equipment needed to supply hydrogen is essentially a pressure regulator and a valve.

However, in real applications, the hydrogen is usually fed in excess to avoid hydrogen starvation[4]. The unspent hydrogen otherwise lost can be recirculated back to the anode inlet where it is combined with the fresh hydrogen feed stream. The recirculation of the unspent hydrogen also humidifies the anode inlet gas, thus making an external humidifier unnecessary and simplifying the FDS. On the other hand, recirculation of hydrogen consumes energy and causes impurities to build up in the recirculated stream. These drawbacks of hydrogen recirculation are addressed in this section.

3.1.3.1 Ejectors – alternative for pumps

An ejector is a jet pump which does not consume any electricity. Instead, the pressure energy of a primary fluid is used to pump a secondary fluid. The pumping is based on accelerating the high pressure primary fluid through a nozzle (McKetta 1983), thus decreasing its pressure. When the pressure of the primary fluid is low enough, the secondary fluid will be entrained and the fluids are mixed. After this, the fluid mixture is decelerated which results in a pressure increase.

The main parts of an ejector are (1) the nozzle, (2) the suction chamber, (3) the mixing section, and (4) the diffuser. The structure of an ejector is shown in figure 3.1.

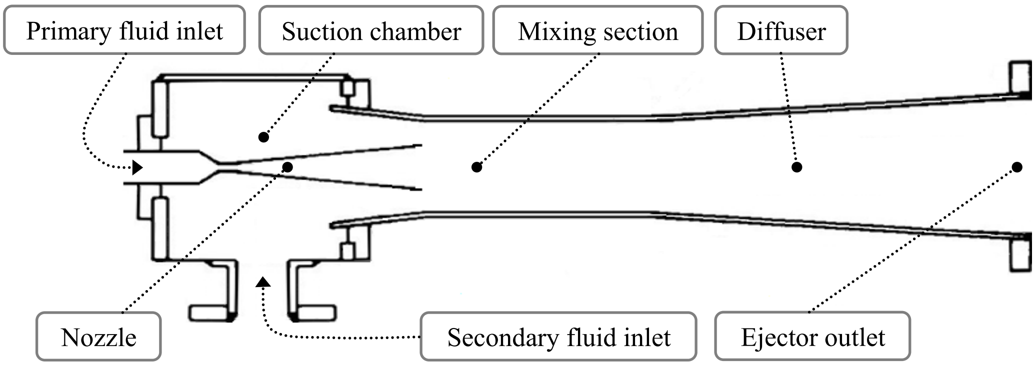

Figure 3.1. The structure of an ejector (figure modified) (McKetta 1983).

---

[4] See section 3.1.4

In the *nozzle*, the primary fluid is accelerated from a high stagnation pressure to a high velocity. The nozzle may consist either of just a convergent part or of both a convergent and a divergent part. The latter type of nozzle is called a 'De Laval' nozzle. Supersonic velocity of the fluid may only be reached in a De Laval nozzle, since the fluid at sonic velocity accelerates in a diverging duct but decelerates in a converging duct. (Perry 1997) Thus, sonic velocity is reached at the nozzle throat if the pressure at this point is high enough.

In order to reach a supersonic velocity in the nozzle, the static pressure of the primary fluid at the nozzle throat has to be higher than the stagnation pressure of the secondary fluid. If this condition holds, the primary fluid is accelerated further in the diverging part of the nozzle. (Perry 1997) As the increase in velocity and the decrease in static pressure go hand in hand, the minimum in primary fluid pressure is at the nozzle exit plane.

The nozzle exit plane is in the *suction chamber*. Here a low pressure region is created due to the low pressure primary fluid flowing out of the nozzle. Because of the pressure difference between the nozzle exit plane and the secondary fluid, the secondary fluid flows towards the primary fluid and is eventually entrained (He, Li & Wang 2009).

The fluids are often assumed to flow from the suction chamber to the *mixing section* without being mixed. Only in the mixing section, when the pressure of the secondary fluid has decreased to that of the primary fluid, the fluids mix. (Munday, Bagster 1977) After mixing, if the velocity of the mixture is supersonic, the uniform mixture of fluids undergoes a shock and chokes. When a fluid chokes, the pressure of the fluid suddenly increases while at the same time the velocity decreases to a subsonic value.

After leaving the mixing section, the subsonic fluid enters a *diffuser*. The purpose of a diffuser is exactly the opposite to that of a nozzle: to decrease the velocity of the fluid (He, Li & Wang 2009). This is done by letting the fluid flow in a diverging duct. The idea of a diffuser is to convert all the kinetic energy of the fluid back to pressure energy.

3.1.3.2 Recirculation of hydrogen – pump vs. ejector

The use of an ejector to recirculate the anode gas is more energy-efficient in systems where hydrogen is stored pressurized, since the ejector uses this pressure energy for pumping and, hence, does not need any electric power. Other advantages of an ejector include its rigid and simple construction which make it very reliable and lasting (McKetta 1983). Furthermore, an ejector has no moving parts and, thus, do not need any lubrication and very little maintenance (McKetta 1983). However, the function of an ejector depends strongly on its geometry which means that it works only at a relatively narrow range of flow rates (Ahluwalia, Wang 2008b). Moreover, in order for the ejector to work as a recirculation pump, hydrogen must continuously be consumed in the fuel cell.

A pump, on the other hand, can be very flexible when it comes to the need of changing the flow rate. However, this flexibility comes at the expense of the efficiency of the pump, since the efficiency is flow rate dependent. The main drawback of a pump compared to an ejector is that it needs electric power to run. In addition, with a pump, the pressure energy of the hydrogen storage is lost.

By using an ejector and a pump in parallel, the advantages of both of them can be utilized – the pump is needed only at flow rates that are outside the working range of the ejector (Ahluwalia, Wang 2008b). In this case, the control is of crucial importance. Another way to mitigate the problems with an ejector is to hybridize the fuel cell system, i.e. to use a battery and/or a super capacitor in parallel with the fuel cell. In hybridized systems the energy output of a fuel cell can be relatively constant which is ideal from the point of view of using an ejector. Nevertheless, a pump might be needed in hybridized systems during start-up and shut-down.

3.1.3.3 Build-up of impurities

As discussed in section 3.1.1, the hydrogen used as fuel in PEMFC might contain impurities. These impurities stem from the production or the distribution of hydrogen. In addition, some impurities, e.g. nitrogen and SO_2, can diffuse through the membrane from the air stream fed to the cathode. The rate of the gas crossover from the cathode to the anode depends on several parameters such as the power level, the concentration of the impurity in the anode gas, the purge rate, and the membrane thickness. (Ahluwalia, Wang 2007)

As a result of the recirculation of unused hydrogen, impurities are enriched in the recirculated stream. Without occasional purging the concentration of these impurities will build-up, thus leading to decreased performance of the fuel cell. (Ahluwalia, Wang 2007; Papadias et al. 2009) By establishing a mole balance over the anode side of the fuel cell, the effects of the recirculation rate and the amount of anode gas purged on the build-up of impurities can be examined by introducing the *impurity build-up factor* defined as follows

$$\beta = \frac{y_{impurity,FC,in}}{y_{impurity,feed}} \tag{3.1}$$

where $y_{impurity}$ is the mole fraction of the impurity. Figures 3.2 (a) and (b) show β as a function of hydrogen utilization per pass, Φ_{H_2}, and hydrogen net utilization, $\Phi_{H_2,net}$, respectively.

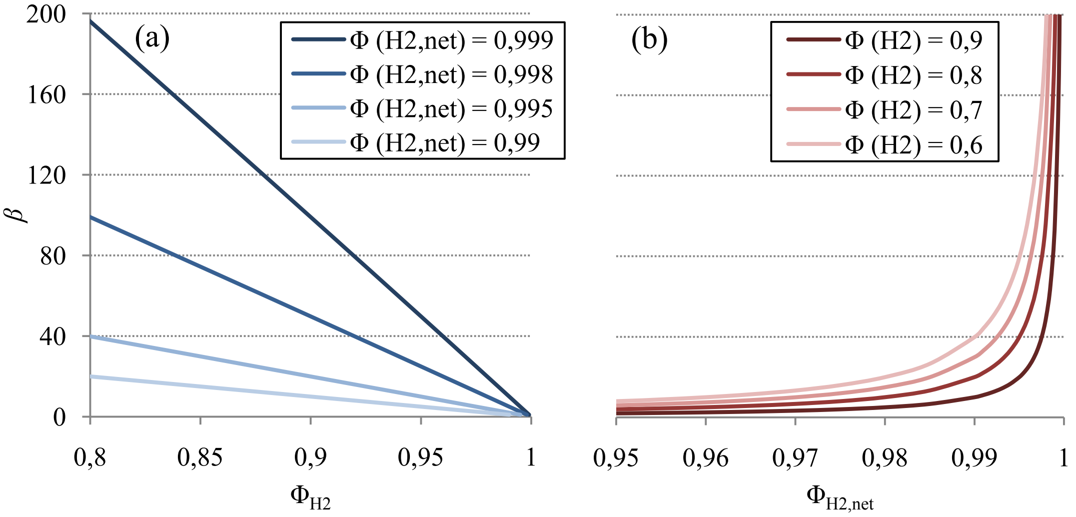

Figure 3.2. The impurity build-up factor as a function of hydrogen utilization per pass (a) and as a function of hydrogen net utilization (b).

From figures 3.2 (a) and (b), it can be deduced that the minimum level of impurities is obtained when there is no recirculation of the hydrogen, i.e. when all the unconsumed hydrogen is purged. This is an ideal situation if the net utilization of hydrogen is 100 %. However, as already mentioned, hydrogen is often fed in excess and recirculated to avoid hydrogen starvation and to increase fuel utilization, respectively.

Figure 3.2 (a) shows a very intuitive fact; as the recirculation is increased, i.e. when Φ_{H_2} is decreased, the mole fraction of impurities in the gas entering the fuel cell is increased. This stems from the changed mixing ratio of recirculated gas and fresh hydrogen. The increased hydrogen recirculation rate also increases the impurity recirculation rate, thus decreasing the mass transport resistance. Hence, the nature of the impurity determines whether the increased recirculation rate increases the performance of the fuel cell or accelerates the poisoning of the fuel cell.

From figure 3.2 (b), it can be seen that when decreasing the amount of gas purged, i.e. when increasing $\Phi_{H_2,net}$, the build-up of impurities is increased. Hence, the achievable $\Phi_{H_2,net}$ is ultimately determined by the allowable impurity content in the recirculated stream. In other words, there is an optimum purge rate; with a purge rate higher than the optimum, the use of hydrogen is inefficient, and with a purge rate lower than the optimum, the build-up of the impurity causes a reduction in cell performance (Ahluwalia, Wang 2007; Ahluwalia, Wang 2008a). The optimum purge rate is most likely different for different impurities. Therefore, the purge rate has to be optimized based on the purity of the available hydrogen.

3.1.4 Hydrogen starvation on PEMFC anode

Hydrogen starvation occurs when hydrogen is no longer available at the anode to be oxidized. When this happens, the potential of the anode will rise to that needed to oxidize water

$$H_2O(l) \rightarrow \frac{1}{2}O_2(g) + 2H^+(aq) + 2e^-. \tag{3.2}$$

At this potential and in the presence of platinum catalyst, the carbon support of the anode catalyst will be oxidized by water

$$C(s) + 2H_2O(l) \rightarrow CO_2(g) + 4H^+(aq) + 4e^-. \tag{3.3}$$

As a result of reaction (3.3) the carbon support of the anode catalyst is converted into CO_2 and catalyst particles are lost. Thus, the performance of the fuel cell is lost irrecoverably. (Knights et al. 2004)

Besides damaging the catalyst layer, the hydrogen starvation lowers the cell potential to a negative value. This means that the energy required to run reaction (3.3) is taken from other cells besides the hydrogen starved cells in the fuel cell stack. (Knights et al. 2004)

Hydrogen starvation might occur as a result of inert gas build-up, during load peaks, or when hydrogen is distributed unevenly between the cells in the stack. Uneven hydrogen distribution can occur when the flow resistance varies between cells and might be a result of poor water management (flow channels flooding or ice formation during sub-zero operation).

3.2 Oxygen supply

Oxygen can be supplied to the fuel cell either as pure oxygen or as air. The advantage of using pure oxygen instead of air includes the increased performance of the fuel cell because of the higher partial pressure of oxygen and because of the lower concentration of contaminants. On the other hand, the advantages of using air instead of pressurized oxygen include increased safety, decreased space requirements, and that there is no need to refuel (Cunningham 2001).

The choice of the oxidant affects also the water balance. When using air, the flow rate on the cathode is considerably higher than when using pure oxygen. This affects the removal of water vapour from the cathode. Moreover, the linear gas velocity affects the removal of water droplets from the flow channels (Anderson et al. 2010). Because of this, when using pure oxygen, recirculation might be necessary in some channel designs, thus adding complexity to the system.

In practice, the use of pure oxygen is limited to niche markets in space and submarine applications. Because of this, the use of pure oxygen as the oxidant is not considered here. The air supply system in a typical multi-kW fuel cell system consists of a blower or a compressor, an air filter, and a humidifier. In addition, some instruments, such as oxygen sensors and thermometers, might be necessary to effectively control the air supply.

In this section, the factors in the air supply affecting the anode side of the fuel cell are discussed. These factors include the choice of air supply equipment, since the flow rate, the temperature, and the pressure of the air affects the water balance. Another factor affecting the anode side is the contaminants in air which when diffusing through the membrane, will build up in the recirculated anode stream. The oxygen starvation is also covered briefly.

3.2.1 Contaminants in air

While the contaminants in hydrogen primarily stem from the manufacturing process and the distribution of the hydrogen, the sources of the contaminants in air are mainly traffic and industry (Cheng et al. 2007). Contaminants in air include carbon oxides, nitric oxides, benzene, 1,3-butadiene, sulphur oxides, dust, and ozone (Cheng et al. 2007; Ihonen, Keränen 2007). When the air is compressed before being fed into the fuel cell, some compressor lubricants might also be present in the air (Cheng et al. 2007).

In certain applications other contaminants might also come into question. For example, in harbours, the contaminants that might come in contact with the fuel cell include sea salts and different chemical fumes. In mines, there might be carbon monoxide, nitric oxides, ammonia, and diesel fumes in the air. In military applications, the fuel cell has to withstand different battlefield pollutants. (Ihonen, Keränen 2007)

As with the contaminants in hydrogen, the contaminants in air also have various effects on the fuel cell. However, most interest in literature is shown towards the effects of contaminants on the MEA and especially on the catalyst. A few of the studies are briefly reviewed here.

Nitric oxides have been shown to have a reversible effect on fuel cell performance (Yang et al. 2006; Mohtadi, Lee & Van Zee 2004). It is suggested that nitric oxides either adsorb weakly on the Pt catalyst (Yang et al. 2006) or that protons reduce nitrogen dioxide to ammonium which competes with oxygen for the Pt sites (Mohtadi, Lee & Van Zee 2004).

Sulphur containing compounds (H_2S and SO_2) have shown profound poisoning effect on platinum. Both H_2S and SO_2 adsorb on the catalyst so strongly that only partial recovery is possible by purging with neat air (Mohtadi, Lee & Van Zee 2004). There are also studies that suggest that sulphur dioxide adsorbs reversibly but this is considered to occur only when the catalyst is exposed to a relatively low concentration of SO_2 (Mohtadi, Lee & Van Zee 2004; Moore et al. 2000).

The effects of typical battlefield pollutants on PEMFC performance have been studied by Moore et al.. The pollutants included in the study were propane, HCN, CNCl, sulphur mustard, and sarin. Moore et al. found out that all compounds except propane showed a profound and irreversible poisoning effect on the PEMFC. (Moore et al. 2000)

Contamination mitigation strategies on the cathode side include filtration of the air, shut-down of the fuel cell system, and improvement of catalyst durability. The development of air filters has not been going on for very long, and only a few published studies (Kennedy et al. 2007; Ma et al. 2008) about the topic are available. The recent trend of increasing the operating temperature of PEMFCs has a positive effect on contamination mitigation, since the temperature affects the equilibrium of adsorption.

3.2.2 Air supply

The air supply to the fuel cell can be realized by either using a compressor or a blower or by free-breathing. The decision of which of these air supply methods to use depends mainly on the operating pressure as well as on the size of the fuel cell. Free-breathing fuel cells come into question only when the power demand is very low as well as in laboratory tests. Thus, this type of air supply is not considered here.

The two main classes of fluid moving devices suitable for the use in fuel cell systems are positive displacement devices and kinetic devices. These two classes of fluid moving devices differ in how they move the fluid. Positive displacement devices trap a volume of fluid and then discharge it, thus forcing the fluid to move. Kinetic devices add kinetic energy to the fluid which then can be used to move the fluid. (Perry 1997)

The drawback with positive displacement devices is that they produce a fluctuating flow if the volume trapped is large compared to the total volume of gas in the exhaust. This is not very suitable for fuel cell applications because when the flow rate fluctuates, so does also the pressure. In this sense, kinetic devices, e.g. radial blowers or centrifugal compressors are more suitable for fuel cell applications.

Another requirement for the fluid moving device used in a fuel cell system is that it should be oil-free. If the air pumped is mixed with lubricants, the fuel cell might be poisoned and its performance might decrease. In addition, care should be taken when choosing the air supply equipment as the flow rate, the pressure, and the temperature have a profound effect the water balance in the fuel cell.

3.2.2.1 Radial blower

A radial blower adds kinetic energy to the fluid by a rotating impeller. Centrifugal forces drive the fluid radially outwards where it is eventually discharged. Simultaneously, fluid is sucked axially from the centre of the devise to replace the discharged fluid. (Perry 1997)

Radial blowers come with three different blade designs, namely (1) straight blades, (2) forward curved blades, and (3) backward curved blades. Straight blades are best suited for high temperature gases and low rotation speeds. Forward curved blades discharge the gas at high velocity but at low pressure, and the backward curved blades provide the highest discharge pressure but at low velocity. The work done in a blower can be calculated as follows

$$W = \varepsilon \cdot V \cdot p_{dyn} \tag{3.4}$$

where ε is a constant, V is the volume of gas, and p_{dyn} is the dynamic pressure of the discharged gas (Perry 1997).

3.2.2.2 Centrifugal compressor

The working principle of a centrifugal compressor is exactly the same as that of a radial blower. Thus, the difference between radial blowers and centrifugal compressors is not unambiguous. However, compressors can handle larger volumes of fluid, and the discharge pressure is higher. These differences mean that a compressor rotates at a higher speed and that the construction of a compressor is tighter, thus making it more expensive to manufacture. (Perry 1997)

Centrifugal compressors have a special impeller design which compresses the gas while it is driven radially outwards due to the centrifugal force. The rest of the compression is done in the stationary diffusers before discharge. (Perry 1997)

When a gas is compressed, pV^n remains constant. Thus, the relationship between input and output temperatures and pressures for a prefect gas becomes

$$\frac{T_2}{T_1} = \left(\frac{p_2}{p_1}\right)^{\frac{n-1}{n}}. \tag{3.5}$$

The polytropic exponent, n, depends on the nature of compression. For instance, when compression is done isothermally, n is 1, and when the compression is done adiabatically, $n = \kappa = \frac{C_p}{C_v}$ where C_p is the isobaric heat capacity and C_v is the isochoric heat capacity. The work done during compression is

$$W = \int_1^2 pdV \tag{3.6}$$

which for a prefect gas and isothermic compression becomes

$$W = p_1 V_1 \, ln \frac{p_2}{p_1}. \tag{3.7}$$

For an adiabatic compression, the work done is

$$W = \frac{\kappa}{\kappa - 1} p_1 V_1 \left[\left(\frac{p_2}{p_1}\right)^{\frac{\kappa-1}{\kappa}} - 1 \right] = C_p(T_2 - T_1). \tag{3.8}$$

(Perry 1997) The reference for compression efficiency is normally taken to be adiabatic and frictionless, i.e. isentropic compression. Thus, the efficiency of compression is

$$\eta_{compression} = \frac{W'}{W} = \frac{T_2' - T_1}{T_2 - T_1} \tag{3.9}$$

where T_2' is the isentropic output temperature and T_2 is the actual output temperature. In practice, T_2 is always higher than T_2' due to friction losses in the compressor. (Larminie, Dicks 2003)

3.2.2.3 Expander

The compressor consumes quite much power, according to some studies even 20 to 25 % of the power generated by the fuel cell stack (Blunier, Miraoui 2005; Blunier et al. 2008), and the pressure of gas leaving the fuel cell is quite high. To recover the pressure energy otherwise lost, an expander can be used.

Expanders, also known as turbines, come in two constructions: axial flow and radial flow expanders. Axial flow expanders are primarily used in multistage expanders because of the simpler arrangement of the flow path. Radial flow expanders are an

inverse of centrifugal compressors and work at higher efficiencies than axial flow expanders. Thus, most of the expanders are of the radial flow type. (Perry 1997)
Because the expansion is essentially the reverse of compression, most of the equations presented above (3.5 – 3.8) are valid also for expansion. However, equation (3.9) does not hold. Instead, the efficiency of an expansion is defined as follows

$$\eta_{expansion} = \frac{W}{W'} = \frac{T_1 - T_2}{T_1 - T_2'} \tag{3.10}$$

(Larminie, Dicks 2003).

3.2.2.4 The decision of air supply equipment

The main problem with a blower or a compressor is that they consume a lot of energy compared to other equipment in a fuel cell system (Ahluwalia, Wang 2008b) and that the efficiency is quite poor except for a narrow range of flow rates (Larminie, Dicks 2003). There are three alternative combinations of air supply equipment, namely (1) a blower, (2) a compressor, and (3) a compressor expander module (CEM). The bottom line in choosing between these is the benefits gained versus the energy lost. The amount of useful energy in terms of voltage lost when using a compressor can be calculated based on equation (3.8) as follows

$$\Delta E_{lost} = \frac{\lambda_{O_2}}{4F \cdot y_{O_2}} \cdot \frac{\bar{c}_p \cdot T_{in}}{\eta_{compression}} \left[\left(\frac{p_{out}}{p_{in}} \right)^{\frac{\kappa - 1}{\kappa}} - 1 \right] \tag{3.11}$$

where λ_{O_2} is the stoichiometric ratio of oxygen, y_{O_2} is the mole fraction of oxygen in the feed gas, $\bar{c}_p$ is the average molar isobaric heat capacity of the gas, and $\eta_{compression}$ is the total efficiency of compression including compression and compressor motor efficiencies. On the other hand, the energy gain in terms of voltage can be calculated based on equation (2.16) as follows

$$\Delta E_{gain} = \frac{RT_{FC}}{4F} ln \left(\frac{p_{FC,2}}{p_{FC,1}} \right). \tag{3.12}$$

These calculations can also be done for the rest of the three alternatives. However, comparison between the three supply systems is hard due to the facts that the actual voltage gain calculated from equation (3.12) is system dependent (Blunier, Miraoui 2005) and the efficiencies of the compressor, the blower, and the expander are highly dependent on flow rates as well as on the equipments themselves. Thus, the decision of the air supply system should be made based on expected operating conditions of the fuel cell.

Nevertheless, some comparison between a blower and a compressor can be made. A blower is considerably less expensive than a compressor, consumes less power, is less noisy, and is more durable (Mallant, R. K. A. M. 2003). The main reason for preferring a blower over a compressor is that there simply are not available compressors efficient enough in the size ranges needed in small systems (Mallant, R. K. A. M. 2003). On the other hand, the choice of air supply equipment affects also the water balance through the temperature and the pressure of the compressed gas. For example, based on equation (3.5), the resulting temperature of pressurizing ambient air (293 K, 1.013 bar) to 2.5 bar is close to 100 °C when assuming an efficiency of 100 %. This will inevitably cause dehydration of the membrane at the air inlet unless addressed somehow.

A comparison between using a blower and a compressor has also been made by Cunningham et al.. They found out that to achieve the same net power with a fuel cell system (FCS), a remarkably larger stack is needed when using a blower instead of a compressor. However, the system net efficiency was found to be 1,5-2,0 percentage points higher over most of the net power range of the FCS when using a blower compared to when using a compressor. Based on this study, the choice between a blower and a compressor depends on stack cost versus compressor cost. (Cunningham, Hoffman & Friedman 2001)

In another study by Cunningham, an air supply system consisting of a compressor was compared to an air supply system consisting of a CEM. It was concluded that the use of an expander results in an improved system efficiency at peak power levels as well as in an increased peak net power when using the same stack size. However, at low power levels the net efficiency was almost unchanged. Moreover, when using an expander, the control methods become more complex. (Cunningham et al. 2000)

As a conclusion, based on the studies reviewed above, it can be stated that from the system overall efficiency point of view, using a CEM is more advantageous compared to using a blower when the fuel cell system is operated at high power levels most of the time. However, finding an optimal air supply setup can often be quite demanding because of the fluctuating power demand in PEMFC systems. By hybridizing the FCS, optimization of the air supply system becomes easier, since hybridized PEMFC system can be operated at nearly constant power output.

3.2.3 Oxygen starvation

Oxygen starvation might occur in a PEMFC especially during transient conditions due to poor water management, due to small geometric deviations in the flow channel geometry, or due to thermal inhomogeneities (Rodatz et al. 2004). However, the effect of oxygen starvation is not as severe as that of hydrogen starvation.

Oxygen starvation occurs when there is not enough oxygen on the cathode to react with protons and electrons. Thus, protons and electrons react to form hydrogen, and the cell works as a proton pump (Knights et al. 2004). Naturally, the cell where oxygen starvation occurs does not do any work but consumes energy produced by other cells.

In contrast to the hydrogen starvation, oxygen starvation does not directly result in catalyst degradation but may cause very uneven currents distribution leading to overheating and degradation if prolonged. Oxygen starvation is also more difficult to avoid, since it depends on the air supply rate which must be controlled actively.

3.3 Water management

In order to be proton conductive, the electrolyte in a PEMFC needs to be hydrated. This is because protons move in the hydrated parts of the membrane via dissociation of sulfonic acid bonds. When water is not present, the sulfonic acid bonds cannot dissociate, the protons cannot migrate, and the conductivity of the electrolyte decreases. Decreased conductivity of the electrolyte is observed as increased voltage losses that are ohmic in nature. (Ji, Wei 2009)

Ideally, the water formed on the cathode would suffice to maintain the electrolyte membrane hydrated; water would diffuse from the cathode to the anode to achieve an adequate hydration level in the whole electrolyte, and excess water would be flushed away with the cathode gas. However, the actual situation is not as simple as this because of several factors affecting the water balance in a PEMFC. Therefore, humidification of the fuel and the oxidant are necessary to achieve an even water distribution throughout the cell. In this section, the factors affecting the water balance, the methods for guaranteeing a correct water balance, and the consequences of incorrect water balance are introduced.

3.3.1 Water balance

The water balance within the cell is affected by the humidity of the inlet gases, the operating conditions (temperature, pressure, and flow rates), the rate at which water is generated at the cathode (i.e. the current density), as well as the water transport in the membrane. These factors are discussed next.

3.3.1.1 Water sources

In a PEMFC, the sources of water are the electrochemical reaction taking place on the cathode and the humidity entering the fuel cell with the reactant gases. As mentioned in section 2.1.1, for every two moles of electrons transferred from the anode to the cathode, one mole of water is produced. Hence, according to Faraday's law, the rate of water production is

$$\dot{n}_{H_2O,gen} = \frac{I}{2F} \tag{3.13}$$

where I is the current drawn from the fuel cell.

Due to the rather high vapour pressure of water at normal operating temperatures of a PEMFC, the gases leaving the fuel cell carry quite much moisture and, hence, the inlet gases have to be humidified to ensure an adequate hydration level of the membrane. The absolute humidity of a gas is commonly given as mass of water per mass unit of dry gas

$$x_j = \frac{\dot{m}_{H_2O}}{\dot{m}_j} \tag{3.14}$$

where $\dot{m}_{H_2O}$ is the mass flow rate of water and $\dot{m}_j$ is the mass flow rate of the dry carrier gas. Using mole fractions and molar weights of water and the carrier gas, equation (3.14) can be written as follows

$$x_j = \frac{M_{w,H_2O} \cdot p_{H_2O}}{M_{w,j} \cdot (p_{total} - p_{H_2O})} \tag{3.15}$$

where M_{w,H_2O} is the molar weight of water, $M_{w,j}$ is the molar weight of the carrier gas, p_{H_2O} is the partial pressure of water, and p_{total} is the total pressure of the gas mixture. The relative humidity, $\emptyset_j$, is defined as the ratio of water partial pressure to saturated vapour pressure at a given temperature

$$\emptyset_j(T) = \frac{p_{H_2O}}{p^s_{H_2O}(T)} \cdot 100\%. \tag{3.16}$$

Using equations (3.15) and (3.16), the molar flow rate of water entering the fuel cell with the reactant gases can be expressed as follows

$$\dot{n}_{H_2O,in} = \frac{\emptyset_j \cdot p^s_{H_2O}(T)}{\left(p_{total} - \emptyset_j \cdot p^s_{H_2O}(T)\right)} \cdot \frac{\dot{m}_j}{M_{w,j}} \tag{3.17}$$

where the subscript *j* refers to the dry carrier gas, i.e. either air (oxygen) or hydrogen.

In fuel cell context, the humidity of a gas is often given as the 'dew point temperature' which is defined as the temperature to which the gas should be cooled to reach saturation. Another term commonly used is the 'approach dew point temperature' which is defined as the difference between the temperature of the gas and its dew point temperature.

3.3.1.2 Water transport

The above mentioned factors (gas humidity and water generation) affect the water balance by changing the total amount of water inside a cell. Water transport does not directly do this, although it does indirectly. Instead, it changes the distribution of water inside a cell.

Water moves inside a cell because of different reasons. The most notable of these are: (1) electro-osmotic drag, (2) back diffusion, and (3) hydraulic permeation (Colinart et al. 2009). There is also some evidence of thermo-osmosis in which a temperature difference between the anode and the cathode causes water to move across the membrane (Zaffou, Kunz & Fenton 2006).

The *electro-osmotic drag* (EOD) is a result of protons flowing through the membrane, dragging water molecules from the anode to the cathode. The movement of water as a result of EOD is, therefore, always from the anode to the cathode. The magnitude of EOD is given as a coefficient, EOD coefficient, which is defined as the number of water molecules transported per one proton (Liu, Lu & Wang 2007). The EOD coefficient has been found to depend on the water content in the membrane, to the membrane external acid concentration, the temperature, and the phase (liquid or vapour) of water in the membrane (Ye, Wang 2007).

The build-up of water at the cathode as a result of the electrochemical reaction and electro-osmotic drag causes a water concentration gradient over the membrane. Diffusion tries to even out this gradient, and the process is called *back-diffusion* because the direction of water transport is the opposite compared to the one in the electro-osmotic drag (Mennola et al. 2004; Yan, Toghiani & Wu 2006).

Hydraulic permeation happens due to a pressure difference over the membrane. Normally the pressure difference between the anode and the cathode is kept as small as possible in order to maximize the membrane lifetime. Therefore, this form of water transport is usually unsubstantial (Yan, Toghiani & Wu 2006).

A commonly used coefficient to describe the water transport is the so called net water transport coefficient, α. It is defined as the ratio of the net transport of water from the anode to the cathode to the moles of protons transported from the anode to the cathode

$$\alpha = \frac{\dot{n}_{H_2O}^{net,a\rightarrow c}}{\dot{n}_{H^+}^{a\rightarrow c}} = \frac{\dot{n}_{H_2O}^{net,a\rightarrow c}}{\frac{1}{2}\dot{n}_{H_2O,gen}} = \frac{F}{I}\cdot \dot{n}_{H_2O}^{net,a\rightarrow c} = \frac{F}{I}\cdot \left(\dot{n}_{H_2O}^{in,a} - \dot{n}_{H_2O}^{out,a}\right) \tag{3.18}$$

(Mennola et al. 2004; Liu, Lu & Wang 2007; Lu, Liu & Wang 2007). The recent trend in MEA development is towards thinner membranes (Wang 2004). This has a major impact on water transport through the membrane, since the rate of back-diffusion is substantially increased. As the trend of decreasing membrane thickness continues, the rate of back-diffusion is likely to reach a level where external humidification is not needed at all. This not only completely changes the optimal stack design but is also a major advantage in terms of investment costs. However, thinner membranes also increase the rate of gas crossover which, as mentioned in section 2.1.2.3, causes a major voltage drop in PEMFCs. Thus, as the technical constraints for making even thinner membranes are overcome, the task is to optimize the thickness of the membrane.

3.3.1.3 Effects of temperature, pressure and flow rate on water balance

The effects of the operating temperature, the operating pressure, and the flow rate can be visualized by making an overall water balance in a PEMFC during operation at steady state. When it is assumed that the fuel cell works at such conditions that the net water transport through the membrane is zero, the partial pressure of water at the cell exhaust is

$$p_{H_2O,out} = \frac{\dot{n}_{H_2O,in}+\dot{n}_{H_2O,gen}}{\dot{n}_{H_2O,in}+\dot{n}_{H_2O,gen}+\dot{n}_{O_2,out}+\dot{n}_{inert}}\cdot p_{out} = \frac{2\cdot y_{O_2}+\lambda_{O_2}\cdot\Psi}{y_{O_2}+\lambda_{O_2}\cdot(\Psi+1)}\cdot p_{out} \tag{3.19}$$

where y_{O_2} is the mole fraction of oxygen in the air fed to the fuel cell, λ_{O_2} is the stoichiometric ratio of oxygen, and Ψ is

$$\Psi = \frac{p_{H_2O,in}}{p_{in}-p_{H_2O,in}}. \tag{3.20}$$

(Larminie, Dicks 2003)

Plotting equation (3.19) as a function of the operating temperature and the stoichiometric ratio of oxygen (1.5, 2, 3 and 6), we get the results shown in figures 3.3 (a) – (d) when the inlet conditions are varied as follows

(a) air fed at 1.2 bar and saturated at 15 °C
(b) air fed at 1.2 bar and saturated at 50 °C
(c) air fed at 1.2 bar and saturated at 75 °C
(d) air fed at 2.2 bar and saturated at 50 °C.

The pressure drop in the cell is 0.1 bar.

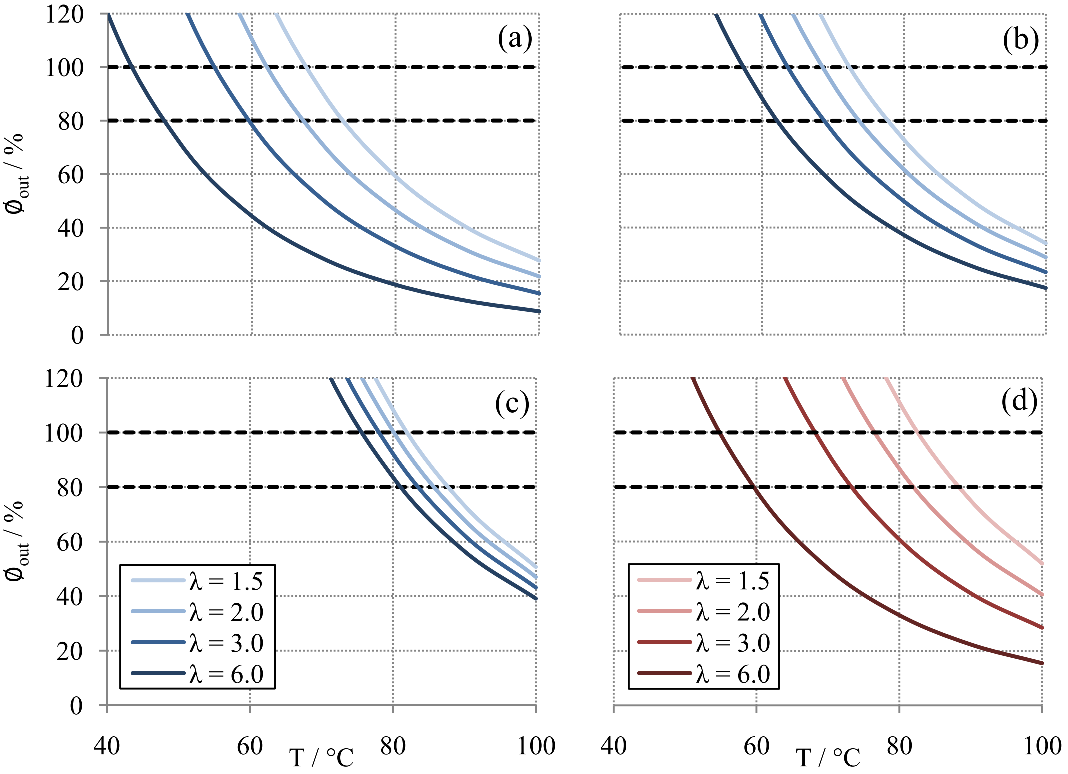

Figure 3.3. The effects of temperature, pressure, and flow rate on the humidity of air leaving the fuel cell.

From figures 3.3 (a), (b) and (c), it can be seen how the air inlet humidity affects the need of external humidification in different operating temperatures. From figure 3.3 (a), it can be concluded that when feeding ambient air to the fuel cell, there is a need for external humidification when the operating temperature is above 50 – 70 °C, depending on the air flow rate.

Comparing figures 3.3 (b) and (d) reveals the effect of the operating pressure: at low stoichiometric ratios of oxygen, the operating temperature can be increased when increasing the operating pressure without drying the cell out. However, the opposite is true when the air flow rate is high.

3.3.2 Effects of incorrect water balance

Water management in a PEMFC is challenging because of the narrow range of operating conditions leading to correct water balance. Moreover, it is challenging to maintain a correct water balance throughout the entire cell. In this section, the consequences of poor water management as well as mitigation strategies are introduced.

3.3.2.1 Dehydration

As already mentioned, the dehydration of the membrane translates into increased losses leading to decreased performance of the fuel cell. Besides decreasing the proton conductivity, low water content in the membrane also shrinks the pores in the membrane which in turn causes decreased back-diffusion and further dehydration of the anode side (Ji, Wei 2009). In an extreme case of dehydration, crazes might arise in the membrane. This enables gas crossover which on one hand results in membrane degradation through the formation hydrogen peroxide and radicals (Borup et al. 2007), and on the other hand enables thermal combustion of hydrogen (Ji, Wei 2009). Due to the thermal combustion of hydrogen, local hot spots are formed which might cause pinholes and increased gas crossover. Once this process is initiated, an accelerating destructive cycle is established (Ji, Wei 2009).

Dehydration can be mitigated by humidifying the reactant gases, by decreasing the flow rates of the reactants or by decreasing the operating temperature of the fuel cell. In addition, the development of thinner membranes, in which the rate of water transport is faster, alleviates the problem of membrane dehydration.

3.3.2.2 Flooding

Although water is required in PEMFC during operation, an excess of water causes decreased performance of the fuel cell by preventing reactant gases from reaching the catalyst. Indeed, flooding is a problem both for reactants flowing in the flow channels and for reactants diffusing in the GDL towards the catalyst.

Flooding of the flow channels occurs when the reactant flow rates are not high enough to remove the water. This occurs especially in fuel cell stacks where the reactant gases are supplied in parallel to the cells; when the flow channel of one cell floods, the excess gas simply flows through another cell. The flooding of the flow channels can be prevented by increasing the flow rate of reactants occasionally (purge) or by increasing the operating temperature. The increased operating temperature mitigates flow channel flooding because of the decreased surface tension and viscosity of water (Ji, Wei 2009).

Flooding of the cathode is more common than flooding of the anode because of the water formation on the cathode and the EOD phenomena. Nevertheless, the anode might flood due to poor water management, namely at low operating temperatures and at low reactant flow rates. The cathode, on the other hand, floods at high current densities when the generation of water and the EOD phenomena prevails over the back-diffusion of water (Ji, Wei 2009). Particularly, the cathode is prone to flood near the end of the cell where the air has reached saturated state and cannot remove any more water (Knights et al. 2004). The flooding of the cathode and the anode can be mitigated by increasing the operating temperature, resulting in a higher vapour pressure of water (Ji, Wei 2009).

3.3.3 Controlling the water balance – external humidification

The purpose of water management is to ensure a correct water balance throughout the cell – neither too dry nor too wet. This can be done, besides by controlling the operating conditions (temperature, pressure, and flow rates) as mentioned earlier in this section, also through other methods. These methods of water management can be categorized into either active methods or passive methods.

Passive methods do not consume energy and include special properties of the GDL (e.g. hydrophobicity) (Hussaini 2010) and of the electrolyte (e.g. thickness, morphology (Hussaini, Wang 2009), increased retention, and catalytic combustion of hydrogen (Larminie, Dicks 2003)). In addition, the use of a micro-porous layer between the GDL and the catalyst layer (CL) to facilitate effective wicking of liquid water from the cathode CL into the diffusion media is a passive method of water management (Barbir 2005).

Active methods of water management consume energy, but the benefits gained should outweigh the cost of energy. These methods include, in addition to controlling the operating conditions, mainly humidification of the membrane one way or another (Hussaini 2010). In this section, the methods of humidifying the membrane are introduced.

As was shown in section 3.3.1.3, at least some external humidification is needed at high operating temperatures. On the other hand, high operating temperature is desirable in order to increase the fuel cell performance. External humidifiers, however, take space and add cost to the fuel cell system. That is why the above mentioned alternatives to external humidifiers have recently gained a lot of interest. Nonetheless, external humidifiers are currently a natural choice for ensuring a proper water balance in a fuel cell, since similar equipment is used elsewhere as well (Larminie, Dicks 2003).

There are several ways to provide external humidification to a fuel cell: membrane humidifier (MH), enthalpy wheel humidifier (EWH), injection of water into the gas, 'interdigitated flow field'-design, bubbling gas through water, and connecting wicks to the electrolyte (Larminie, Dicks 2003; Park, Choe & Choi 2008). In the first two methods, moisture is transferred directly from a humid gas to a dry gas while the last four methods use liquid water to humidify the electrolyte or the gases entering the fuel cell. As the need of liquid water adds complexity, space, and cost of the system (Larminie, Dicks 2003), either a MH or a EWH is often preferred in real applications (Jung et al. 2007). Furthermore, in a MH and a EWH heat is also transferred, thus pre-heating the inlet gases (Jung et al. 2007).

In a MH the dry gas and the humid gas are separated with a polymer membrane which allows water to move across it (Jung et al. 2007). The advantage of a MH compared to a EWH is that the humidification is done passively, i.e. without the need of extra energy.

In a EWH the humid gas is passed over a water adsorbing material. Then the 'wheel' is rotated so that the dry gas becomes in contact with the adsorbing material and the water is desorbed. (Ahluwalia, Wang 2008b) By rotating a wheel with the adsorbant between fuel cell inlet and outlet gases, this method provides a means for continuous humidification. However, due to the rotating wheel, gas leakages are possible.

Direct injection of liquid water to the inlet gases is one of the simplest methods of humidification, it does not consume much energy, and it is easy to control (Jung et al. 2007). However, this method has the drawback of using liquid water, as mentioned above. Nevertheless, direct injection of liquid water can be advantageous when the inlet gas needs cooling, e.g. after being compressed (Larminie, Dicks 2003).

The use of 'interdigitated flow fields' is another method where liquid water is used. Only now, the water is fed directly into the fuel cell. In this method, the gas-water - mixture is flushed through the electrolyte by using pressurized gas feed and a special flow field design. (Wood, Yi & Nguyen 1998)

Humidification by bubbling is mostly used in laboratory test systems (Larminie, Dicks 2003). Here the humidity is controlled by controlling the temperature of the water bath.

Humidification by using wicks constructed into the electrolyte and dipped into liquid water keeps the electrolyte saturated with water. However, this method is not very widely used because of the problems with sealing the cell. (Larminie, Dicks 2003)

The choice of the humidification method depends greatly on the application at hand as well as on the operating conditions. However, the membrane humidifier and the enthalpy wheel are considered to be the most promising for mobile applications because of the simplified system (Park, Choe & Choi 2008). The enthalpy wheel tolerates higher temperatures than a membrane humidifier but has the problem of gas leakage. Moreover, in mobile applications, the passive operation of the membrane humidifier is a clear advantage over the enthalpy wheels active one.

3.4 Thermal management

The operating temperature of an unpressurized PEMFC is limited to below 100 °C because of the high water vapour pressure. This necessitates the use the expensive Pt catalyst but enables a quick start-up of the fuel cell as well as a wider range of materials in the fuel cell. In this section, the effects of the operating temperature on the performance and on the durability, the heat generation, as well as some practical aspects of realizing the cooling system are discussed.

3.4.1 Effects of temperature

The operating temperature affects cell performance through four different phenomena; increasing the temperature (1) decreases the EMF (Nernst equation), (2) increases the reaction rate and, thus, the exchange current density, (3) decreases the activation overpotential, and (4) increases the rate of mass transport. The net effect of increased temperature is increased performance of a fuel cell. However, in a PEMFC, the operating temperature also affects the water management and the durability of cell components.

Water and thermal management are inherently coupled, as the temperature inside the cell affects the water balance through the vapour pressure of water as well as through thermo-osmosis (Zaffou et al. 2006). Moreover, the latent heat of water plays a central role in the combined effects of water balance and temperature. The most critical challenges from the water management point of view are membrane dehydration and cathode flooding which dictate the operating temperature of a PEMFC (Kandlikar, Lu 2009).

From the fuel cell durability point of view, the temperature affects mainly the membrane and the catalyst. The membrane is especially sensitive to local hot spots which might dehydrate the membrane and cause leaks as discussed in section 3.3.2.1. The heat might also spread to neighbouring cells causing dehydration of the membrane and gas crossover. (Rodatz et al. 2004)

While the increased operating temperature is known to have a positive effect on the performance of the fuel cell, it has also been found to affect among other factors the rate of Pt particle sintering (Larminie, Dicks 2003). When catalyst particles sinter, they combine to form larger particles, thus reducing the active surface area. This results in an irreversible loss of catalytic activity.

3.4.2 Fuel cell efficiency and the sources of heat

Since the local temperature in a fuel cell has a profound impact on both the performance and the durability of the cell, it is worth considering the sources and the amount of the heat released during operation.

3.4.2.1 Efficiency and heat generation

The theoretical maximum amount of energy that can be gained from a reaction is the reaction enthalpy. Therefore, a commonly used definition of fuel cell efficiency is

$$\eta_{FC} = \frac{\Delta g(T)}{\Delta h_r(T)}. \tag{3.21}$$

Based on this and using equations (2.9) and (2.10), the theoretical maximum voltage of a hydrogen fuel cell can be written as follows

$$E_{theoretical} = -\frac{\Delta h_r(T)}{2 \cdot F}. \tag{3.22}$$

Hence, using equations (2.11), (3.21) and (3.22), the efficiency of the fuel cell can also be expressed as follows

$$\eta_{FC} = \frac{E}{E_{theoretical}}. \tag{3.23}$$

As discussed in section 2.1.1, the efficiency depends on whether the comparison is made against HHV or LHV of the fuel, i.e. whether the product water is in liquid or in vapour phase. While the efficiency calculated based on the LHV is more commonly used, it might lead to values greater than 100 % in CHP- (Combined heat and power) applications.

The power of a fuel cell is the current multiplied by the voltage as follows

$$P = I \cdot E. \tag{3.24}$$

Hence, the power lost as heat can be calculated as follows

$$\dot{Q} = P_{theoretical} - P = I \cdot (E_{theoretical} - E). \tag{3.25}$$

Because of the different losses occurring in a fuel cell, the operating voltage is a compromise between efficiency, current, and power and lies often somewhere between 0.6 and 0.7 V. Since $E_{theoretical,HHV} = 1.42\,V$ and $E_{theoretical,LHV} = 1.25\,V$ based reactions (2.1) and (2.2), respectively, it can be concluded that roughly half of the energy content of the fuel is lost as heat in a PEMFC using hydrogen as fuel. Hence, the amount of waste heat is remarkable, especially in large PEMFC systems, and has to be removed to avoid membrane dehydration (Faghri, Guo 2005).

3.4.2.2 Sources of heat

The sources of heat in a fuel cell include the voltage losses introduced in section 2.1.2.3 and the entropic losses. In figure 3.4, an example of a polarization curve (secondary axis) is depicted. Based on this polarization curve, the actual power, the heat losses at the cathode, and the heat losses at the anode (primary axis) are plotted as a function of current. It is assumed that the heat of entropic losses (Lampinen, Fomino 1993), the activation overpotential (Larminie, Dicks 2003), the gas crossover (Larminie, Dicks 2003; Koryta, Kavan 1987), and a major part of the heat from concentration overpotential (Faghri, Guo 2005) is released at the cathode. The heat of losses that are ohmic in nature is assumed to distribute evenly between the anode and the cathode.

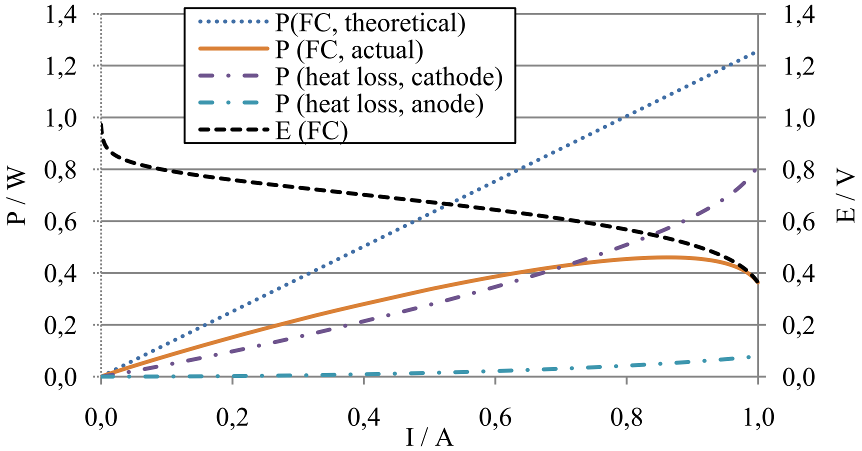

Figure 3.4. The power distribution in a PEMFC based on a theoretical polarization curve.

From figure 3.4, it can be concluded that majority of the heat is generated on the cathode side of the fuel cell. As the temperature gradients affect the water balance and high temperatures affect the membrane and catalyst durability, the major heat sources in a fuel cell should be taken into account when realizing the cooling.

3.4.3 Cooling system

The heat generated leaves the fuel cell naturally with the exhaust gases, by radiation, and by convection. In small fuel cell systems and in systems with open construction, the above mentioned phenomena can account for a large portion of heat removal. In large systems, air cooling is seldom sufficient to remove the large amount of heat generated. Thus, water cooling is often necessary.

In low temperature fuel cells, the removal of the waste heat is quite problematic because of the relatively small temperature difference between the fuel cell and the surroundings. Because of this, compared to ICEs, significantly larger and more efficient heat exchangers are needed (Ahluwalia, Wang 2008b; Kandlikar, Lu 2009). As a result, in automotive applications, the fuel cell stack size can actually be limited by radiator capacity (Knights et al. 2004). In working machine applications, where space is not necessarily an issue, the problem is not that critical because larger heat exchangers can be used.

Due to the large amount of heat to be removed, the coolant medium has to be supplied in parallel to the cells. However, even small deviations in flow resistance cause an uneven distribution of coolant between the cells. This problem can be mitigated by increasing the flow rate of the coolant medium, although at the expense of power consumption. In addition, by degassing the coolant circuit, air pockets can be avoided which when present can cause a remarkable flow resistance. (Rodatz et al. 2004)

Uniform operating conditions are naturally highly desirable throughout the fuel cell. Thus, the location of the coolant channels plays an important role in the thermal management. The misplacement of the coolant channels might cause temperature gradients inside the cell which in turn affect the uniformity of current density and, therefore, also the water balance (Kandlikar, Lu 2009; Knights et al. 2004).

4 Ejector model

Ejectors are an interesting option for recirculation pumps, as they do not consume any electricity but instead uses the pressure energy of the stored hydrogen to recirculate unconsumed hydrogen. However, the use of an ejector of fixed geometry in PEMFC applications is challenging because of frequent transients and wide ranges of operating conditions expected and because an ejector of fixed geometry works only at a relatively narrow range of flow rates (Ahluwalia, Wang 2008b). Nevertheless, there are some alternative methods to mitigate this problem, namely by changing the primary nozzle position (Aphornratana, Eames 1997), by controlling the anode back pressure (Karnik, Jing & Buckland 2006), by controlling the primary fluid pressure (He, Choe & Hong 2008; Karnik, Jing & Buckland 2006), by using a hybrid FDS consisting of an ejector and a pump (He, Choe & Hong 2008; Ahluwalia, Wang 2008b), and by using several ejectors in parallel.

Regardless of which of the aforementioned methods will be used, the control of the FDS is of crucial importance to avoid conditions that might damage the fuel cell. An example of control method is presented in the work of He et al. where the authors analyzed a hybrid FDS in which the ejector was passively controlled by controlling the hydrogen feed and the recirculation pump was actively controlled (He, Choe & Hong 2008). Another example is the work of Karnik et al. where the authors studied the control of ejector FDS based on two actuators namely anode back pressure valve and hydrogen feed valve (Karnik, Jing & Buckland 2006).

4.1 Model development

In PEMFC applications, a high humidity of the recirculated stream is desirable. Even though the highest performance of an ejector is achieved in critical mode (Munday, Bagster 1977), critical mode operation is not necessarily the most optimal option for PEMFC applications, since accelerating the fluid necessarily cools it down. Therefore, in this work, a model based on the work by Huang et al. (1999) is presented with some modifications making it more suitable for PEMFC applications. One of the modifications is the assumption of subcritical operation of the ejector which in practise means that the primary fluid is accelerated through a De Laval –nozzle to a sonic or supersonic velocity determined by the ratio of nozzle exit plane area to the nozzle throat area. This velocity together with the primary fluid stagnation pressure determines the pressure at the nozzle exit plane which is assumed to equal the mixing pressure. Another modification to the model presented by Huang et al. (1999) is that the recirculated gas is assumed to be saturated with water and the composition of the streams is taken into account when calculating the physical properties of them. In addition, the phase changes of water occurring in different parts of the ejector are included in the calculations.

4.1.1 Assumptions and general equations

The assumptions used are as follows (Huang et al. 1999):

1. The fluids behave like ideal gases.
2. The flow inside the ejector is steady and one-dimensional.
3. The flow inside the ejector is frictionless and adiabatic and, hence, isentropic.
4. The two fluids mix with a uniform pressure in a constant area mixing section.
5. The fluids enter and leave the ejector at zero velocity.

The ideal gas assumption is justified for both hydrogen and water vapour at normal conditions. However, by contrast to most gases, the Joule-Thompson inversion temperature of hydrogen is very low, only about 200 K at atmospheric pressure (Perry 1997). This means that when hydrogen undergoes isenthalpic expansion at room temperature, its temperature will rise. However, this is not taken into account in this model.

The assumption of isentropic flow is corrected for by using correction factors (efficiencies) for the flows in different parts of the ejector. A correction factor is also introduced to account for the irreversibility of the mixing process.

The validity of assumptions 4 and 5 is at least partly a matter ejector design. The assumption of zero velocity at ejector inlet and exhaust, however, is justified, as the effect of low velocity on temperature and pressure is unsubstantial.

From the ideal gas assumption it follows that

$$pV = nRT \tag{4.1}$$

and that the Mach-number can be expressed as follows

$$M = \frac{v}{c} = v\sqrt{\frac{M_w}{\kappa RT}} \tag{4.2}$$

where v is the velocity of the gas and c is the speed of sound in the gas (Perry 1997). Based on assumptions 1 – 3, the following isentropic flow relations for temperature, pressure, density and flow cross-sectional area can be used

$$T_0 = T\left(1 + \frac{\kappa - 1}{2} M^2\right) \tag{4.3}$$

where T_0 is the temperature of stagnated fluid, κ is the isentropic expansion factor, M is the Mach-number and T is the temperature of fluid accelerated to a velocity of M.

$$p_0 = p\left(1 + \frac{\kappa - 1}{2} M^2\right)^{\frac{\kappa}{\kappa - 1}} \tag{4.4}$$

where p_0 is the pressure of stagnated fluid and p is the pressure of fluid accelerated to a velocity of M.

$$\rho_0 = \rho\left(1 + \frac{\kappa - 1}{2} M^2\right)^{\frac{1}{\kappa - 1}} \tag{4.5}$$

where ρ_0 is the density of stagnated fluid and ρ is the density of fluid accelerated to a velocity of M.

$$\frac{A_1}{A_2} = \frac{M_2}{M_1}\sqrt{\frac{\left[\left(\frac{2}{\kappa_1+1}\right)\left(1+\frac{(\kappa_1-1)}{2}{M_1}^2\right)\right]^{\frac{\kappa_1+1}{\kappa_1-1}}}{\left[\left(\frac{2}{\kappa_2+1}\right)\left(1+\frac{(\kappa_2-1)}{2}{M_2}^2\right)\right]^{\frac{\kappa_2+1}{\kappa_2-1}}}} \tag{4.6}$$

where A_j is the cross-sectional area of the fluid flowing at a velocity of M_j. (Perry 1997; Kutz 2009)

Mass, momentum, and energy conservation equations are

$$\sum_j \left(\rho_j A_j v_j\right)_{in} = \sum_j \left(\rho_j A_j v_j\right)_{out}, \tag{4.7}$$

$$\sum_j \left(\dot{m}_j v_j\right)_{in} = \sum_j \left(\dot{m}_j v_j\right)_{out}, \tag{4.8}$$

$$\sum_j \dot{m}_j \left(h_{w,j}(T) + \frac{1}{2}{v_j}^2\right)_{in} = \sum_j \dot{m}_j \left(h_{w,j}(T) + \frac{1}{2}{v_j}^2\right)_{out} \tag{4.9}$$

where $h_w = \bar{c}_p\left(T - T_{ref}\right)$ is the specific enthalpy of fluid and $\bar{c}_p$ is the isobaric specific heat capacity calculated in the mean temperature. The momentum conservation equation (4.8) is based on the assumption of constant area and constant pressure mixing, and the energy conservation equation (4.9) is based on the assumption of an adiabatic system.

Friction losses and other irreversibility's are accounted for by using efficiency coefficients in the primary nozzle, in the suction chamber, in the mixing section, and in the diffuser as follows

$$M_{real} = \eta \cdot M_{ideal}. \tag{4.10}$$

In the primary nozzle, in the suction chamber, and in the diffuser, the friction losses are reflected on the pressure, i.e. when calculating the pressure, M_{ideal} is used. However, the temperature and the density are not affected by friction losses, i.e. they are calculated using the real velocity.

4.1.2 Model formulation

Figure 4.1 shows a schematic diagram of an ejector.

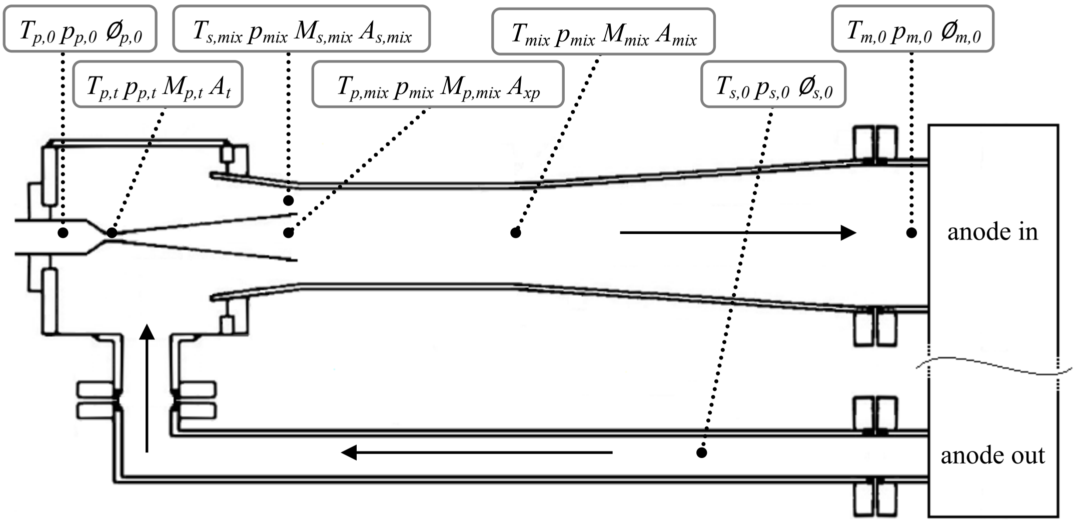

Figure 4.1. Schematic diagram of an ejector (figure modified) (McKetta 1983).

The primary fluid is accelerated from a given stagnation state, $p_{p,0}$ and $T_{p,0}$, to sonic velocity in the converging part of the nozzle. By using equations (4.3), (4.4), and (4.10), the temperature and pressure at the nozzle throat can be solved, respectively, as follows

$$T_{p,t} = T_{p,0}\frac{2}{\kappa-1}, \tag{4.11}$$

$$p_{p,t} = p_{p,0}\left(1+\frac{\kappa-1}{2\cdot\eta_p{}^2}\right)^{\frac{\kappa}{1-\kappa}}. \tag{4.12}$$

Using the temperature and pressure at the nozzle throat calculated above, the mass flow rate through the nozzle throat of given area can be calculated using equations (4.1), (4.2), (4.5), and (4.7) as follows

$$\dot{m}_p = A_t\cdot\frac{p_{p,0}}{T_{p,0}}\left(\frac{\kappa+1}{2}\right)^{\frac{1}{(1-\kappa)}}\sqrt{\frac{\kappa\cdot M_w\cdot T_{p,t}}{R}}. \tag{4.13}$$

In the diverging part of the nozzle, the primary fluid is accelerated further to a velocity determined by the nozzle exit plane area. Using equation (4.6), this velocity can be calculated iteratively as follows when the velocity at nozzle throat is unity

$$M_{p,xp} = \frac{A_t}{A_{xp}}\left[\left(\frac{2}{\kappa+1}\right)\left(1+\frac{(\kappa-1)}{2}M_{p,xp}{}^2\right)\right]^{\frac{\kappa+1}{2(\kappa-1)}}. \tag{4.14}$$

This is the velocity that the primary fluid is assumed to have at the beginning of the mixing section, $M_{p,mix} = M_{p,xp}$. By using equations (4.3) and (4.4), the temperature and pressure of the primary fluid at the beginning of the mixing section can be calculated, respectively, as follows

$$T_{p,mix} = T_{p,0}\left(1+\frac{\kappa-1}{2}M_{p,mix}{}^2\right)^{-1}, \tag{4.15}$$

$$p_{p,mix} = p_{p,0}\left(1+\frac{\kappa-1}{2}\left(\frac{M_{p,mix}}{\eta_p}\right)^2\right)^{\frac{\kappa}{1-\kappa}}. \tag{4.16}$$

The pressure in the mixing section is taken to be the pressure of primary fluid at the beginning of mixing section, $p_{mix} = p_{p,mix}$.

The secondary fluid is accelerated from a stagnation state, $p_{s,0}$ and $T_{s,0}$, to the mixing pressure calculated in equation (4.16). The velocity of the secondary fluid at the beginning of the mixing section can be calculated using equations (4.4) and (4.10) as follows

$$M_{s,mix} = \eta_s\sqrt{\left[\left(\frac{p_{s,0}}{p_{mix}}\right)^{\frac{\kappa-1}{\kappa}}-1\right]\frac{2}{\kappa-1}}, \tag{4.17}$$

and the temperature can be calculated using equation (4.3) as follows

$$T_{s,mix} = \frac{T_{s,0}}{\left(1+\frac{\kappa-1}{2}\cdot M_{s,mix}{}^2\right)}. \tag{4.18}$$

The area of secondary fluid at the beginning of the mixing section is

$$A_{s,mix} = A_{mix} - A_{xp}. \tag{4.19}$$

Using this area and the mass balance, the mass flow rate of secondary fluid entering the mixing section can be solved as follows

$$\dot{m}_s = A_{s,mix} \cdot p_{s,0} \cdot M_{s,mix} \left(1 + \frac{\kappa-1}{2} {M_{s,mix}}^2\right)^{\frac{1+\kappa}{2(1-\kappa)}} \sqrt{\frac{\kappa \cdot M_w}{R \cdot T_{s,0}}}. \tag{4.20}$$

In the mixing section the two fluids mix totally, i.e. at the end of mixing section the fluid properties as well as the velocities are uniform. During mixing, there is momentum exchange and energy exchange between the two fluids. The mixed fluid velocity (v_m) and temperature (T_{mix}) can be calculated from the momentum balance and the energy balance, respectively, as follows

$$\dot{m}_p v_{p,mix} + \dot{m}_s v_{s,mix} = \eta_m \dot{m}_m v_m, \tag{4.21}$$

$$\dot{m}_p \left(\bar{c}_{p,p}\left(T_{p,mix} - T_{ref}\right) + \frac{1}{2} {v_{p,mix}}^2\right) + \dot{m}_s \left(\bar{c}_{p,s}\left(T_{s,mix} - T_{ref}\right) + \frac{1}{2} {v_{s,mix}}^2\right) +$$

$$\ldots \frac{\dot{m}_{H_2O,condensed}}{M_{w,H_2O}} \cdot h_l\left(T_{ref}\right) = \dot{m}_m \left(\bar{c}_{p,m}\left(T_m - T_{ref}\right) + \frac{1}{2} {v_m}^2\right) \tag{4.22}$$

where h_l is the latent heat of water and $\bar{c}_p$ is the isobaric specific heat capacity at the mean temperature.

In the diffuser, the mixture is decelerated to zero velocity. The resulting pressure can be calculated equations (4.4) and (4.10) as follows

$$p_{m,0} = p_{mix} \left(1 + \frac{\kappa-1}{2} (M_m \cdot \eta_d)^2\right)^{\frac{\kappa}{\kappa-1}}. \tag{4.23}$$

The deceleration of the fluid to stagnation results in a temperature increase. This in turn affects the vapour pressure of water which results in evaporation of the condensed water. Hence, the resulting stagnation temperature is

$$T_{m,0} = T_m \left(1 + \frac{\kappa-1}{2} {M_m}^2\right) - \frac{h_l \cdot M_w}{\dot{m}_{tot} \cdot \bar{c}_p} \tag{4.24}$$

where $\dot{m}_{tot}$ is the total mass flow rate of gas and liquid water entering the stack. The flow resistance of the fuel cell is a function of the mass flow rate

$$\Delta p_{FC} = f\left(\dot{m}_p + \dot{m}_s\right) \tag{4.25}$$

and is used for calculating the secondary fluid stagnation pressure as follows

$$p_{s,0} = p_{m,0} - \Delta p_{FC}. \tag{4.26}$$

4.1.3 Solving the model

The model is solved iteratively as shown in figure 4.2. The green boxes represent explicit states of the fluid, i.e. states where the temperature, pressure and velocity are solved.

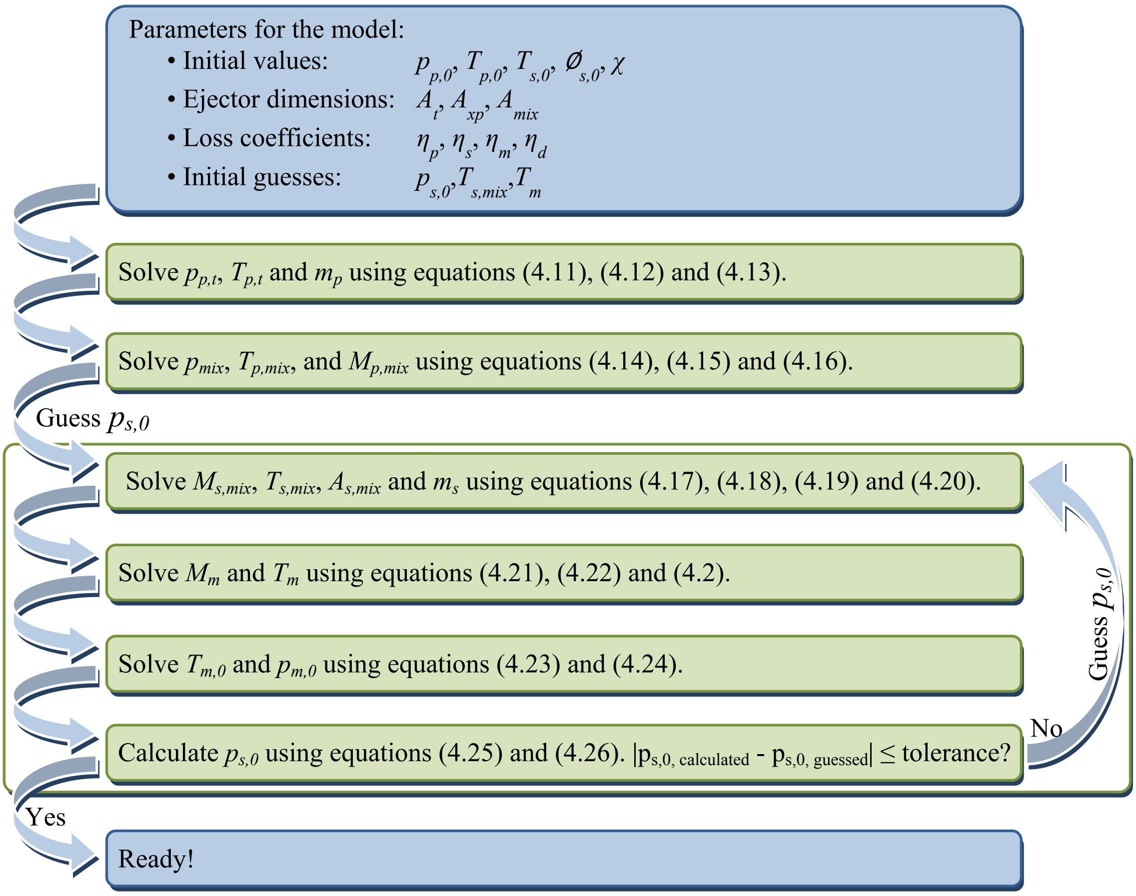

Figure 4.2. Model solving chart.

The model has to be solved iteratively because the value of the secondary fluid stagnation pressure is used in equation (4.17) before it is solved in equation (4.26). Additionally, at most of the explicit states shown in figure 4.2, the temperature, the pressure, and the velocity have to be solved iteratively because the physical properties of the streams depend on temperature and pressure which depend on the velocity which in turn cannot be solved without knowing the physical properties of the stream.

The model is implemented in Matlab® and solved using Matlab’s ‘fminsearch’ function. The physical properties (isochoric and isobaric heat capacities) of water and steam are calculated using XSteam, a ready-built toolbox for Matlab®. XSteam is based on the "International Association for Properties of Water and Steam Industrial

Formulation 1997" (Holmgren 2005). Isochoric and isobaric heat capacities for hydrogen are calculated from curve fits on data from (Roder, McCarty & Hall 1972).

4.2 Simulations

In PEMFC applications, high recirculation rate of the anode outlet gas is desirable mainly for two reasons, namely to achieve a high stoichiometric ratio of hydrogen and to achieve a high anode inlet humidity. The high stoichiometric ratio of hydrogen enables fast response during transient conditions and allows a lower hydrogen concentration in the anode loop. The allowed lower hydrogen concentration translates into the possibility of using lower quality and cheaper hydrogen as fuel as well as into a better hydrogen economy, as the purged gas contains less hydrogen. The recirculated humidity, on the other hand, makes external humidification on the anode side unnecessary, thus simplifying the system. Recirculation, however, consumes energy except when using an ejector.

The recirculation rate achieved with an ejector depends, besides on the ejector dimension, mainly on two parameters namely the hydrogen feed pressure and the flow resistance of the recirculation loop. While pressurizing hydrogen necessarily consumes energy, the flow resistance of the stack can be decreased by optimizing the gas flow channel structure. Therefore, in this work, the ejector model is simulated to study the benefits gained with decreasing the flow resistance of the stack. In addition, the effects of ejector dimensions on the ejector performance are studied. The simulations are carried out using parameters shown in table 4.1.

Table 4.1. Parameters common to all simulations.

Parameter	Value
Primary fluid	
Temperature, $T_{p,0}$	293 K
Relative humidity, $\varnothing_{p,0}$	0 % [5]
Secondary fluid	
Temperature, $T_{s,0}$	333 K
Relative humidity, $\varnothing_{s,0}$	100 %
Efficiency coefficients	
Primary flow, η_p	0.88 [6]
Secondary flow, η_s	0.88
Mixing, η_m	0.80 [6]
Diffuser, η_d	0.88
Stack flow resistance	
Pressure drop, Δp (for P8 stack)	$\Delta p = \chi \cdot 150$ bar (kg s^{-1})$^{-1}$ + $6 \cdot 10^{-3}$ bar [7]

The pressure drop shown in table 4.1 is a function of the mass flow rate entering the stack. This function is based on the pressure drop measured on the 8-kW$_e$ stack used in this work.

4.2.1 Effects of stack flow resistance

The effect of stack flow resistance on stack inlet stoichiometry of hydrogen is studied by simulating the model with four different ejectors and by varying the flow resistance coefficient as well as the hydrogen feed pressure. The dimensions of ejectors are shown in table 4.2 and the varied parameters are shown in table 4.3.

Table 4.2. Dimensions of ejectors used in the study of the effects of stack flow resistance.

Ejector	A_t / mm^2	A_{xp} / mm^2	A_{mix} / mm^2
E_1	0.3	0.34	10
E_2	0.3	0.3	10
E_3	0.3	0.34	50
E_4	0.3	0.3	50

---

[5] The humidity of fresh hydrogen is not considered in the implementation of the model

[6] (Huang et al. 1999)

[7] χ is the flow resistance coefficient

Table 4.3. Parameters used in simulations where the effect stack flow resistance is investigated.

Parameter	Value
Primary fluid Pressure, $p_{p,0}$	1...10 bar
Stack flow resistance Flow resistance coefficient	$\chi = 0.2 ... 2$

4.2.2 Effects of ejector dimensions

The effects of ejector dimensions are studied by solving the model for variable ejector dimensions but with some constraints. This way the optimal ejector dimensions can be determined for certain operating conditions. The ejector dimension ranges as well as other parameters used in the simulation are shown in table 4.4. The constraints are shown in table 4.5.

Table 4.4. Parameters used in simulations where the effect ejector dimensions is investigated.

Parameter	Value
Primary fluid Pressure, $p_{p,0}$	Solved
Ejector dimensions Nozzle throat area, A_t Nozzle exit plane area, A_{xp} Mixing section area, A_{mix}	 Solved $1 ... 2 \cdot A_t$ 2 ... 68 mm^2
Stack flow resistance Flow resistance coefficient	$\chi = 1$

Table 4.5. Constraints used when solving the model in investigating the effect of ejector dimensions.

Variable	Constraint
m_p	determined by the current load of 64 cell stack
I	60 A, 200 A [8]
$p_{m,0}$	1.3 bar

---

[8] The idea is to simulate the hydrogen consumption of 64 cell stack operating at maximum amperage (200 A) and at 30 % of maximum amperage (60 A).

5 Experimental

In the experimental part of this work, the build-up of nitrogen in the anode recirculated stream is studied. The rate of nitrogen build-up is measured by varying the current load and the rate of nitrogen feed. The effect of nitrogen build-up on cell voltages is also studied. The experiments are conducted on a PEMFC system assembled around an 8-kW_e fuel cell stack. Prior to the nitrogen build-up experiments, the newly assembled fuel cell system is tested by conducting steady state experiments.

5.1 Testing equipment and experimental setup

The fuel cell stack used in the experiments is a NedStack P8.0-64 PEM fuel cell stack with a maximum power of more than 8 kW_e, a maximum current of more than 250 A, and an OCV of 64 V. The fuel cell stack operates at atmospheric pressure and at a temperature of approximately 65 °C.
The assembled fuel cell system consists of, in addition to the fuel cell stack, three subsystems namely the fuel supply, the air supply, and the cooling. The entire fuel cell system is depicted in figure 5.1.

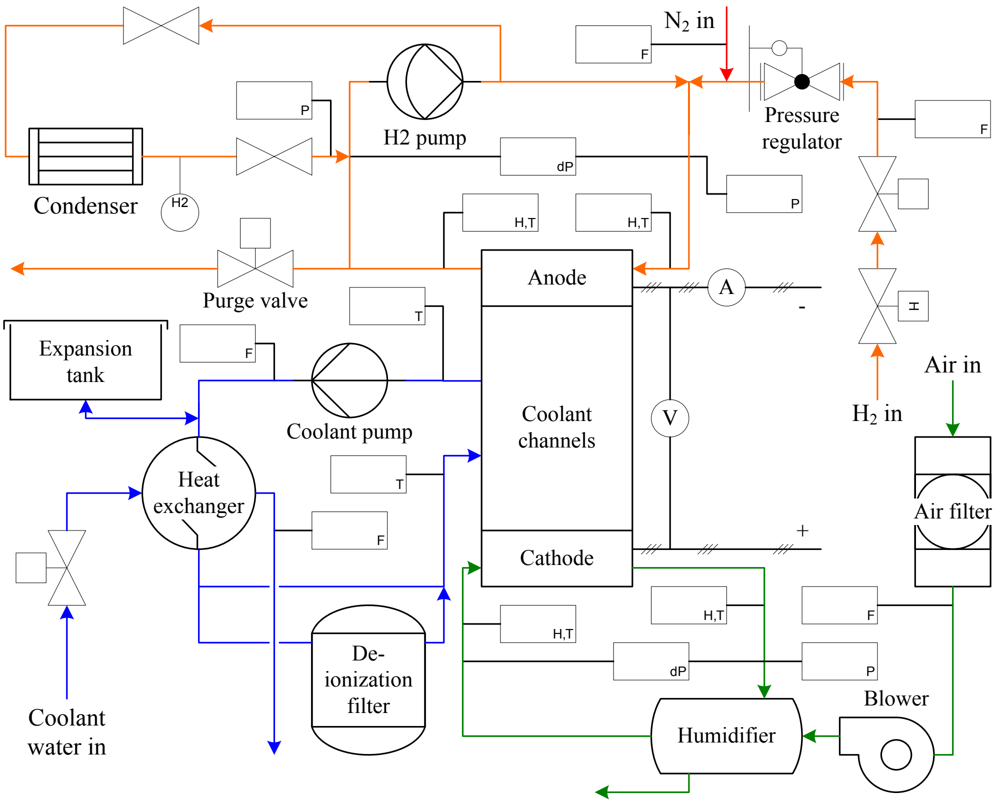

Figure 5.1. The fuel cell system used in the experiments.

The hydrogen used as fuel is fed passively through a pressure regulator (RHPS, LRS4) in order to reduce the pressure from the storage and to keep the pressure on the anode side as constant as possible. The hydrogen feed rate is measured continuously using a mass flow meter (Bronkhorst High-Tech B.V., EL-FLOW F-112AC).

The unconsumed hydrogen leaving the stack is recirculated to the anode inlet using a diaphragm pump (Rietschle-Thomas, 118ZC) which is controlled manually by adjusting the control voltage. Because of the hydrogen recirculation, no humidifier is needed to humidify the hydrogen entering the fuel cell stack but the recirculated moist hydrogen suffices.

As a result of the closed hydrogen loop and the recirculation, impurities enrich in the hydrogen stream. To remove these impurities, the purge valve (Sirai, D132V20) is opened periodically for a short period of time or when the voltage of at least one cell drops below a certain limit. During the purge, the hydrogen flow rate increases, thus flushing water droplets and slugs from the flow channels in the stack. After every hydrogen purge, the air blower is run at full speed for a moment to remove the water droplets and slugs from the cathode side flow channels as well.

The effect of inert build-up is investigated by feeding nitrogen through a mass flow controller (MKS Instruments, Mass flo 1179A00813C) into the anode loop. The concentration of hydrogen in the anode loop is measured using a hydrogen sensor (H2scan, HY-OPTIMA 740) through which a dried sample stream is passed. The drying of the sample stream is realized by cooling it in an ice bath.

The air used as the oxidant is fed to the fuel cell stack using a blower (Domel, d.d., 497.3.265-852). The flow speed of air is automatically controlled by the control system. Before passing the blower, the air is filtered (Donaldson, FCX400045) and its flow rate is measured (TSI Incorporated, 42350101).

Unlike the hydrogen, the air is not recirculated. Consequently, external humidification is required on the cathode side. The dry air entering the system flows through a membrane humidifier (PermaPure, FC300-1660-10HP) where it is humidified by the moist air leaving the stack.

Heat is removed from the fuel cell stack by recirculating de-ionized coolant water in a closed loop between the stack and a liquid-liquid heat exchanger (SWEP, B5Hx20/1P-SC-S). The stack temperature is automatically controlled by opening and closing the water supply to the cold side of the heat exchanger. The coolant water in the closed loop is pumped (Johnson Pump, CM30P7-1) at constant speed and its flow rate is measured (Bürkert, 8012).

A de-ionization filter (Domnick Hunter Technologies Ltd./Pentek) is used to remove impurities dissolved from the coolant loop, mainly from the fuel cell stack. The maximum flow rate through the de-ionization filter is lower than the flow rate of coolant water used in this work, so a major part of the coolant water is by-passed. This keeps the temperature of the de-ionization filter within acceptable limits.

The temperature is measured at the inlet and at the outlet of the fuel cell stack in all three subsystems. In the cooling subsystem, the temperature is measured using thermistors (Tempatron, NTC 10 kΩ) whereas the temperature in the fuel supply and air supply subsystems are measured together with the humidities (Vaisala, Humidity and temperature transmitter HMT337). Moreover, in the fuel supply and air supply subsystems, the pressure at the stack inlet (Sensor Technics, CTEM 70350 GY4) and the pressure difference between stack inlet and outlet (Omega, PX2300) are measured. Cell voltages are measured using a CVM (Vito). All pieces of equipment and instruments are listed in tables 5.1 and 5.2, respectively.

Table 5.1. List of equipment.

Piece of equipment	Manufacturer	Model
Air filter	Donaldson	FCX400045 [9]
Air blower	Domel, d.d.	497.3.265-852/223602
Membrane humidifier	PermaPure	FC300-1660-10HP
H_2 recirculation pump	Rietschle-Thomas	118ZC (55lpm version)
Pressure regulator	RHPS	LRS4
Purge valve	Sirai	D132V20
Coolant pump	SPX Johnson Pump	CM30P7-1
De-ionization filter	domnick hunter technologies Ltd. / Pentek (cartridge)	10" cartridge
Heat exchanger	SWEP	B5Hx20/1P-SC-S

---

[9] Manufacturing discontinued.

Table 5.2. List of instruments.

Instrument	Manufacturer	Model
Differential pressure sensor	Omega	PX2300
Humidity and temperature transmitter	Vaisala	HMT337
Thermistor	Tempatron	NTC 10 kΩ
Air flow meter	TSI Incorporated	42350101[10]
Coolant flow meter	Bürkert	8012
H_2 mass flow meter	Bronkhorst High-Tech B.V.	EL-FLOW F-112AC
Pressure sensor	Sensor Technics	CTEM 70350 GY4
N_2 mass flow controller	MKS instruments	Mass flo 1179A00813C
H_2 sensor	H2scan	HY-OPTIMA 740

For recording the measurements, two systems are used. FieldPoint (National Instruments) and LabView are used for recording the load current, the anode and the cathode pressures, the anode pressure difference, the hydrogen flow rate, as well as the temperature and humidity of gases in air and fuel supply systems. The rest of the measurements are recorded using an in-house-built measurement and control system based on an embedded Ethernet board (eginte Gmbh., Ethernut 2). This system is also used for controlling the FCS. The complete fuel cell system assembled in a fume hood is shown in figure 5.2.

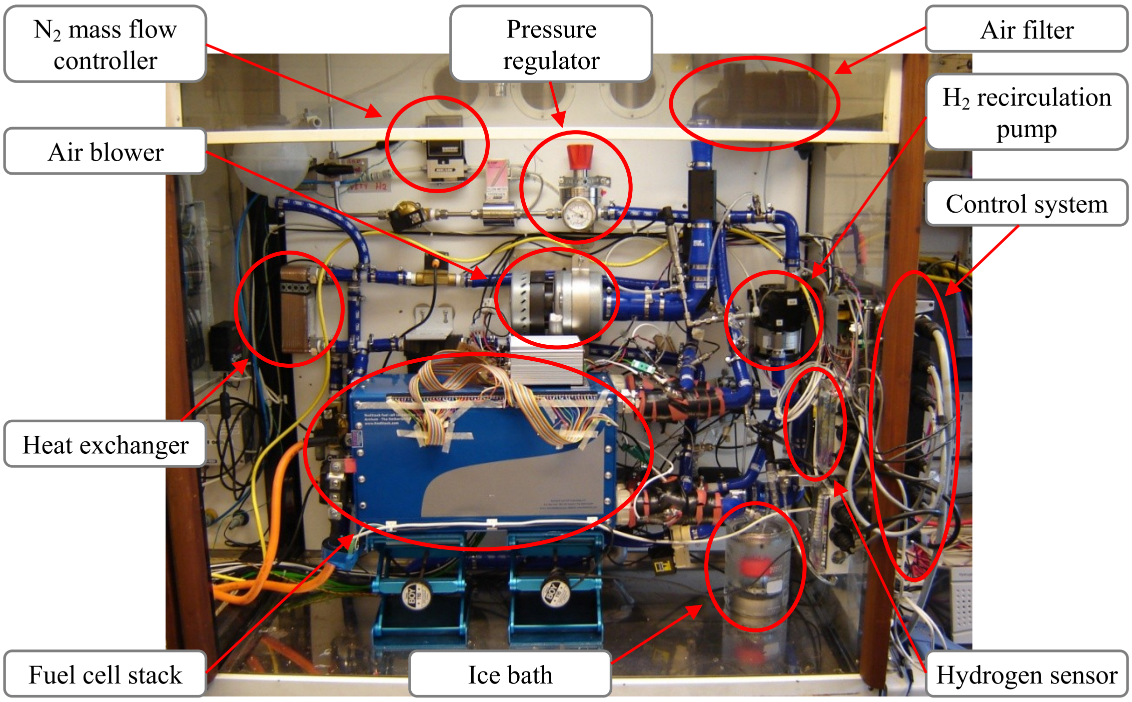

Figure 5.2. A picture of the system assembled in a fume hood.

---

[10] Manufacturing discontinued

5.2 Measurements

The primary goal of the experimental part of this work is investigate the inert build-up in the recirculated anode exhaust stream. These measurements are presented in section 5.2.3. Prior to the inert build-up measurements, the function of the newly assembled PEM fuel cell system was verified. The method of system initial testing is presented in section 5.2.2. Besides testing the complete system, the function of some instruments is also verified and corrections are made to the signal processing if necessary. These calibrations measurements are presented in section 5.2.1.

5.2.1 Calibration measurements

5.2.1.1 Calibration of the pressure sensors

The readings of the pressure sensors as well as the differential pressure sensors used for measuring the anode and the cathode pressures and pressure differences, respectively, are measured using a U-column. The setup is shown in figure 5.3.

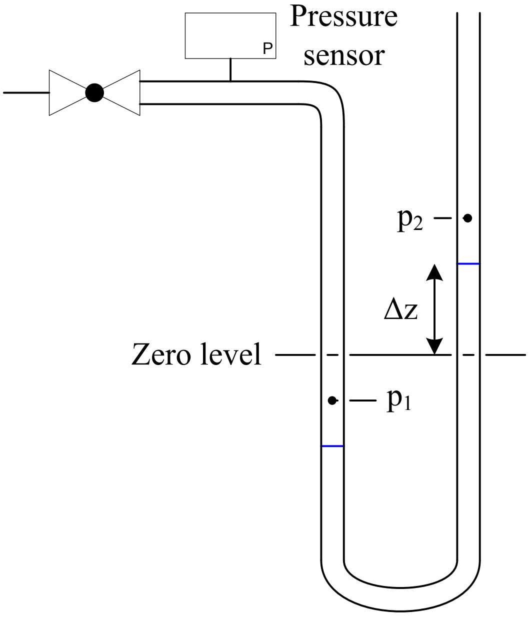

Figure 5.3. Experimental setup of the calibration of the pressure sensors and the differential pressure sensors.

With reference to figure 5.3, the measurements are carried out by pressurizing the left side of the U-column progressively, measuring Δz, and recording the sensor response. Prior to measuring the Δz and recording the sensor response, the system is let to stabilize for a moment.

The pressure difference $p_1 - p_2$ is calculated as follows

$$p_1 - p_2 = 2\rho g \Delta z \tag{5.1}$$

where g is the gravitational acceleration. While the pressure sensors are calibrated to measure overpressure with the zero level in atmospheric pressure, i.e. $p_2 = 0$, the differential pressure sensors measure the difference $p_1 - p_2$ with p_2 in atmospheric pressure in this experiment.

5.2.1.2 Calibration of the mass flow controllers

The flow rate as a function of the control signal is verified of two mass flow controllers, namely an air mass flow controller and a hydrogen mass flow controller, using a flow calibrator. The setup is shown in figure 5.4.

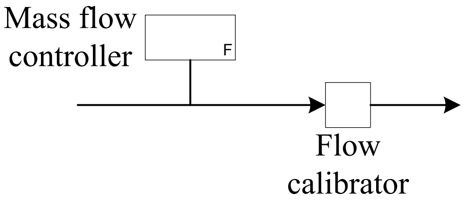

Figure 5.4. Experimental setup of the calibration of the mass flow controllers.

The air mass flow controller (MKS Instruments, Mass flo 1179A00813C) is calibrated with flow rates ranging from 0.1 dm^3/min to 1 dm^3/min using nitrogen, and the hydrogen mass flow controller (MKS Instruments, Mass flo 1179A00732C) is calibrated with flow rates ranging from 0.1 dm^3/min to 0.3 dm^3/min using hydrogen. For each control value, five readings of the flow calibrator are taken and an average of these is used. The flow calibrator used is a Gilian Gilibrator-2 (Sensidyne inc).

5.2.1.3 Determining the anode side volume

The anode side volume of the fuel cell system is needed for calculation of inert build-up rates. Hence, the volume of the anode side is determined. This is done by feeding nitrogen (MKS Instruments, Mass flo 1179A00813C) with constant rate to the closed anode loop (purge valve closed) and measuring the pressure increase. Using the ideal gas law, the volume of the anode loop can be calculated as follows

$$V_{anode} = \frac{\dot{n} \cdot \Delta t}{\Delta p} RT \tag{5.2}$$

where $\dot{n}$ is the feed rate of nitrogen and Δp is the pressure increase during the time interval Δt. Additionally, $\frac{\Delta t}{\Delta p}$ is the inverse of the slope of the pressure as a function of time when there are no leakages in the system.

5.2.1.4 Calibration of the H_2 sensor

The function of the hydrogen sensor is verified by feeding both hydrogen and nitrogen into a closed loop and measuring the hydrogen sensor reading. The setup is shown in figure 5.5.

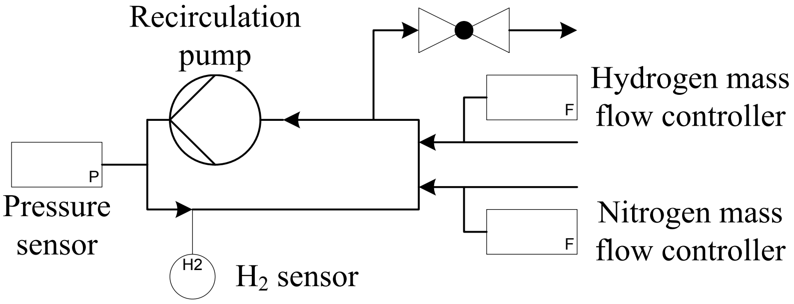

Figure 5.5. Experimental setup of the hydrogen sensor verification measurements.

The measurements are conducted by feeding nitrogen and hydrogen simultaneously into the closed loop, keeping the recirculation pump running, and periodically purging the loop. This is done until the reading of the H_2 sensor stabilized. At this point the mole fraction of hydrogen in the loop can be calculated from the ratio of the hydrogen feed rate to the nitrogen feed rate. Next, the composition inside the loop is changed gradually by alternately feeding nitrogen and keeping the pump running for a moment to even out concentration gradients. The pressure inside the loop is increased gradually up to about 300 mbar(g) after which the experiment is repeated with a different initial gas composition.

5.2.1.5 Measuring the flow resistance of the H_2 sensor loop

During operation of the assembled fuel cell system, the flow rate through the H_2 sensor loop is determined by the H_2 sensor loop flow resistance and the pressure difference between loop inlet and outlet, i.e. pressure drop over the stack. Therefore, the flow resistance of the hydrogen sensor loop is measured. The setup is shown in figure 5.6.

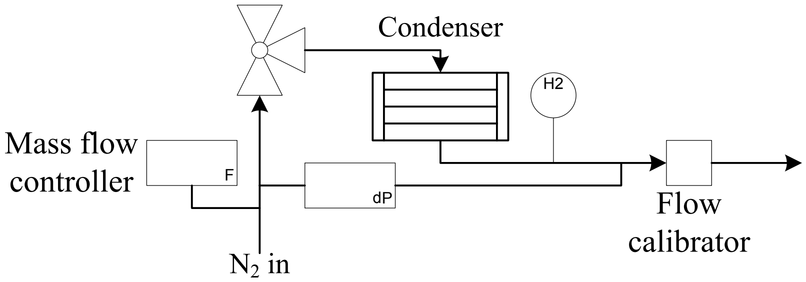

Figure 5.6. Experimental setup of hydrogen sensor loop pressure drop measurements.

The measurements are carried out by feeding nitrogen through a mass flow controller. As the mass flow controller (El-Flow Select F-201C, Bronkhorst High-Tech B.V.) used in this experiment is not calibrated, a flow calibrator (Gilian Gilibrator-2, Sensidyne inc.) is used to measure the flow rate.

The flow of nitrogen can be assumed to be incompressible, since the pressure differences are relatively small in this experiment. When no shaft work is done, there is no elevation, and the difference in kinetic energies of the flow at the boundaries is negligible, the mechanical energy balance for the flow through the hydrogen sensor loop can be written as follows

$$\Delta p + \rho \cdot \left(\xi \frac{L}{D} + \sum_j \zeta_j\right) \cdot \bar{v}^2 = 0 \qquad (5.3)$$

where Δp is the pressure difference, ρ is the density of the gas, L is the length of the pipe, D is the diameter of the pipe, $\bar{v}$ is the average velocity of the fluid, and $\sum \zeta_j$ is the sum of local flow resistances (Aittamaa 2006). ξ is the friction loss coefficient which for laminar flow (Re < 2100) is

$$\xi = \frac{64}{Re} \qquad (5.4)$$

and for turbulent flow (Re > 3000) can be solved using Colebrook's equation

$$\frac{1}{\sqrt{\xi}} = -2.0 \cdot log\left(\frac{k}{3.7065 \cdot d} + \frac{2.5226}{Re\sqrt{\xi}}\right) \qquad (5.5)$$

where k is the absolute roughness of the pipe and d is the nominal diameter of the pipe (Keskinen 1989).

The hydrogen sensor loop consists of pipes in varying diameters. When considering separately the laminar flow section and the turbulent flow section, equation (5.3) can be rewritten as follows

$$\Delta p + \left[\rho \cdot \left(\xi \frac{L}{D} + \sum \zeta_j\right) \cdot \bar{w}^2\right]_t + \left[\rho \cdot \left(\xi \frac{L}{D} + \sum \zeta_j\right) \cdot \bar{w}^2\right]_l = 0 \qquad (5.6)$$

where the subscripts t and l refer to turbulent flow section and laminar flow section, respectively. By using the definition of Reynolds number

$$Re = \frac{\bar{v}D\rho}{\mu} \tag{5.7}$$

where μ is the viscosity of the fluid and equation (5.4), equation (5.6) can be written as follows

$$\Delta p + \rho \cdot \frac{4}{\pi} \cdot \left[\xi(Re)\frac{L_t}{\bar{D}_t^{\,3}} + \frac{\sum \zeta_{j,t}}{\bar{D}_t^{\,2}} + \frac{\sum \zeta_{j,l}}{\bar{D}_l^{\,2}}\right] \cdot \dot{V}^2 + \mu\frac{64L_l}{\bar{D}_l^{\,2}} \cdot \dot{V} = 0 \tag{5.8}$$

where $\dot{V}$ is the volume flow rate.

5.2.2 Initial testing of the system

The initial testing of the system is done by carrying out steady state measurements with variable current loads, hydrogen recirculation rates, and anode pressures. In these measurements, the loop containing the hydrogen sensor, seen in figure 5.1, is not connected. The conditions used in the measurements are shown in table 5.3.

Table 5.3. The conditions used when testing the system.

Parameter	Control
H_2 recirculation pump control voltage	0%, 33%, 67%, 100%
Anode set point pressure	~100 mbar(g), ~300 mbar(g)
Current load	120 A, 160 A
Purge interval	90 s
Anode purge length	0.5 s
Inert feed	none

5.2.3 Inert build-up measurements

Two sets of inert build-up measurements are conducted. First, the inert build-up rate is measured by varying the purity of the fuel, and second, the effect of inert concentration on the performance of fuel cell stack is investigated by using cell voltage triggered purge.

5.2.3.1 Inert build up rate measurements

The rate of inert build-up is investigated by using four different feed hydrogen purities, one with laboratory quality hydrogen and three hydrogen qualities where the purity is changed by feeding nitrogen into the anode loop. The conditions used in these measurements are shown in table 5.4.

Table 5.4. Conditions used when measuring the inert build-up rate.

Parameter	Control
H_2 recirculation pump control voltage	100%
Anode set point pressure	200 mbar(g)
Blower control	~520 dm^3/min
Current	25 A...175 A (step 25 A)
Purge interval [11]	controlled manually
Anode purge length	0.5 s
Inert feed	0...1000 sccm [12]

5.2.3.2 *Measuring the effect of inert concentration on stack performance and fuel utilization*

The effect of inert concentration on stack performance and fuel utilization is investigated by operating the fuel cell system with low hydrogen concentrations in the anode loop. The feed rate of nitrogen is varied and the purge is done automatically when at least one cell voltage drops below a limiting value. The conditions used in these experiments are shown in table 5.5.

Table 5.5. Conditions in inert build-up measurements.

Parameter	Control
H_2 recirculation pump control voltage	100%
Anode set point pressure	200 mbar(g)
Load current	120 A
Blower control	$\lambda_{O2} = 2.5$
Purge interval	triggered by cell voltage below 500 mV
Anode purge length	0.5 s
Inert feed	varied

---

[11] Only anode purge, cathode purge not used. Also, the anode was not purged during measurements.

[12] The inert feed rate, if any, is relative to the current load in order to simulate different hydrogen purities.

6 Results and discussion

6.1 The results from ejector model simulations

6.1.1 The effects of stack flow resistance

The ejector model presented in section 4.1 was simulated as described in section 4.2.1 in order to investigate how the stack flow resistance affects the achievable recirculation rate. The results are presented in figure 6.1 and 6.2.

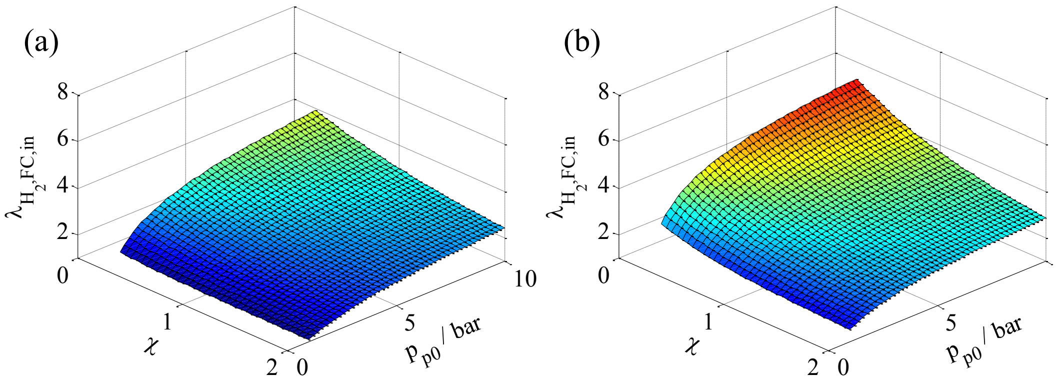

Figure 6.1. The effects of flow resistance and hydrogen feed pressure on stoichiometric ratio of hydrogen using ejectors (a) E_1 and (b) E_2.

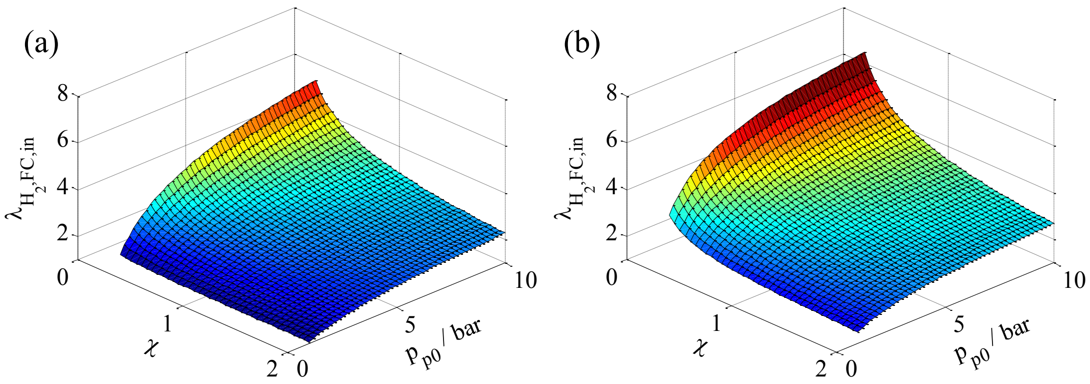

Figure 6.2. The effects of flow resistance and hydrogen feed pressure on stoichiometric ratio of hydrogen using ejectors (a) E_3 and (b) E_4.

From figures 6.1 and 6.2, it is seen that by reducing the stack flow resistance, the stoichiometric ratio of hydrogen and, hence, the recirculation rate increases. However, the increase in recirculation rate due to decreased flow resistance is ejector dependent and a function of hydrogen feed pressure. Figure 6.3 shows the percentual increase in hydrogen stoichiometry as a function of hydrogen feed pressure when the flow resistance of the stack is decreased by 50 %, i.e. χ is changed from 1.0 to 0.5.

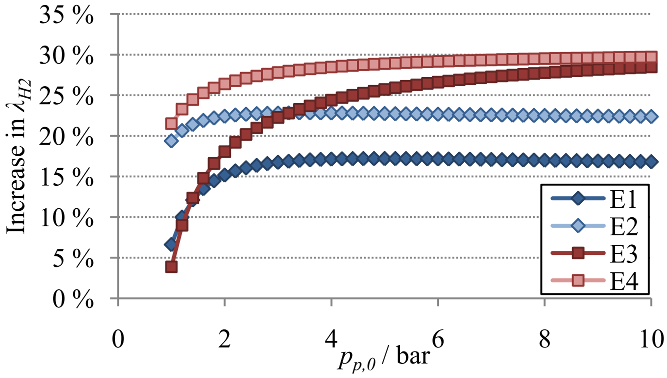

Figure 6.3. The percentual increase in hydrogen stoichiometry as a function of hydrogen feed pressure when the stack flow resistance is decreased by 50 %.

As seen in figure 6.3, the increase in recirculation rate achieved by reducing the stack flow resistance can be significant. Hence, by reducing the stack flow resistance, not only is the performance of the fuel cell increase through increased hydrogen partial pressure but also the durability is increased because hydrogen starvation can be avoided during transient conditions.

6.1.2 The effects of ejector dimensions

The effect of ejector dimension on the stoichiometric ratio of hydrogen entering the stack was investigated by simulating the ejector model as described in section 4.2.2. The results are presented in figure 6.4.

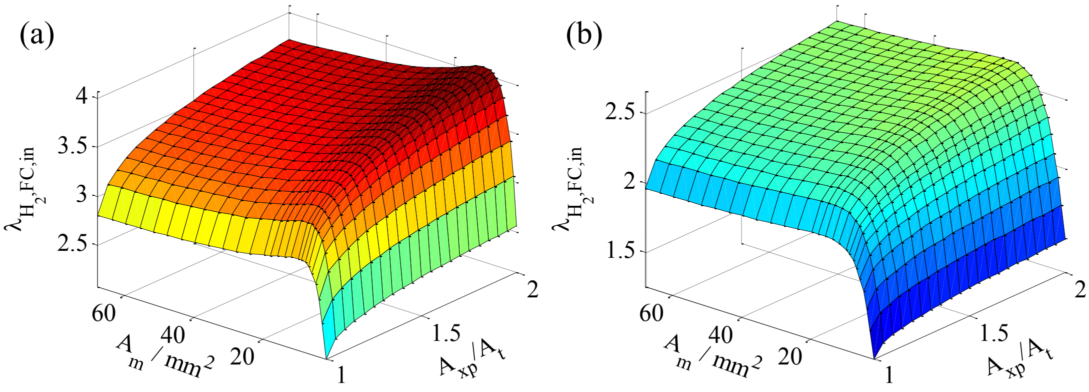

Figure 6.4. Stoichiometric ratio of hydrogen at the stack inlet as a function of mixing section area and the ratio of nozzle exit plane area to nozzle throat area. The stack inlet pressure was 1.3 bar and the current load was (a) 60 A and (b) 200 A.

From figures 6.4 (a) and (b), it can be seen that there is an optimal mixing section area for which the hydrogen stoichiometry is maximized. With higher hydrogen feed rate, shown in figure 6.4 (a), this optimal mixing section area is a bit larger than with the lower feed rate, shown in figure 6.4 (b). Furthermore, it can be seen that increasing the ratio of nozzle exit plane area to nozzle throat area yields higher stoichiometric ratios of hydrogen at the stack inlet. This can be explained with the increased primary fluid velocity at the beginning of the mixing section. The increased recirculation rate achieved with higher values of A_{xp}/A_t, however, comes with a price, as the required hydrogen feed pressure also increases. The feed pressures of hydrogen required to satisfy the constraints shown in table 4.5 are shown in figure 6.5.

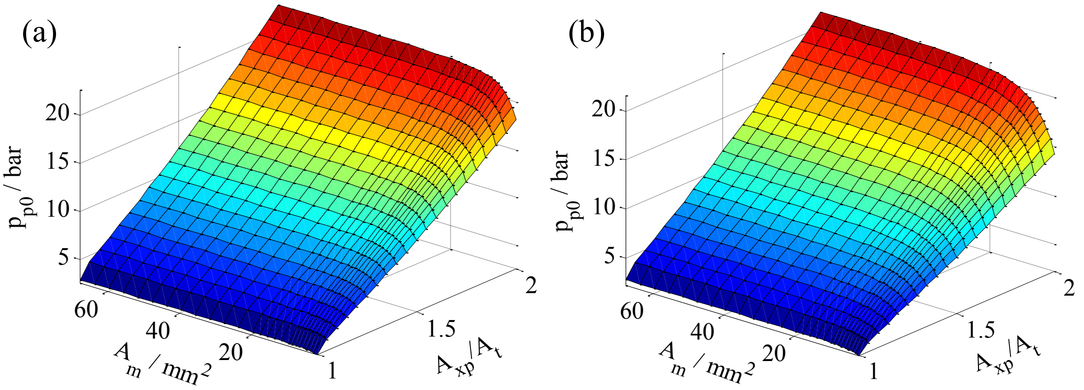

Figure 6.5. The hydrogen feed pressure, $p_{p,0}$, required to achieve 1.3 bar in stack inlet as a function of mixing section area and the ratio of nozzle exit plane area to nozzle throat area when hydrogen feed rate corresponds to (a) 60 A and (b) 200 A.

When comparing the achieved increase in hydrogen stoichiometry and the required hydrogen pressure, it can be concluded that maximizing the hydrogen recirculation rate by optimizing the ejector dimensions has a significant effect on the required hydrogen feed pressure. This, however, does not cause necessarily any added expenses in a fuel cell system where the fuel is stored pressurized, as the pressure in these storage containers can easily reach tens or even hundreds of bars in order to save space. Instead, the acceleration of the primary fluid to a high velocity will inevitably cause the fluid to cool down which might cause problems. The temperatures of the primary fluid at the beginning of the mixing section as a function of ejector dimensions are shown in figure 6.6.

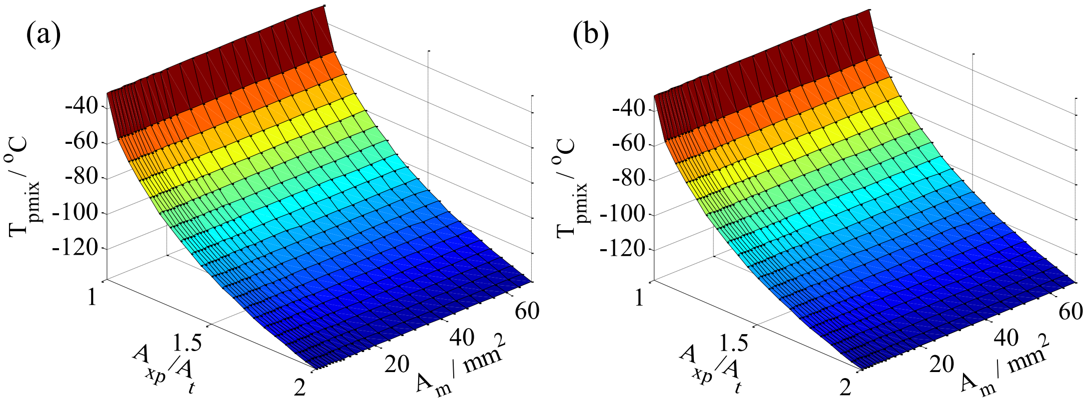

Figure 6.6. The temperature of the primary fluid at the beginning of the mixing section as a function of mixing section area and the ratio of nozzle exit plane area to nozzle throat area. The stack inlet pressure is 1.3 bar, and the current load is (a) 60 A and (b) 200 A.

As seen in figure 6.6, the temperature of the primary fluid accelerated to high velocity can be very low. When this cold stream comes in contact with the humid secondary stream in the mixing section, the humidity might condensate or even sublimate. To avoid this, the hydrogen fed to the system or recirculated can be heated.

To determine optimal ejector dimensions and the required hydrogen feed pressure based on the results presented in this subsection, it is assumed that lowest tolerated temperature of the primary fluid is -120 °C. The highest hydrogen stoichiometry is then achieved using hydrogen feed pressure and ejector dimensions shown in table 6.1.

Table 6.1. The optimal ejector dimensions, the required hydrogen feed pressure, and the achieved stoichiometric ratio of hydrogen at the stack inlet when the pressure at the inlet of a 64 cell stack is constrained to 1.3 bar.

Parameter	Partial load (60 A)	Full load (200 A)
A_t	0.05 mm^2	0.15 mm^2
A_{xp}	0.07 mm^2	0.25 mm^2
A_{mix}	12.0 mm^2	18.0 mm^2
$p_{p,0}$	14.8 bar	14.0 bar
$\lambda_{H2,FC,in}$	3.95	2.59

From table 6.1, it can be seen that the optimal ejector dimensions differ rather much between the two power levels. Therefore, if the fuel supply system should be able to supply hydrogen both at 60 A and 200 A, some of the methods discussed in the beginning of chapter 4 has to be used.

6.2 The results from calibration measurements

6.2.1 The volume of the anode compartment

The volume of the anode loop was measured as described in section 5.2.1.3 using different nitrogen feed rates. The pressure was a linear function of time in all measurements from which it can be concluded that there were no leakages. Therefore, equation (5.2) can be used. The measurement was repeated several times with each nitrogen feed rate, and the results are shown in table 6.2.

Table 6.2. The anode volume (dm^3) measured using different nitrogen feed rates.

#	Nitrogen feed rate / sccm			
	400	600	800	1000
1	2.67	2.62	2.62	2.61
2	2.62	2.61	2.62	2.60
3	2.61	2.62	2.62	2.60
4	-	2.61	2.61	2.60
5	-	-	2.61	2.59

Taking an average of the volumes shown in table 6.2, we get that the anode volume is

$$\bar{V}_{anode} = 2.61 \text{ dm}^3$$

6.2.2 The results from the hydrogen sensor system verification measurements

Figure 6.7 shows the results of three separate calibrations of the hydrogen sensor carried out as described in section 5.2.1.4 as well as the corrected values.

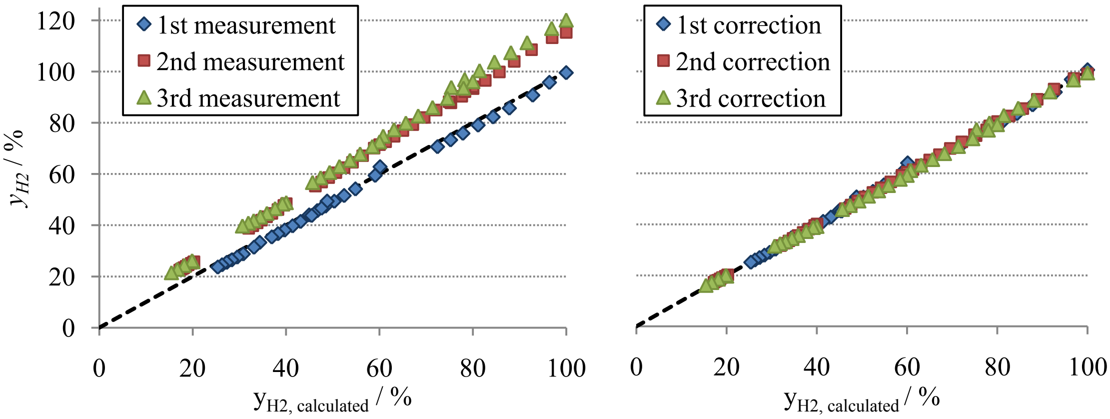

Figure 6.7. The (a) uncorrected and the (b) corrected hydrogen sensor readings. The dashed line represents the calculated hydrogen mole fractions.

The reading of the hydrogen sensor was found to drift between measurements, as seen in figure 6.7 (a). This was probably due to that the sensor was exposed to air which resulted in oxygen adsorption. Due to this drifting, the hydrogen sensor reading was corrected (figure 6.7 (b)). The corrections are shown in table 6.3.

Table 6.3. The corrections to the hydrogen sensor calibration results.

#	Correction
1	$y_{H2,\ corrected} = y_{H2,\ measured} \cdot 0.99 + 1.58$
2	$y_{H2,\ corrected} = y_{H2,\ measured} \cdot 0.88 - 2.45$
3	$y_{H2,\ corrected} = y_{H2,\ measured} \cdot 0.84 - 2.07$

The flow resistance of the hydrogen sensor loop was measured as described in section 5.2.1.5. Since the Reynolds numbers for the flow in the narrowest tube varied only little ($Re_t \approx 1000 \ldots 3000$) in the measurements, the quadratic term in equation (5.8) is assumed to be a linear function of the volume flow rate, i.e. a linearization of the Moody chart is used. Hence, equation (5.8) can be rewritten as follows

$$-\Delta p = \mu \cdot K_1 \cdot \dot{V} + \rho \cdot \left(K_2 + K_3 \cdot \dot{V}\right) \cdot \dot{V}^2$$

where K_1, K_2 and K_3 are constants specific to this particular piping. Figure 6.8 shows the measured pressure drop as a function of the volume flow rate.

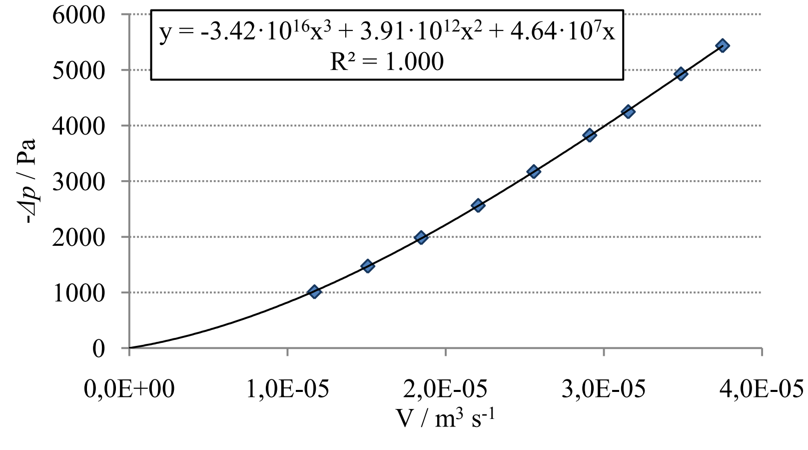

Figure 6.8. The measured pressure drop as a function of the volume flow rate.

The constants K_1, K_2 and K_3 can be solved from the trendline shown in figure 6.8 as follows

$$K_1 = \frac{4.64 \cdot 10^7 \frac{Pa\,s}{m^3}}{\mu_{N_2}} = \frac{4.64 \cdot 10^7 \frac{Pa\,s}{m^3}}{17.78 \cdot 10^{-6}\ Pa\,s} = 2.61 \cdot 10^{15} m^{-3}$$

$$K_2 = \frac{3.91 \cdot 10^{12} \frac{Pa\,s^2}{m^6}}{\rho_{N_2}} = \frac{3.91 \cdot 10^{12} \frac{Pa\,s^2}{m^6}}{1.17 \frac{kg}{m^3}} = 3.35 \cdot 10^{15} \frac{Pa\,s^2}{kg\,m^3}$$

$$K_3 = \frac{-3.42 \cdot 10^{16} \frac{Pa\,s^3}{m^9}}{\rho_{N_2}} = \frac{-3.42 \cdot 10^{16} \frac{Pa\,s^3}{m^9}}{1.17 \frac{kg}{m^3}} = -2.93 \cdot 10^{19} \frac{Pa\,s^3}{kg\,m^6}$$

The density of nitrogen is calculated assuming ideal gas behaviour, and the viscosity of nitrogen is taken from reference (Seibt et al. 2006).

6.3 The results from initial testing of the setup

The initial testing of the assembled system was carried out as described in section 5.2.2 through 16 steady state measurements. The time average current loads, anode pressures, stack voltages, and hydrogen recirculation pump control values during these tests are shown in table 6.4.

Table 6.4. The time average current loads, hydrogen recirculation pump control values, anode inlet and outlet pressures, as well as stack voltages in initial testing of the system.

#	I / A	H_2 recirculation [13] / %	$p_{anode,in}$ / mbarg	$p_{anode,out}$ [14] / mbarg	U_{stack} / V
1	119.8	0	146.0	123.1	42.4
2	119.8	33	125.5	100.5	44.0
3	119.8	66	132.1	102.9	44.1
4	119.8	100	109.2	73.7	44.1
5	119.8	0	330.2	307.3	43.8
6	119.8	33	311.2	286.2	44.0
7	119.8	66	307.9	278.7	44.1
8	119.8	100	290.3	254.7	44.1
9	160.0	0	134.9	107.0	39.9
10	160.0	33	118.7	91.3	40.2
11	160.0	66	121.9	90.1	40.4
12	160.0	100	99.0	57.9	40.5
13	159.6	0	321.4	293.6	41.0
14	160.0	33	303.2	275.8	41.6
15	160.0	66	307.4	275.6	41.7
16	160.0	100	306.1	265.0	41.8

---

[13] Hydrogen recirculation pump control voltage relative to the maximum control voltage

[14] The pressure difference over the stack was measured separately as a function of hydrogen recirculation rate with different current loads and the results are used here to calculate the anode outlet pressure from the anode inlet pressure.

6.3.1 The performance of the hydrogen recirculation pump

The measured time average anode inlet and outlet temperatures as well as the relative humidities of anode inlet and outlet gases are presented in table 6.5.

Table 6.5. The time average anode inlet and outlet temperatures as well as the relative humidities of anode inlet and outlet gases.

#	$T_{anode,in}$ / °C	$T_{anode,out}$ / °C	$Ø_{anode,in}$ / %	$Ø_{anode,out}$ / %
1	56.3	57.6	0.0	100.0
2	54.5	56.9	25.2	100.0
3	53.4	56.9	40.0	99.9
4	51.7	57.4	56.5	99.9
5	56.5	57.5	0.0	99.9
6	54.6	57.4	30.2	99.9
7	52.9	57.2	46.7	99.9
8	51.7	57.3	61.4	99.9
9	55.0	58.5	0.0	99.9
10	53.6	58.1	22.8	99.9
11	51.9	58.2	37.5	99.9
12	50.6	58.0	52.8	99.9
13	55.4	58.9	0.0	99.9
14	53.5	58.3	25.2	99.9
15	52.3	58.3	40.9	99.9
16	50.5	58.4	59.6	99.9

From the results shown in table 6.5, the recirculation rate can be solved using the overall material balance

$$\dot{n}_{tot,out} + \dot{n}_{H_2,feed} = \dot{n}_{tot,in} \tag{6.1}$$

and the water balance

$$\dot{n}_{tot,out} \cdot y_{H_2O,out} = \dot{n}_{tot,in} \cdot y_{H_2O,in} \tag{6.2}$$

arriving at

$$\dot{n}_{tot,out} = \dot{n}_{H_2,feed} \cdot \left(\frac{y_{H_2O,in}}{y_{H_2O,out} - y_{H_2O,in}}\right) \tag{6.3}$$

where $\dot{n}_{tot,out}$ is the molar flow rate of recirculated gas. By using equation (3.16), $y_{H_2O,in}$ and $y_{H_2O,out}$ can be calculated from the anode inlet and outlet temperatures and relative humidities, respectively, as follows

$$y_{H_2O,in} = \emptyset_{anode,in}\frac{p^S_{H_2O}(T_{anode,in})}{p_{anode,in}}, \tag{6.4}$$

$$y_{H_2O,out} = \emptyset_{anode,out}\frac{p^S_{H_2O}(T_{anode,out})}{p_{anode,out}}. \tag{6.5}$$

Assuming only hydrogen and water in the anode loop, the stoichiometric ratio of hydrogen at the stack inlet is

$$\lambda_{H_2} = \frac{\dot{n}_{tot,in}\cdot(1-y_{H_2O,in})}{\dot{n}_{H_2,feed}} \tag{6.6}$$

which by using equations (6.1) and (6.3) can be written as follows

$$\lambda_{H_2} = \frac{y_{H_2O,out}\cdot(1-y_{H_2O,in})}{y_{H_2O,out}-y_{H_2O,in}}. \tag{6.7}$$

The vapour pressure of water as a function of temperature is taken from reference (Keskinen 1989). The calculated stoichiometric ratios of hydrogen at the stack inlet are presented in figure 6.9.

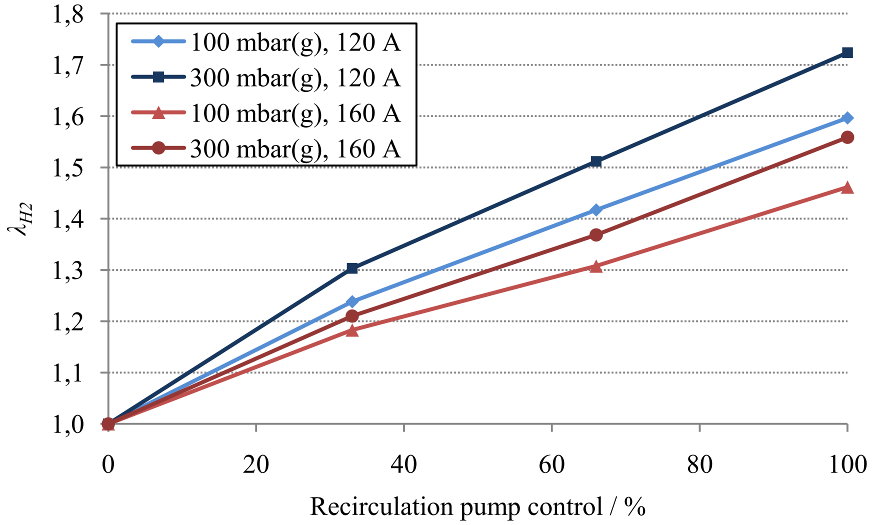

Figure 6.9. The calculated stoichiometric ratio of hydrogen at the stack inlet as a function of the hydrogen recirculation pump control.

Based on figure 6.9, it can be concluded that the achievable recirculation rate is sufficient when the concentration of impurities in the recirculated stream is low. However, as the build-up of impurities in the recirculated stream changes the stoichiometry of hydrogen, a more powerful recirculation pump might be needed especially when operating the stack with low hydrogen mole fractions and at high current loads.

The anode stream is heated before entering the stack. Therefore, the anode inlet temperatures and relative humidites shown in table 6.5 are not the temperatures and relative humidities of the gas mixture resulting when the recirculated gas is mixed with the fresh hydrogen feed. The relative humidity of the mixed stream can be calculated as follows

$$\emptyset_{mixed} = \frac{y_{H_2O,mixed} \cdot p_{anode,in}}{p^s_{H_2O}(T_{mix})} \tag{6.8}$$

where the mole fraction of water in the mixed stream, $y_{H_2O,mixed}$, is based on the mole balance of water

$$y_{H_2O,mixed} = \frac{\dot{n}_{tot,out} \cdot y_{H_2O,out}}{\dot{n}_{tot,out} + \dot{n}_{H_2,feed}}. \tag{6.9}$$

The temperature of the mixed gas, T_{mix}, is calculated from the energy balance as follows

$$\bar{c}_{p,H_2,a,out} \cdot \dot{m}_{H_2,a,out} \cdot \left(T_{a,out} - T_{mix}\right) + \bar{c}_{p,H_2O,a,out} \cdot \dot{m}_{H_2O,a,out} \cdot \ldots$$

$$\left(T_{a,out} - T_{mix}\right) + \bar{c}_{p,H_2,feed} \cdot \dot{m}_{H_2,feed} \cdot \left(T_{H_2,feed} - T_{mix}\right) = 0 \tag{6.10}$$

where the heat capacities of the gases $\bar{c}_{p,H_2,anode,out}$, $\bar{c}_{p,H_2O,anode,out}$, and $\bar{c}_{p,H_2,feed}$ are calculated in the mean temperatures.

The calculations were carried out with three different temperatures of the fresh hydrogen (20 °C, 30 °C and 40 °C) and the calculated relative humidities of the mixed stream are shown in figure 6.10. The temperature of the fresh hydrogen feed was not measured but it was most likely close to room temperature, i.e. 20 °C.

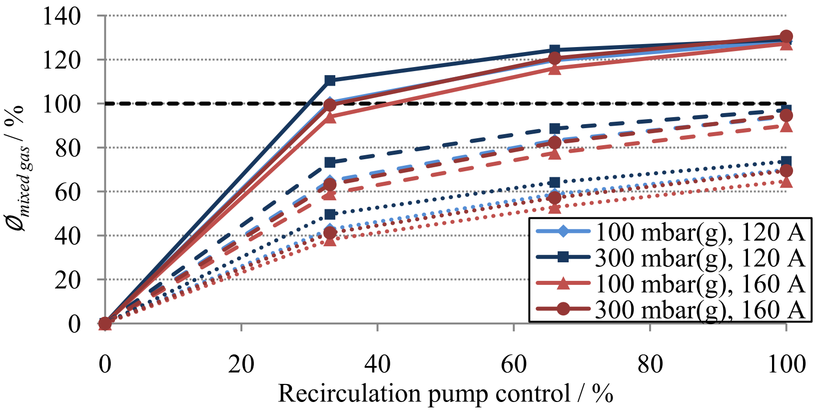

Figure 6.10. The calculated relative humidities of the mixed stream. The temperature of the fresh hydrogen is assumed to be 20 °C for the solid lines, 30 °C for the dashed lines and 40 °C for the dotted lines.

It is concluded that local condensation might occur during the mixing process, but the liquid water, if any, is evaporated before entering the stack as seen in table 6.5. Furthermore, the condensation of water during mixing of the two gas streams can be avoided by preheating both or either of the streams.

6.3.2 The performance of the air blower

The measured time average current loads and air volume flow rates are presented in table 6.6.

Table 6.6. Measured time average current loads and air flow rates [15].

#	I / A	Air flow rate / dm^3 min^{-1}
$(1,2,3,4)_{\text{average}}$	119.8	417.4
$(5,6,7,8)_{\text{average}}$	119.8	418.2
$(9,10,11,12)_{\text{average}}$	160.0	463.8
$(13,14,15,16)_{\text{average}}$	159.9	462.7

Assuming ideal gas behaviour, the stoichiometric ratio of oxygen fed to the stack can be calculated as follows

$$\lambda_{O_2} = \frac{y_{O_2} \cdot \dot{V}_{air} \cdot p}{T \cdot R} \cdot \frac{4 \cdot F}{N_{cells} \cdot I}. \tag{6.11}$$

The calculated stoichiometric ratios of oxygen, assuming the mole fraction of oxygen in air is 0.21, are presented in table 6.7.

Table 6.7. Calculated stoichiometric ratios of oxygen.

#	λ_{O2}
$(1,2,3,4)_{\text{average}}$	3.0
$(5,6,7,8)_{\text{average}}$	3.0
$(9,10,11,12)_{\text{average}}$	2.5
$(13,14,15,16)_{\text{average}}$	2.5

As mentioned in section 5.1, the cathode is purged simultaneously with the anode purge. During the cathode purge, the flow rate of air exceeds 610 litres per minute corresponding to a stoichiometric ratio of about 4.4 at a load of 120 A, about 3.3 at a load of 160 A, and about 2.3 at a load of 230 A. Hence, it can be concluded that the air blower is well dimensioned for this particular stack.

---

[15] The measured air flow rate includes the increased flow rate during purges. Hence, the average flow rate excluding purges is a few litres per minute lower than the given flow rate.

6.3.3 The performance of the cooling system

The time average coolant inlet and outlet temperatures, coolant flow rates, and the percentual time the coolant valve being open in the initial tests are shown in table 6.8.

Table 6.8. Time average coolant in- and output temperatures, coolant flow rate, and the percentual time the coolant valve being open.

#	$\dot{V}_{coolant}$ / $dm^3\ min^{-1}$	$T_{coolant,in}$ / °C	$T_{coolant,out}$ / °C	$\frac{t_{valve\ open}}{t_{total}}$ / %
$(1,2,3,4)_{average}$	13.9	50.7	54.8	19.1
$(5,6,7,8)_{average}$	12.0	50.6	55.2	19.5
$(9,10,11,12)_{average}$	13.8	50.9	57.0	27.3
$(13,14,15,16)_{average}$	12.0	50.6	57.4	27.1

From the temperatures and the coolant flow rates shown in table 6.8, the cooling power of the heat exchanger can be calculated as follows

$$\dot{Q}_{HE} = c_p \cdot \dot{V}_{coolant} \cdot \rho_{coolant} \cdot \Delta T. \tag{6.12}$$

If it is assumed that the heat exchanger transfers heat only when the coolant valve is open, i.e. when cold water flows through the shell side of the heat exchanger, the maximum rate of heat transfer can be approximated as follows

$$\dot{Q}_{HE,max} = \frac{\dot{Q}_{HE}}{\frac{t_{valve\ open}}{t_{total}}}. \tag{6.13}$$

The calculated cooling powers and the approximate maximum cooling powers of the cooling system are shown in table 6.9.

Table 6.9. Calculated cooling powers and approximate maximum cooling powers of the cooling system. The numerical values for heat capacity and density of water are taken from reference (Keskinen 1989).

#	$\dot{Q}_{HE}$ / kW	$\dot{Q}_{HE,max}$ / kW
$(1,2,3,4)_{average}$	3.95	20.64
$(5,6,7,8)_{average}$	3.78	19.44
$(9,10,11,12)_{average}$	5.84	21.35
$(13,14,15,16)_{average}$	5.62	20.74

Based on the results shown in table 6.9, it can be concluded that the cooling power of the cooling system suffices even for larger fuel cell stacks. It can also be seen that measurements with the higher anode pressure, i.e. measurements 5…8 and 13...16, have lower heat transfer rates than does the measurements with lower anode pressure. The reason for this was found to be hydrogen leaking into the coolant channels, thus affecting the recirculation rate of the coolant water, as seen in table 6.8.

6.4 The results from inert build-up measurements

The inert build-up measurements were conducted as described in section 5.2.3. The results from measuring the inert build-up rate are presented in section 6.4.3, and the results of investigating the effects of inert build-up on fuel cell stack performance are presented in section 6.4.4. In addition, the results from the measurements described in section 5.2.3.1 were used to determine the purity of hydrogen, the gas permeability of the membrane, and the fraction of the recirculated stream passing the hydrogen sensor. The results of these measurements are presented in sections 6.4.1 and 6.4.2, respectively.

6.4.1 The determined flow rate through the hydrogen sensor

As mentioned in section 5.2.1.5, the flow of the sample stream passing the hydrogen sensor was driven by the pressure gradient. By using equation (5.8) and the parameters calculated in section 6.2.2, the fraction of anode outlet gas passing the hydrogen sensor was calculated. The calculations were based on time average pressure difference, anode outlet pressure, anode outlet temperature, and anode outlet gas composition of the measurements presented in section 5.2.3.1. The results are shown in figure 6.11 together with the time it takes to replace the volume of the hydrogen sensor loop.

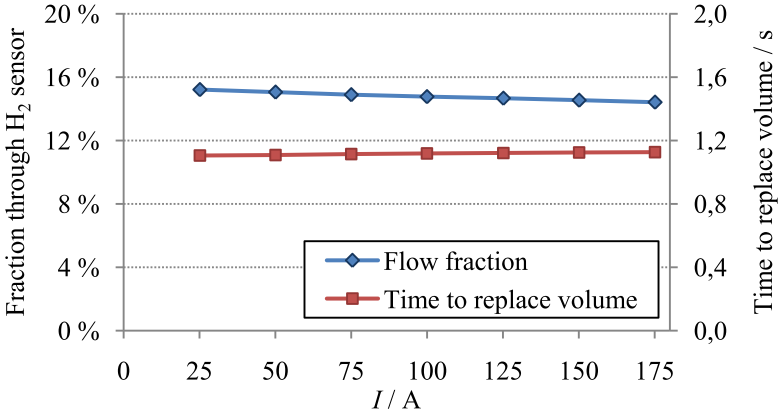

Figure 6.11. The fraction of anode outlet gas passing the hydrogen sensor and the time it takes to replace the volume of the hydrogen sensor loop as a function of current load.

From figure 6.11, it can be concluded that the flow rate through hydrogen sensor loop is almost independent of the current load despite the increased pressure gradient with increasing current load. This can be explained with the increased viscosity and density of the gas mixture due to increased water mole fraction.

As the gas passing the hydrogen sensor is dried, the flow rate should be kept relatively low to avoid membrane dehydration. By using a separate pump to circulate the gas mixture, the humidity of the recirculated anode gas could be controlled more accurately.

6.4.2 The measured hydrogen purity and membrane permeability

Figure 6.12 shows the measured hydrogen mole fraction as a function time in one of the measurements described in section 5.2.3.1. In this experiment, no nitrogen was fed into the anode loop.

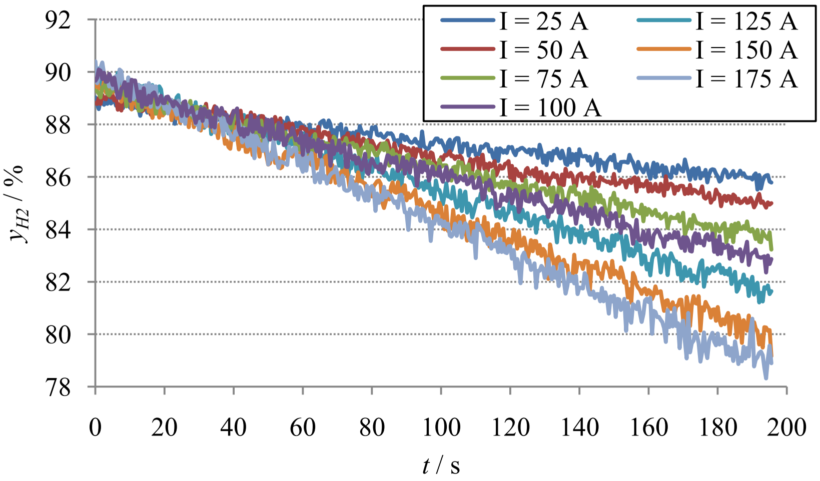

Figure 6.12. The measured hydrogen mole fraction as a function time.

The noise observed in the results shown in figure 6.12 is caused by the fluctuating pressure used for scaling the hydrogen sensor reading. The fluctuating pressure is in turn caused by the diaphragm pump used for recirculating the unconsumed hydrogen.

Assuming that the recirculated stream behaves like an ideal gas, the total rate of inert gas build-up in the anode loop can be calculated as follows

$$\dot{n}_{inert,in} = -\frac{dn_{H_2}}{dt} = -n_{total}\frac{dy_{H_2}}{dt} = -\frac{\bar{p}_{anode} \cdot V_{anode}}{R \cdot \bar{T}_{anode}}\frac{dy_{H_2}}{dt}. \tag{6.14}$$

However, as the hydrogen sensor in the current setup measures the mole fraction of hydrogen in the dried sample stream, the change in y_{H_2} is not representative for the total hydrogen mole fraction depletion rate in the anode loop where also water vapour exists.

Hence, a correction has to be made to equation (6.14) to take into account the volume taken by the water vapour. The exact volume taken by water vapour was not possible to measure with current setup, so the average water partial pressure in the anode loop was assumed to be the vapour pressure of water in the temperature of gas entering the anode,

$$\bar{p}_{H_2O} \approx p^s_{H_2O}\left(\bar{T}_{anode,in}\right). \tag{6.15}$$

Hence, the average water mole fraction in the anode loop was

$$\bar{y}_{H_2O} = \frac{p^s_{H_2O}\left(\bar{T}_{anode,in}\right)}{\bar{p}}, \tag{6.16}$$

and equation (6.14) can be rewritten as follows

$$\dot{n}_{inert,in} = \left(\bar{y}_{H_2O} - 1\right) \cdot V_{anode} \cdot \frac{\bar{p}_{anode}}{R \cdot \bar{T}_{anode}} \frac{dy_{H_2}}{dt}. \tag{6.17}$$

Using equation (6.17) and the slopes of the measured hydrogen mole fractions shown in figure 6.12, the inert build-up rates can be expressed as a function of the current load, as shown in figure 6.13.

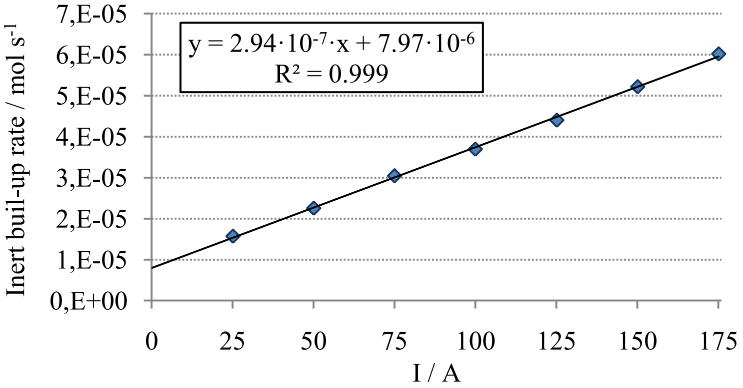

Figure 6.13. The calculated inert build-up rate as a function current load.

The intercept of the trendline shown in figure 6.13 is the inert build-up rate when hydrogen is not fed. In other words, the intercept equals the membrane permeability. As the active area of each cell is 200 cm^2 and there were 64 cells in the stack, the average inert gas flux through the membrane was

$$\dot{n}_{inert,membrane} = \frac{7.97 \cdot 10^{-6} \frac{mol}{s}}{64 \cdot 200\ cm^2 \cdot \frac{m^2}{10000\ cm^2}} = 6.23 \cdot 10^{-6} \frac{mol}{m^2\ s}.$$

Assuming a membrane thickness of 35 μm, the above calculated figure is several orders of magnitude higher than the modelling results by (Ahluwalia, Wang 2007) and the experimental data from (Baik, Kim 2010). It is concluded that there exists leakages in the membrane that cause such high membrane permeability.

From the slope of the trendline shown in figure 6.13, the hydrogen purity can be determined as follows

$$y_{H_2,feed} = 1 - \frac{2F}{64}\frac{d\dot{n}_{inert,in}}{dI} = 1 - \frac{2\cdot 96485\frac{C}{mol}}{64}\cdot 2.94\cdot 10^{-7}\,\frac{mol}{A\,s} = 0.999.$$

6.4.3 The effects of hydrogen purity on the inert build-up rate

The inert build-up rate was measured as described in section 5.2.3.1 using different purities (99.9 %, 99.5 %, 99.1 %, and 98.7 %) of the hydrogen fed. The corrected mole fractions of hydrogen as a function of time are shown in figure 6.14.

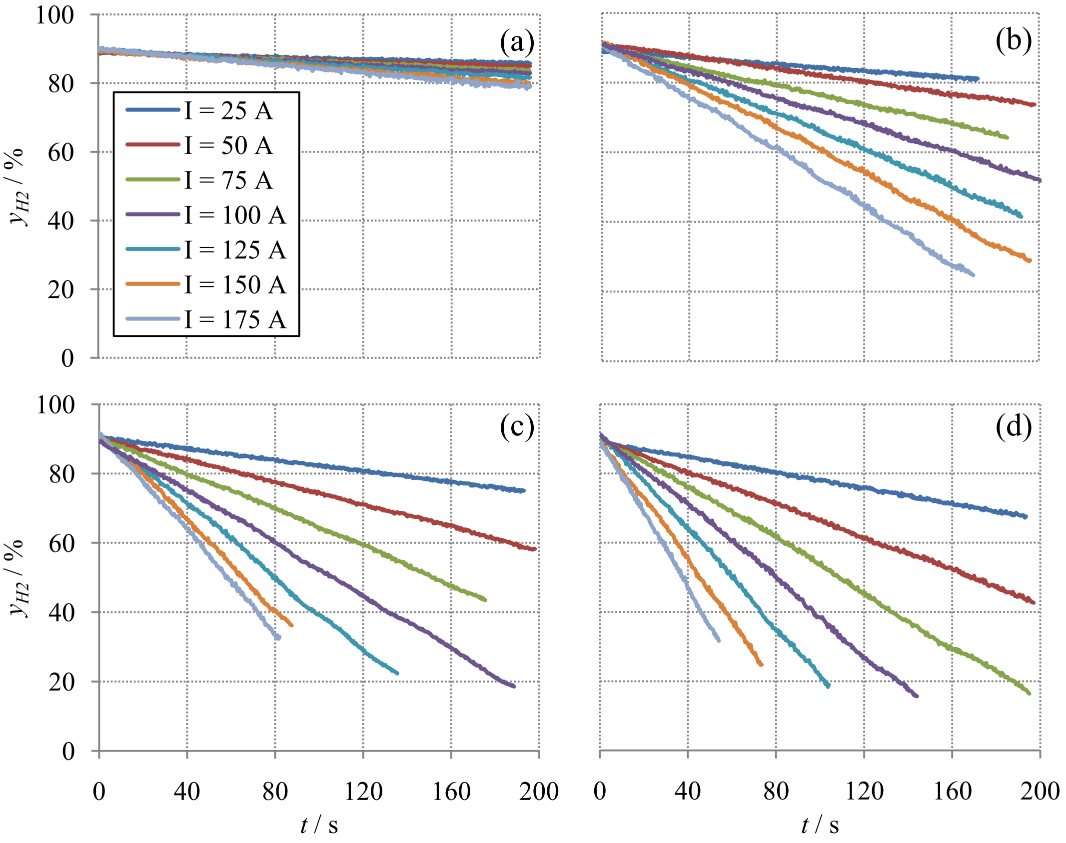

Figure 6.14. Hydrogen mole fraction as a function time when using different feed hydrogen purities: (a) $y_{H_2,feed}$ = 99.9 %, (b) $y_{H_2,feed}$ = 99.5 %, (c) $y_{H_2,feed}$ = 99.1 % and (d) $y_{H_2,feed}$ = 98.7 %.

From figure 6.14, it can be seen that the mole fraction of hydrogen decreased linearly as a function of time, i.e. the membrane permeability was not affected by the inert concentration in the anode loop in contrast to what was stated by (Ahluwalia, Wang 2007). This, however, supports the conclusion of leakages existing in the membrane, causing nitrogen to enter the anode at a high rate independent of the power level.

Figure 6.15 shows both the measured and the calculated inert accumulation rates when using different feed hydrogen purities (99.9 %, 99.5 %, 99.1 %, and 98.7 %). The calculated inert build-up rates are based on the amount of nitrogen fed as well as on the membrane permeability and hydrogen purity presented in section 6.4.2.

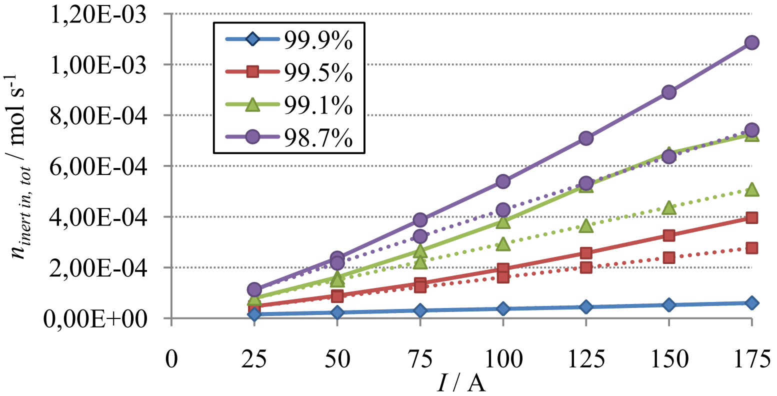

Figure 6.15. The measured (solid lines) and the calculated (dotted lines) inert accumulation rates when using different feed hydrogen purities (99.9 %, 99.5 %, 99.1 %, and 98.7 %).

From figure 6.15, it can be seen that the higher the nitrogen feed rate was, the more the measured inert build-up rates deviated from the calculated ones. Hence, it can be concluded that the mass flow controller used for feeding the nitrogen is accurate only at low flow rates.

Figure 6.16 shows the fraction of measured inert build-up caused by the inert entering with fuel as a function of current load with different hydrogen purities. Here it is assumed that the rate at which inert gas diffuses from the cathode through the membrane to the anode remains constant.

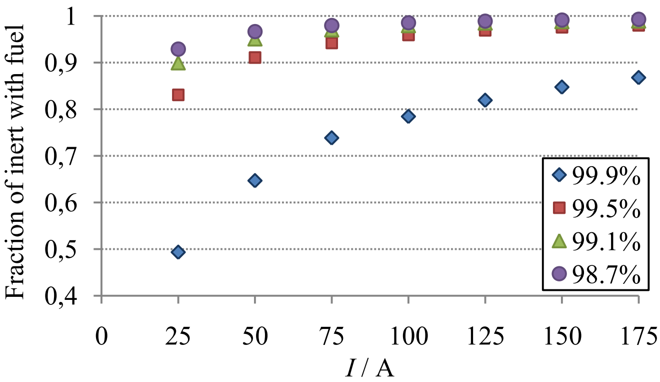

Figure 6.16. The fraction of inert build-up caused by the inert entering with fuel as a function of current load with different hydrogen purities.

From figure 6.16, it can be seen that as the purity of hydrogen decreases, the fraction of the total inert build-up rate caused by membrane permeation becomes unsubstantial. It is important to remember here that in these measurements, the amount of inert entering from the cathode was several orders of magnitude higher than reported elsewhere (Ahluwalia, Wang 2007; Baik, Kim 2010). Therefore, in “normal” PEMFCs the membrane permeation has an even lower effect on the total inert build-up rate than seen in figure 6.16 and correspondingly the effect of hydrogen purity is stronger.

6.4.4 The effects of inert build-up on stack performance and fuel utilization

Figure 6.17 shows a drive cycle where the nitrogen feed rate was varied and the purges were triggered by low cell voltages.

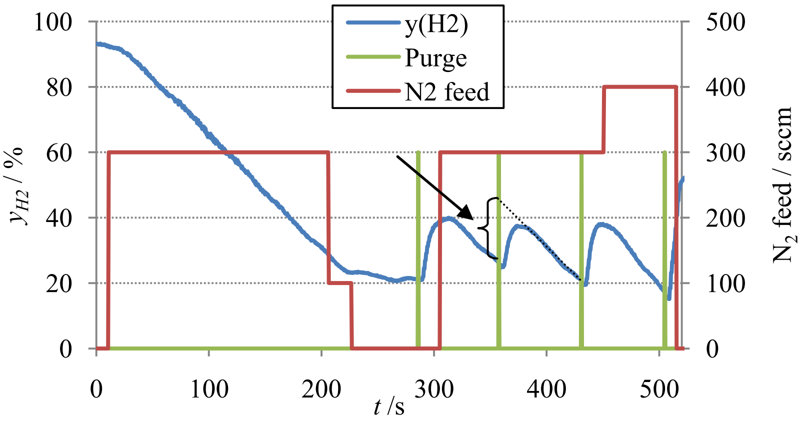

Figure 6.17. The drive cycle showing the inert feed rate, hydrogen mole fraction, and the purges.

From figure 6.17, it is seen how the mole fraction of hydrogen in the anode loop behaves during purges. Particularly, the rounded shape of the hydrogen mole fraction after a purge reveals that there is some delay in the hydrogen sensor reading. This is partly explained with the limited flow rate through the hydrogen sensor loop covered in section 6.4.1.

Concentrating on the second purge, the hydrogen mole fraction in the dried stream immediately after the purge can be estimated to be 46 %, as shown in figure 6.17. The dry hydrogen mole fraction just before the purge is 26 %. Correcting these mole fractions to account for the water content in the anode outlet gas during the purge, we have

$$y_{H_2,before} = y_{H_2} \cdot \left(1 - y_{H_2O}\right) = 0.26 \cdot (1 - 0.16) = 0.22,$$

$$y_{H_2,after} = y_{H_2} \cdot \left(1 - y_{H_2O}\right) = 0.46 \cdot (1 - 0.16) = 0.39.$$

The amount of gas purged can be calculated by establishing a hydrogen balance as follows

$$V_{purged} = V_{anode} \cdot \frac{y_{H_2,after} - y_{H_2,before}}{y_{H_2,feed} - y_{H_2,purged}}. \tag{6.18}$$

As nitrogen was fed at a rate of 300 sccm, the purity of the hydrogen in the feed stream was 99.4 %. Hence, if assuming $y_{H_2,purged} = y_{H_2,before}$, the volume purged under the anode pressure is

$$V_{purged} = 2.61\ dm^3 \cdot \frac{0.39 - 0.22}{0.994 - 0.22} = 0.57\ dm^3.$$

Assuming ideal gas behaviour, the amount of hydrogen lost in the purge is

$$n_{H_2,purged} = \frac{p_{anode} \cdot V_{purged} \cdot y_{H_2,purged}}{R \cdot T_{anode}}. \tag{6.19}$$

Hence, with the amount of hydrogen lost during purge, the stack could have been operated for

$$\Delta t = \frac{n_{H_2,purged} \cdot 2 \cdot F}{I \cdot 64} = \frac{121825\ Pa \cdot 0.57\ dm^3 \frac{m^3}{1000\ dm^3} \cdot 0.22}{8.31451 \frac{J}{K\ mol} \cdot 331\ K} \cdot \frac{2 \cdot 96485 \frac{C}{mol}}{120\ A \cdot 64} = 0.14\ s$$

according to Faraday's law.

As the amount of hydrogen lost in the purge is directly proportional to the hydrogen mole fraction in the purged gas, it is advantageous to operate the fuel cell with a low hydrogen concentration. However, the hydrogen concentration affects the fuel cell performance through decreased mass transport rate leading to lowered cell voltages which equals lower efficiency. Figure 6.18 shows the cell voltages together with the mole fraction of hydrogen in the same drive cycle as shown in figure 6.17. The cell voltages are shown as average values of the strongest cells (normal cells) and the weakest cells.

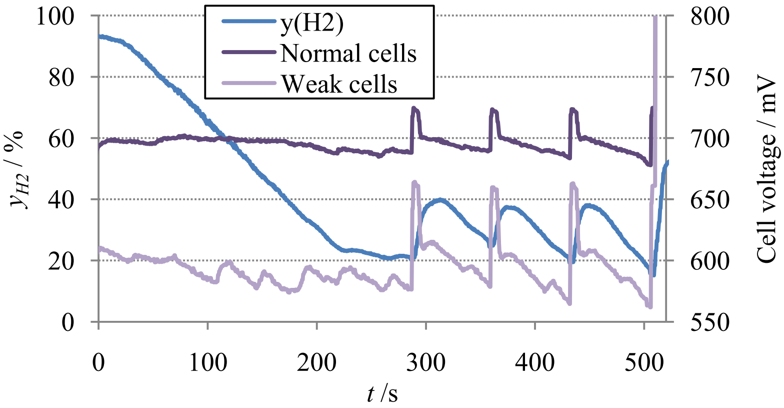

Figure 6.18. The dependency of cell voltages on dry hydrogen mole fraction.

From figure 6.18, it can be seen how the performance of the weak cells differed from the performance of normal cells when exposed to low hydrogen concentrations: the voltage of the weaker cells was much more sensitive to low hydrogen concentrations and to the temperature than the voltage of normal cells. The effect of the concentration of hydrogen on cell voltages is best seen between the purges while the effect of the temperature is best seen before the first purge in figure 6.18. Furthermore, the increased flow rate during a purge, observed as peaks in the cell voltages, had a much stronger effect on the cell voltages of weak cells than it did on normal cells. The conclusion based on this is that the weak cells seem to suffer from a higher mass transport resistance than the normal ones. Thus, the optimal purge interval depends not only on the recirculation rate, covered in section 3.1.3.3, and on the inert build-up rate, but also on the condition of the cells.

7 Conclusions and future work

In this work the recirculation of PEMFC anode exhaust gas was studied through modelling and experimental work. The modelling work consisted of modelling an ejector while the experimental work concentrated on investigation of the build-up of inert gases in the recirculated stream. The fuel cell system used in investigating the inert build-up in this work was assembled and tested prior to the inert build-up tests. Here the results are summarized and future work is proposed.

7.1 Modelling an ejector

In the modelling part of this work a steady state, one-dimensional ejector model was developed. The model was simulated to investigate the effects of the flow resistance of the stack and the dimensions of the ejector on the achievable recirculation rate. It was found that the flow resistance of the stack can have a notable effect on the achievable recirculation rate, but the effect is highly dependent on the ejector dimensions. Moreover, the recirculation rate can be increased by optimizing the dimensions of the ejector. However, maximizing the recirculation rate by optimizing the ejector dimensions influences the required feed pressure of hydrogen and the temperature of the hydrogen accelerated to high velocity. It was concluded that while the high required hydrogen feed pressure is not necessarily a problem due to high pressure storages, the temperature of the accelerated hydrogen probably will be in PEMFC systems where high humidity of the recirculated stream is desirable.

The developed ejector model is based on the ideal gas assumption, on the assumptions of constant pressure and constant area mixing as well as on the assumption that friction losses of the flow and losses of the two gases mixing are independent of the temperature, pressure, velocity and composition of the gases. Modelling the flow inside the ejector, especially the mixing process, more accurately and taking into account the real behaviour of the gases would doubtless lead to more reliable results.

7.2 Assembling and testing an 8 kW$_e$ PEM fuel cell system

In the experimental part of this work, a complete 8 kW$_e$ PEM fuel cell system was reassembled from a power pack into a fume hood. The function of the newly assembled system was verified through steady state experiments with variable loads, hydrogen recirculation rates, and anode pressures. Based on the results from these measurements the dimensioning of the hydrogen recirculation pump, the air blower, and the heat exchanger was studied. The dimensioning of the air blower was found to be suitable for the system at hand. However, this was not the case for the hydrogen recirculation pump and the heat exchanger. The hydrogen recirculation rate achievable with the pump used in this work was found to be sufficient even at high current loads when the inert concentration in the recirculated stream is low. However, when operating the stack at high inert concentrations in the recirculated stream, the stoichiometric ratio of hydrogen at the anode inlet decreases notably. The heat exchanger on the other hand, was found to have a much higher maximum cooling capacity than needed in the current setup. However, the cooling power was found to depend on the anode pressure which was found to be a consequence of anode gas leaking into the coolant loop, thus decreasing the coolant flow rate

The purpose of reassembling the 8 kW$_e$ system into a fume hood was to be able to easily exchange components and to test varying system combinations. During the verification tests and the inert build-up measurements, it was observed that the current cooling system caused the temperature of the stack to fluctuate somewhat. This caused some fluctuation of the cell voltages at high loads as well as of the temperatures of gas in the anode loop and air leaving the cathode. Furthermore, the diaphragm pump used in this work for recirculating the unconsumed hydrogen caused some noise to the hydrogen sensor reading. Therefore, it is suggested that the hydrogen recirculation and the thermal management are improved to achieve better results in the future.

7.3 Inert build-up in the anode loop due to recirculation

The assembled 8 kW$_e$ PEM fuel cell system was used for investigating the inert build-up rate as well as the effects of inert build-up on the performance of the stack and the utilization of fuel. The rate of inert build-up was measured as a function of the current load and the purity of the fuel. Different purities of the fuel were simulated by feeding nitrogen into the anode loop.

From the measurement results, the purity of the hydrogen used as fuel as well as the inert build-up rate due to membrane permeation were determined. It was concluded that the measured membrane permeation was several orders of magnitude higher than the modelling results and measured values reported by Ahluwalia & Wang (2007) and Baik & Kim (2010), respectively. The reason for this was assumed to be leakages in the stack. Because of the leakages in the membrane, the proportion of inert build-up caused by impurities in the fuel was lower than in “normal” fuel cell systems. Nonetheless, the impurities in fuel caused a major part of the inert build-up especially at high current loads and when using lower quality hydrogen.

The effects of inert build-up on the performance of the stack and on the utilization of fuel were investigated by operating the FCS at constant load and recording the hydrogen mole fraction as well as the cell voltages. Because of the high age of the fuel cell stack, there were deviations in performance of the cells. Thus, the effects of inert build-up on cell performance were obtained for both normal cells and for weak cells. The results revealed that the inert build-up has a much stronger effect on the weaker cells. It was concluded that the optimal purge interval depends not only on the recirculation rate and on the inert build-up rate, but also on the condition of the cells.

An investigation of the combined effects of recirculation rate and inert build-up on stack performance is suggested as future work. The increased recirculation rate results in the ability to operate the stack at lower hydrogen concentrations, thus resulting in higher fuel utilization through decreased loss of hydrogen during purges. Moreover, the increased recirculation rate translates into higher anode inlet humidity, thus making the water distribution in the stack more even. The drawback of increasing the recirculation is the increased consumption of energy which translates into lowered overall efficiency of the system. However, when using an ejector to recirculate the unspent hydrogen, there is no added energy consumption.

8 References

Ahluwalia, R.K., Hua, T.Q. & Peng, J.K. 2007, "Fuel cycle efficiencies of different automotive on-board hydrogen storage options", *International Journal of Hydrogen Energy,* vol. 32, no. 15, pp. 3592-3602.

Ahluwalia, R.K. & Peng, J.K. 2008, "Dynamics of cryogenic hydrogen storage in insulated pressure vessels for automotive applications", *International Journal of Hydrogen Energy,* vol. 33, no. 17, pp. 4622-4633.

Ahluwalia, R.K. & Wang, X. 2008a, "Effect of CO and CO2 impurities on performance of direct hydrogen polymer-electrolyte fuel cells", *Journal of Power Sources,* vol. 180, no. 1, pp. 122-131.

Ahluwalia, R.K. & Wang, X. 2008b, "Fuel cell systems for transportation: Status and trends", *Journal of Power Sources,* vol. 177, no. 1, pp. 167-176.

Ahluwalia, R.K. & Wang, X. 2007, "Buildup of nitrogen in direct hydrogen polymer-electrolyte fuel cell stacks", *Journal of Power Sources,* vol. 171, no. 1, pp. 63-71.

Aittamaa, J. 2006, *Virtaustekniikka (Hydraulics)*, Handout, Helsinki University of Technology, Department of Chemical Engineering.

Anderson, R., Zhang, L., Ding, Y., Blanco, M., Bi, X. & Wilkinson, D.P. 2010, "A critical review of two-phase flow in gas flow channels of proton exchange membrane fuel cells", *Journal of Power Sources,* vol. 195, no. 15, pp. 4531-4553.

Aphornratana, S. & Eames, I.W. 1997, "A small capacity steam-ejector refrigerator: experimental investigation of a system using ejector with movable primary nozzle", *International Journal of Refrigeration,* vol. 20, no. 5, pp. 352-358.

Baik, K.D. & Kim, M.S. 2010, "Characterization of nitrogen gas crossover through the membrane in proton-exchange membrane fuel cells", *International Journal of Hydrogen Energy,* vol. In Press, Corrected Proof.

Balat, M. 2008, "Potential importance of hydrogen as a future solution to environmental and transportation problems", *International Journal of Hydrogen Energy,* vol. 33, no. 15, pp. 4013-4029.

Barbir, F. 2005, *PEM fuel cells: Theory and practice,* Elsevier Science & Technology.

Blunier, B. & Miraoui, A. 2005, "Optimization and air supply management of a polymer electrolyte fuel cell", *Vehicle Power and Propulsion, 2005 IEEE Conference*, pp. 7 pp.

Blunier, B., Pucci, M., Cirrincione, G., Cirrincione, M. & Miraoui, A. 2008, "A Scroll Compressor With a High-Performance Sensorless Induction Motor Drive for the Air Management of a PEMFC System for Automotive Applications", *IEEE Transactions on Vehicular Technology,* vol. 57, no. 6, pp. 3413-3427.

Borup, R., Meyers, J., Pivovar, B., Kim, Y.S., Mukundan, R., Garland, N., Myers, D., Wilson, M., Garzon, F., Wood, D., Zelenay, P., More, K., Stroh, K., Zawodzinski, T., Boncella, J., McGrath, J.E., Inaba, M., Miyatake, K., Hori, M., Ota, K., Ogumi, Z., Miyata, S., Nishikata, A., Siroma, Z., Uchimoto, Y., Yasuda, K., Kimijima, K.i. & Iwashita, N. 2007, "Scientific Aspects of Polymer Electrolyte Fuel Cell Durability and Degradation", *Chemical Reviews,* vol. 107, no. 10, pp. 3904-3951.

Chambers, A., Park, C., Baker, R.T.K. & Rodriguez, N.M. 1998, "Hydrogen Storage in Graphite Nanofibers", *The Journal of Physical Chemistry B,* vol. 102, no. 22, pp. 4253-4256.

Cheng, X., Shi, Z., Glass, N., Zhang, L., Zhang, J., Song, D., Liu, Z.-., Wang, H. & Shen, J. 2007, "A review of PEM hydrogen fuel cell contamination: Impacts, mechanisms, and mitigation", *Journal of Power Sources,* vol. 165, no. 2, pp. 739-756.

Colinart, T., Chenu, A., Didierjean, S., Lottin, O. & Besse, S. 2009, "Experimental study on water transport coefficient in Proton Exchange Membrane Fuel Cell", *Journal of Power Sources,* vol. 190, no. 2, pp. 230-240.

Cunningham, J.M. 2001, *Air System Management for Fuel Cell Vehicle Applications*, Michigan State University.

Cunningham, J.M., Hoffman, M.A., Eggert, A.R. & Friedman, D.J. 2000, "The implications of using an expander (turbine) in an air system of a PEM fuel cell engine", Proceedings of the 17th International Electric Vehicle Symposium & Exposition.

Cunningham, J.M., Hoffman, M.A. & Friedman, D.J. 2001, "A comparison of high-pressure and low-pressure operation of PEM fuel cell systems", SAE publications, SAE no. 2001-01-0538.

Faghri, A. & Guo, Z. 2005, "Challenges and opportunities of thermal management issues related to fuel cell technology and modeling", *International Journal of Heat and Mass Transfer,* vol. 48, no. 19-20, pp. 3891-3920.

He, J., Choe, S. & Hong, C. 2008, "Analysis and control of a hybrid fuel delivery system for a polymer electrolyte membrane fuel cell", *Journal of Power Sources,* vol. 185, no. 2, pp. 973-984.

He, S., Li, Y. & Wang, R.Z. 2009, "Progress of mathematical modeling on ejectors", *Renewable and Sustainable Energy Reviews,* vol. 13, no. 8, pp. 1760-1780.

Holmgren, M. 2005, 2005-09-06-last update*, Excel Engineering*. Available: www.x-eng.com [2010, 10/14].

Huang, B.J., Chang, J.M., Wang, C.P. & Petrenko, V.A. 1999, "A 1-D analysis of ejector performance ", *International Journal of Refrigeration,* vol. 22, no. 5, pp. 354-364.

Hussaini, I. 2010, "Intermittent humidification - a novel technique of water management of PEM fuel cells", *SciTopics*.

Hussaini, I.S. & Wang, C.-. 2009, "Visualization and quantification of cathode channel flooding in PEM fuel cells", *Journal of Power Sources,* vol. 187, no. 2, pp. 444-451.

Ihonen, J. 2003, *Development of characterisation methods for the components of the polymer electrolyte fuel cell*, Kungliga Tekniska högskolan.

Ihonen, J. & Keränen, T. 2007, *Literature Survey of fuel cell air contamination and their filtration*, Literature survey.

Ji, M. & Wei, Z. 2009, "A Review of Water Management in Polymer Electrolyte Membrane Fuel Cells", *Energies,* vol. 2, no. 4, pp. 1057-1073.

Jung, S.H., Kim, S.L., Kim, M.S., Park, Y. & Lim, T.W. 2007, "Experimental study of gas humidification with injectors for automotive PEM fuel cell systems", *Journal of Power Sources,* vol. 170, no. 2, pp. 324-333.

Kandlikar, S.G. & Lu, Z. 2009, "Thermal management issues in a PEMFC stack – A brief review of current status", *Applied Thermal Engineering,* vol. 29, no. 7, pp. 1276-1280.

Karnik, A.Y., Jing, S. & Buckland, J.H. 2006, "Control analysis of an ejector based fuel cell anode recirculation system", *American Control Conference, 2006*, pp. 484-489.

Kennedy, D.M., Cahela, D.R., Zhu, W.H., Westrom, K.C., Nelms, R.M. & Tatarchuk, B.J. 2007, "Fuel cell cathode air filters: Methodologies for design and optimization", *Journal of Power Sources,* vol. 168, no. 2, pp. 391-399.

Keskinen, K.I. 1989, *Kemian laitetekniikan taulukoita ja piirroksia 845 (Charts and diagrams in chemical engineering),* 10th edn, Otatieto.

Knights, S.D., Colbow, K.M., St-Pierre, J. & Wilkinson, D.P. 2004, "Aging mechanisms and lifetime of PEFC and DMFC", *Journal of Power Sources,* vol. 127, no. 1-2, pp. 127-134.

Koryta, J. & Kavan, L. 1987, *Principles of electrochemistry,* Second edn, John Wiley & Sons.

Kutz, M. 2009, *Eshbach's Handbook of Engineering Fundamentals,* 5th edn, John Wiley & Sons.

Lampinen, M.J. & Fomino, M. 1993, "Analysis of Free Energy and Entropy Changes for Half-Cell Reactions", *Journal of The Electrochemical Society,* vol. 140, no. 12, pp. 3537-3546.

Larminie, J. & Dicks, A. 2003, *Fuel Cell Systems Explained,* 2nd edn, John Wiley & Sons.

Li, L. & Hurley, J.A. 2007, "Ammonia-based hydrogen source for fuel cell applications", *International Journal of Hydrogen Energy,* vol. 32, no. 1, pp. 6-10.

Liu, F., Lu, G. & Wang, C.-. 2007, "Water transport coefficient distribution through the membrane in a polymer electrolyte fuel cell", *Journal of Membrane Science,* vol. 287, no. 1, pp. 126-131.

Lu, G.Q., Liu, F.Q. & Wang, C.-. 2007, "An approach to measuring spatially resolved water crossover coefficient in a polymer electrolyte fuel cell", *Journal of Power Sources,* vol. 164, no. 1, pp. 134-140.

Ma, X., Yang, D., Zhou, W., Zhang, C., Pan, X., Xu, L., Wu, M. & Ma, J. 2008, "Evaluation of activated carbon adsorbent for fuel cell cathode air filtration", *Journal of Power Sources,* vol. 175, no. 1, pp. 383-389.

Mallant, R. K. A. M. 2003, "PEMFC systems: the need for high temperature polymers as a consequence of PEMFC water and heat management", *Journal of Power Sources,* vol. 118, no. 1-2, pp. 424-429.

McKetta, J.J. 1983, "Ejectors, Steam Jet" in *Encyclopedia of Chemical Processing and Design: Volume 17* Taylor & Francis Ltd, , pp. 167-194.

Mennola, T., Noponen, M., Kallio, T., Mikkola, M. & Hottinen, T. 2004, "Water balance in a free-breathing polymer electrolyte membrane fuel cell", *Journal of Applied Electrochemistry,* vol. 34, no. 1, pp. 31-36.

Mohtadi, R., Lee, W.-. & Van Zee , J.W. 2004, "Assessing durability of cathodes exposed to common air impurities", *Journal of Power Sources,* vol. 138, no. 1-2, pp. 216-225.

Moore, J.M., Adcock, P.L., Lakeman, J.B. & Mepsted, G.O. 2000, "The effects of battlefield contaminants on PEMFC performance", *Journal of Power Sources,* vol. 85, no. 2, pp. 254-260.

Munday, J.T. & Bagster, D.F. 1977, "A New Ejector Theory Applied to Steam Jet Refrigeration", *Industrial & Engineering Chemistry Process Design and Development,* vol. 16, no. 4, pp. 442-449.

Murtomäki, L., Kallio, T., Lahtinen, R. & Kontturi, K. 2009, *Sähkökemia (Electrochemistry),* Teknillinen korkeakoulu, Espoo, Finland.

Papadias, D.D., Ahmed, S., Kumar, R. & Joseck, F. 2009, "Hydrogen quality for fuel cell vehicles – A modeling study of the sensitivity of impurity content in hydrogen to the process variables in the SMR–PSA pathway", *International Journal of Hydrogen Energy,* vol. 34, no. 15, pp. 6021-6035.

Park, S.-., Choe, S.-. & Choi, S.-. 2008, "Dynamic modeling and analysis of a shell-and-tube type gas-to-gas membrane humidifier for PEM fuel cell applications", *International Journal of Hydrogen Energy,* vol. 33, no. 9, pp. 2273-2282.

Perry, R.H. 1997, *Perry's Chemical Engineers' Handbook (7th Edition),* McGraw-Hill.

Rodatz, P., Büchi, F., Onder, C. & Guzzella, L. 2004, "Operational aspects of a large PEFC stack under practical conditions", *Journal of Power Sources,* vol. 128, no. 2, pp. 208-217.

Roder, H.M., McCarty, R.D. & Hall, W.J. 1972, *Computer programs for thermodynamic and transport properties of hydrogen: [Tabcode-II],* , Washington (DC).

Ross, D.K. 2006, "Hydrogen storage: The major technological barrier to the development of hydrogen fuel cell cars", *Vacuum,* vol. 80, no. 10, pp. 1084-1089.

Sakintuna, B., Lamari-Darkrim, F. & Hirscher, M. 2007, "Metal hydride materials for solid hydrogen storage: A review", *International Journal of Hydrogen Energy,* vol. 32, no. 9, pp. 1121-1140.

Seibt, D., Vogel, E., Bich, E. & Buttig, D.H., E. 2006, "Viscosity Measurements on Nitrogen", *Journal of Chemical & Engineering Data,* vol. 51, no. 2, pp. 526-533.

Sundholm, G. 1987, *Sähkökemia 502 (Electrochemistry),* Otakustantamo, Espoo, Finland.

Wang, C.-. 2004, "Fundamental Models for Fuel Cell Engineering", *Chemical Reviews,* vol. 104, no. 10, pp. 4727-4766.

Wood, D.L., Yi, J.S. & Nguyen, T.V. 1998, "Effect of direct liquid water injection and interdigitated flow field on the performance of proton exchange membrane fuel cells", *Electrochimica Acta,* vol. 43, no. 24, pp. 3795-3809.

Yan, Q., Toghiani, H. & Wu, J. 2006, "Investigation of water transport through membrane in a PEM fuel cell by water balance experiments", *Journal of Power Sources,* vol. 158, no. 1, pp. 316-325.

Yang, D., Ma, J., Xu, L., Wu, M. & Wang, H. 2006, "The effect of nitrogen oxides in air on the performance of proton exchange membrane fuel cell", *Electrochimica Acta,* vol. 51, no. 19, pp. 4039-4044.

Ye, X. & Wang, C.-. 2007, "Measurement of Water Transport Properties Through Membrane-Electrode Assemblies", *Journal of The Electrochemical Society,* vol. 154, no. 7, pp. B676-B682.

Zaffou, R., Kunz, H. & Fenton, J.M. 2006, "Temperature-Driven Water Transport in Polymer Electrolyte Fuel Cells", *ECS Transactions,* vol. 3, no. 1, pp. 909-913.

Zaffou, R., Yi, J.S., Kunz, H.R. & Fenton, J.M. 2006, "Temperature-Driven Water Transport Through Membrane Electrode Assembly of Proton Exchange Membrane Fuel Cells", *Electrochemical and Solid-State Letters,* vol. 9, no. 9, pp. A418-A422.

Zhu, Y. & Li, Y. 2009, "New theoretical model for convergent nozzle ejector in the proton exchange membrane fuel cell system", *Journal of Power Sources,* vol. 191, no. 2, pp. 510-519.